

Dirac Fermions and Topological Phases in Magnetic Topological Insulator Films

Kai-Zhi Bai^{1*}, Bo Fu^{2*} and Shun-Qing Shen^{1,3†}

¹ Department of Physics, The University of Hong Kong, Pokfulam Road, Hong Kong, China

² School of Sciences, Great Bay University, Dongguan, China

³ Quantum Science Center of Guangdong-Hong Kong-Macau Greater Bay Area, China

* kzbai@connect.hku.hk, * fubo@gbu.edu.cn, † sshen@hku.hk

Abstract

We develop a Dirac fermion theory for topological phases in magnetic topological insulator films. The theory is based on exact solutions of the energies and the wave functions for an effective model of the three-dimensional topological insulator (TI) film. It is found that the TI film consists of a pair of massless or massive Dirac fermions for the surface states, and a series of massive Dirac fermions for the bulk states. The massive Dirac fermion always carries zero or integer quantum Hall conductance when the valence band is fully occupied while the massless Dirac fermion carries a one-half quantum Hall conductance when the chemical potential is located around the Dirac point for a finite range. The magnetic exchange interaction in the magnetic layers in the film can be used to manipulate either the masses or chirality of the Dirac fermions and gives rise to distinct topological phases, which cover the known topological insulating phases, such as quantum anomalous Hall effect, quantum spin Hall effect and axion effect, and also the novel topological metallic phases, such as half quantized Hall effect, half quantum mirror Hall effect, and metallic quantum anomalous Hall effect.

Copyright attribution to authors.

This work is a submission to SciPost Physics.

License information to appear upon publication.

Publication information to appear upon publication.

Received Date

Accepted Date

Published Date

1

2 Contents

3	1 Introduction	3
4	2 Massless and massive Dirac fermions in a topological insulator film	5
5	2.1 The continuum model	7
6	2.2 The lattice model	10
7	2.2.1 Strong topological insulator	13
8	2.2.2 Weak topological insulator	13
9	2.2.3 Oscillating \mathbb{Z}_2 invariant	13
10	3 The quantum Hall conductivity of Dirac fermions	14
11	3.1 In the continuum model	14
12	3.1.1 Gapless/Metallic case	15
13	3.1.2 Insulating case	16

14	3.2	In the lattice model	16
15	3.2.1	Gapless/Metallic case	16
16	3.2.2	Insulating case	17
17	3.3	A glance in proof of half-quantization	18
18	3.4	View from field theory	19
19	3.5	Unexchangeable limits	21
20	4	Magnetic and orbital fields in topological insulator films	23
21	4.1	Magnetism polarized along \mathbf{z} direction	23
22	4.1.1	Uniform field strength	25
23	4.1.2	Weak Zeeman field	25
24	4.1.3	Strong Zeeman field	27
25	4.2	Other fields	27
26	5	Topological phases with weak field	29
27	5.1	Half quantum mirror Hall effect: a non-magnetic film with mirror symmetry	30
28	5.2	Quantum anomalous Hall effect: Chern Insulators	32
29	5.2.1	Symmetric magnetic structure	32
30	5.2.2	Asymmetric magnetic structure	35
31	5.2.3	Mirror layer Chern number	36
32	5.3	Axion insulator: an antisymmetric magnetic structure	39
33	5.4	MnBi_2Te_4 film: even and odd number of magnetic layers	40
34	5.4.1	Odd layer: Chern insulator	42
35	5.4.2	Even layer: axion insulator	42
36	5.5	Half-quantized anomalous Hall effect: a semi-magnetic film	42
37	5.6	Phase diagram	45
38	6	Topological phases with strong field	47
39	6.1	Metallic quantized anomalous Hall effect: a film with a magnetic sandwich structure	47
40			
41	6.1.1	A qualitatively model with $n = 1, 2$	50
42	6.1.2	Stronger field in the middle	53
43	6.2	Higher Chern Number Insulator	54
44	6.3	Cooperation between middle and surfaces	55
45	7	Discussion and conclusion	59
46	A	Derivation of Eq. (1a)	62
47	A.1	Symmetry analysis of solutions	66
48	A.2	Equivalent block Hamiltonian	66
49	A.3	Analytic expression for mass term	67
50	A.4	Finite-size correction to mass term	70
51	B	Derivation of Eq. (1b)	72
52		References	77
53			
54			

1 Introduction

Topological phases, bridging the abstract topological classification [1–4] to the in practical electronic phases of matter, have gained an increasing interest and redefined the way people understand and estimate physics in condensed matter systems [5–7]. In contrast to phases described by the Landau-Ginzburg theory and spontaneous symmetry breaking scheme [8, 9], phases termed after topological share no local order parameter, but topological invariants [4, 10–12] defined globally only. These invariants, such as Chern numbers and the \mathbb{Z}_2 invariant, exhibit robustness against continuous deformations that do not alter certain preconditions imposed over specified topological class, like the global gap for an insulator [13–16] and symmetry constraints, over total system [3] or the Fermi surface in a metal [4].

Within the vast topological phase landscape, the three-dimensional topological insulator (3D TI) [17–23] stands out as a unique state of matter, protected by the time-reversal symmetry and characterized by a strong \mathbb{Z}_2 index. As a result of the celebrated bulk-boundary correspondence [24–27], the surface of a 3D TI hosts a single gapless Dirac fermion, whose low energy dispersion is necessarily governed by the massless Dirac equation in 2D, exhibiting spin-momentum locking [28]. Nevertheless, the ever existence of such a gapless Dirac fermion has to be restrained by the no-go Nielsen-Ninomiya theorem [29, 30], and it turns out that the high energy states of this fermionic band gain a bulk-like mass [31, 32] to reconcile the contradiction. The sign of this restored mass is defined as the chirality [33] for a regulated 2D gapless Dirac fermion, and it is responsible for the half-quantization of its Hall conductance. The emergence of the high energy mass term due to lattice regularization essentially both breaks parity symmetry [34] explicitly and evades locality [35].

The gapless behavior of the surface Dirac fermion can be altered through the finite-size effect. When the topological insulator is exfoliated into a film, two gapless Dirac fermions emerge at the top and bottom surfaces. However, as the thickness of the film is further reduced to the ultra-thin limit, by quantum confinement [36–38] the surface states of two Dirac bands become gapped. The thickness-dependent mass gap exhibits an exponentially decaying and oscillating pattern [39], revealing multiple topological phase transitions. This phenomenon provides a pathway to realize the 2D quantum spin Hall effect [12, 40–42] with an ultra-thin TI film.

The occurrence of spontaneous magnetization can alter the topological property of the TI film. Typically, a pair of gapless Dirac fermions emerge at two surfaces of a TI film, each carrying half-quantized Hall conductance with opposite signs under mirror symmetry, leading to the half quantum mirror Hall effect [33]. The effect shares a similar quantized non-local transport signature with the quantum spin Hall effect [12, 43–45], while being intrinsically a metallic phase. Further gapping out the surface states by an out-of-plane magnetism [46] gives rise to various topologically distinct phases. Within the scheme of magnetic topological insulators, two such phases have been discovered as the Chern insulator [47–49], aka quantum anomalous Hall effect (QAHE) that is characterized by Chern invariant and quantized Hall plateau, and the axion insulator [50, 51], signatred by zero Hall plateau and non-vanishing longitudinal conductance. A semi-magnetic topological insulator, on the other hand, bears with the half-quantized quantum anomalous Hall effect (half QAHE) [31, 52, 53] with a half quantized Hall conductance and unusual bulk-boundary correspondence, signed by the absence of edge state but the appearance of the pow-law decaying current from boundary to bulk. In addition, if the magnetization is pushed away from the surfaces and towards the middle of the film with sufficient strength, the metallic quantized anomalous Hall effect (metallic QAHE) [32] can occur, which also

104 exhibits integer Hall conductance but lacks chiral edge states.

105 Remarkably, the physics underlying the topological phases in the (magnetic) topo-
 106 logical insulator films can be all attributed to the topological properties of the emergent
 107 two-dimensional Dirac fermions in the system. While certain phases, like QAHE and half
 108 QAHE, can be well explained by focusing on the interplay between surface Dirac fermions
 109 and magnetism, there exist other phases that essentially involve higher bulk bands, no-
 110 tably the metallic QAHE. These higher bulk bands are identified as a series of massive
 111 Dirac fermions, revealing that both gapless and gapped Dirac fermions in the topological
 112 insulator film interact with spontaneous magnetism to generate various topological phases.
 113 The topological index, or the quantized Hall conductance in each phase, is always given
 114 by some gapped or gapless Dirac fermion(s), described by a modified Dirac equation.

115 In this paper, we will provide a unified framework to discuss and review how emer-
 116 gent Dirac fermions exist and generate various topological phases in magnetic topological
 117 insulator films, thus naturally partitioning the paper into two main parts. The first part
 118 of the paper will focus on establishing the existence of Dirac fermions in magnetic topo-
 119 logical insulator films. This discussion will heavily rely on a newly defined basis derived
 120 from an exact solution in 1D. We will thoroughly investigate the Hall conductivity car-
 121 ried by different types of Dirac fermions within this framework, setting the stage for the
 122 subsequent discussion of topological phases. In the second part we will delve into the
 123 characterization and analysis of topological phases in magnetic topological insulator films.
 124 These phases will be classified into weak- and strong-magnetism regimes, providing a com-
 125 prehensive understanding of how different magnetic strengths influence the emergence of
 126 various topological states. In the remainder of this introduction we will give an overview
 127 of the main results of this paper following the line.

128 The TI film is equivalent to a set of Dirac fermions: a pair of massless Dirac fermions
 129 for bands that contain the surface states, and a series of massive Dirac fermions consisting
 130 of purely bulk states, classified by their momentum-dependent mass terms $m_n(\mathbf{k})$. This
 131 scenario holds with both its continuum and lattice model versions, and is made clear and
 132 exact through an introduced unitary transformation in the whole \mathbf{k} -space, based on an
 133 exact solution in one dimension perpendicular to the film plane. The finite-size effect is
 134 briefly discussed here.

135 The Hall conductivity carried by a massive or gapless Dirac fermion is discussed gen-
 136 erally, with additional symmetry constraints imposed on the Fermi surface for the latter
 137 one, for both continuum and lattice models. A direct deduction leads to the result that
 138 the Hall conductivity associated with the gapless and gapped Dirac fermions in the TI film
 139 are $\pm e^2/2h$ and $\mathbf{0}$, respectively, leading to a half quantum mirror Hall effect by $1/2 - 1/2$,
 140 serving as a metallic partner to the insulating quantum spin Hall effect. A brief proof
 141 for the half-quantization of metallic band structure with considered symmetry constraints
 142 over the Fermi surface is also presented. Additionally, a field theoretical deduction for the
 143 half quantization, and a discussion on handling the Hall conductivity of a gapless Dirac
 144 fermion are provided.

145 The introduced magnetism, characterized by out-of-plane polarization, manifests as
 146 two equivalent matrix Higgs fields that collectively couple the Dirac fermions in a TI
 147 film, generating and altering their masses. Treated at the mean-field level, the exchange
 148 interaction stands as an out-of-plane Zeeman field in TI film, which transforms via the
 149 unitary transformation into two momentum-dependent matrix fields $\mathbf{I}_{S/A}(\mathbf{k})$. The two
 150 fields directly couple different species of Dirac fermions and alter their masses, serving as
 151 mass-generating Higgs fields, whose non-vanishing expectation values arise concurrently
 152 with the spontaneous establishment of the ferromagnetic order. Depending on the field
 153 strength, generally two regimes as weak and strong magnetism are classified. In addi-

154 tion, the forms of other kinds of spin and orbital fields under unitary transformation are
155 discussed.

156 In the weak Zeeman field regime, the topological phases are characterized by focusing
157 on $\mathbf{n} = \mathbf{1}$ matrix elements affecting the two gapless Dirac fermions near the surface. This
158 framework clarifies the underlying physics behind the Chern insulator, axion insulator, and
159 half QAHE, with symmetric, anti-symmetric, or unilateral distribution of Zeeman fields at
160 the surface of the TI film, respectively. The resulting Hall conductance exhibits quantized
161 nature: $\mathbf{1} + \mathbf{0}$, $\mathbf{0} + \mathbf{0}$, and $\mathbf{1}/2 + \mathbf{0}$ in units of e^2/h . Additionally, the mirror layer Chern
162 number in the Chern insulator with symmetrically distributed magnetism is examined,
163 revealing $(\mathbf{1}/4) - (\mathbf{1}/2) - (\mathbf{1}/4)$ partition for the non-trivial band and $(\mathbf{c}/4) - (-\mathbf{c}/2) - (\mathbf{c}/4)$
164 with $\mathbf{c} \approx \mathbf{1}$ for the trivial band.

165 In the strong Zeeman field regime, the discussion is based on the effective mass pic-
166 ture, involving the gapped series of Dirac fermions through matrix Higgs fields couplings.
167 Another metallic topological phase, the metallic QAHE, is identified where the magnetism
168 is centralized in the middle of the TI film. Despite remaining gapless and lacking chiral
169 edge states, its Hall conductance is quantized into an integer over e^2/h . Additionally,
170 higher Chern insulators resulting from sub-band inversion at high-symmetry points are
171 presented under a uniform Zeeman field. Furthermore, the paper discusses topological
172 phases characterized by cooperation between magnetism in the middle and surface, based
173 on the framework of gapping out surface states in the metallic QAHE.

174 The plan of the remainder of this paper is as follows. Beginning with the exact solution
175 of the model Hamiltonian for a topological insulator film in Section 2, we demonstrate that
176 a TI film comprises a pair of gapless Dirac fermions, containing low-energy surface states,
177 and a series of gapped massive bulk Dirac fermions. Section 3 offers a comprehensive
178 discussion on the Hall conductivity, a critical indicator revealing the presence of topological
179 phases, carried by different species of Dirac fermions. Moving on to the inclusion of
180 magnetism in Section 4, we unveil the role of magnetism as matrix Higgs fields, responsible
181 for generating masses of the Dirac fermions in a TI film. This section also briefly explores
182 other spin and orbital fields possible within the framework. In Section 5, based on the weak
183 magnetism approximation, we identify topological phases processable under the lowest
184 four-band model framework, which stresses surface states with magnetism: half quantum
185 mirror Hall effect, quantum anomalous Hall effect, half-quantized anomalous Hall effect,
186 and axion insulator. We introduce the mirror layer Chern number and illustrate the Hall
187 conductivity distribution in symmetrically magnetized TI film. The Chern and axion
188 insulator phases in interlayer anti-ferromagnetic material MnBi_2Te_4 are also discussed
189 under the frame. In Section 6, we delve into topological phases within relatively strong
190 magnetism regimes, such as high Chern number insulators and the metallic quantized
191 anomalous Hall effect, where bulk Dirac fermions come into play. The paper concludes in
192 Section 7 with a summary and a discussion of future prospects.

193 **2 Massless and massive Dirac fermions in a topological insulator** 194 **film**

195 In this section, by solving the minimal continuum and lattice models of the topological
196 insulator, we show that from the physical aspect, a topological insulator film is composed
197 of a pair of gapless Dirac fermions, whose low energy parts near Dirac point are composed
198 of massless surface states inside the bulk gap while the high energy parts away from the
199 Dirac point evolve into bulk states gradually, together with a series of gapped massive

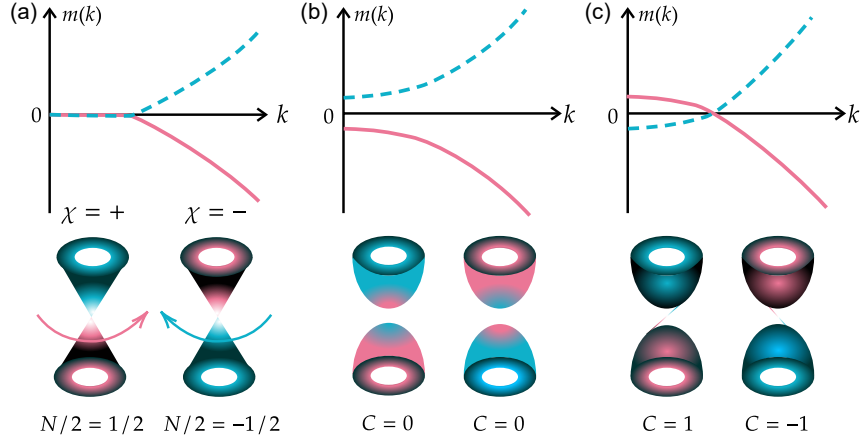


Figure 1: Schematic momentum dependent mass configurations (upper panel) and corresponding band structure of Dirac fermions (lower panel). The quantization of Hall conductivity is denoted by \mathbf{N} for half quantization in a metallic band and \mathbf{C} for quantization at the bottom of a gapped band. The color assigned to the Dirac cones represent the sign of Berry curvature with red for positive and blue for negative. (a) On the left panel, two gapless Dirac fermions are shown, whose masses are zero at low energy near the Dirac point (assumed to be $\mathbf{k} = \mathbf{0}$), while non-vanishing at high-energy with opposite signs, which we define as the **chirality** χ of a 2D gapless Dirac fermion. Such chirality unambiguously determines the sign of the loop integral of Berry connection around the Fermi surface, consequently determining the sign of half-quantized Hall conductivity. (b) In the middle, two trivially gapped massive Dirac fermions are present, with masses being either positive or negative for all \mathbf{k} , leading to a sign change of Berry curvature and a totally vanishing Hall conductivity labeled by zero Chern number. (c) On the right panel, two non-trivial gapped Dirac cones are displayed, and the corresponding masses exhibit kink configurations with sign change between low and high energy areas. Such non-trivial mass configuration indicates overall Berry curvature sign convergence, and leads to a non-vanishing Hall conductivity labelled by an integer Chern number. The non-triviality is also addressed by formally drawing states connecting conduction and valence bands, well-known as chiral edge states for a Chern band under open boundary condition [13, 14].

200 Dirac fermions consist of purely bulk states. Quantitatively, we write

$$H_c(\mathbf{k}) = \bigoplus_n [\lambda_{\parallel} \mathbf{k} \cdot \boldsymbol{\sigma} + m_n(\mathbf{k}) \tau_z \sigma_z], \quad (1a)$$

$$H_l(\mathbf{k}) = \bigoplus_{n=1}^{L_z} [\lambda_{\parallel} \sin(k_x a) \sigma_x + \lambda_{\parallel} \sin(k_y a) \sigma_y + m_n(\mathbf{k}) \tau_z \sigma_z], \quad (1b)$$

201 for the continuum and lattice model, respectively. Here we adopt homogeneous in-film-
 202 plane parameter set with \mathbf{a} and λ_{\parallel} the in plane lattice constant and Fermi velocity, and
 203 $\mathbf{k} = (\mathbf{k}_x, \mathbf{k}_y)$ is the in film plane wavevector. Notice that an infinitely direct summed Dirac
 204 fermions exists in the continuum model, while there are only $2L_z$ species with L_z the layer
 205 number along opened \mathbf{z} -direction of the film in the lattice model. For the mainly concerned
 206 individual Dirac cone with a single Dirac point at $\mathbf{k} = \mathbf{0}$, its topological property is revealed
 207 based on a general discussion over the nature of its Hall conductivity quantization, as
 208 revealed in the schematic diagram Fig. 1. Especially, in the strong TI film with a single
 209 Dirac cone at Γ , aka $\mathbf{k} = \mathbf{0}$ point, the gapless pair of Dirac fermions carry $\pm e^2/2h$, as
 210 half-quantized Hall conductivity, while the gapped series are all trivial.

211 2.1 The continuum model

212 In this subsection, the exact solution of the confined 3D modified Dirac equation, which
 213 is the continuum model describing the topological insulator film, is presented. A detailed
 214 study can be found in Appendix A.

215 The continuum model Hamiltonian for the 3D TI reads [27, 54]

$$\begin{aligned} H_{\text{TI}}(\mathbf{k}, k_z) &= \lambda_{\parallel} (\mathbf{k} \cdot \boldsymbol{\sigma}) \tau_x + \lambda_{\perp} k_z \sigma_z \tau_x + (m_0(\mathbf{k}) - t_{\perp} k_z^2) \sigma_0 \tau_z \\ &= H_{1d}(\mathbf{k}, k_z) + H_{\parallel}(\mathbf{k}), \end{aligned} \quad (2)$$

216 where $H_{\parallel}(\mathbf{k}) = \lambda_{\parallel} (\mathbf{k} \cdot \boldsymbol{\sigma}) \tau_x$, $m_0(\mathbf{k}) = m_0 - t_{\parallel} k^2$. This Hamiltonian is isotropic only in \mathbf{x} - \mathbf{y}
 217 plane. Substituting $k_z \mapsto -i \partial_z$ leads to the real- \mathbf{z} -space description for the 1-D part as
 218 $H_{1d}(\mathbf{k}, \mathbf{z}) = \oplus_{s=\pm} \mathbf{h}(s)$, where

$$\mathbf{h}(s) = -is \lambda_{\perp} \partial_z \tau_x + (m_0(\mathbf{k}) + t_{\perp} \partial_z^2) \tau_z. \quad (3)$$

219 Solving the eigen-problem $\mathbf{h}(s)\boldsymbol{\phi} = E\boldsymbol{\phi}$ leads to specifically symmetrized chiral-partner
 220 basis [36–38]

$$\boldsymbol{\varphi}^n(s) = C \begin{pmatrix} -is \lambda_{\perp} f_+^n \\ t_{\perp} \eta^n f_-^n \end{pmatrix}, \quad E = m_n, \quad (4a)$$

$$\boldsymbol{\chi}^n(s) = C \begin{pmatrix} t_{\perp} \eta^n f_-^n \\ is \lambda_{\perp} f_+^n \end{pmatrix}, \quad E = -m_n, \quad (4b)$$

221 where the dependence on (\mathbf{k}, \mathbf{z}) is inherited inside even/odd parity functions $f_{\pm}^n(\mathbf{k}, \mathbf{z})$
 222 and real factor $\eta^n(\mathbf{k})$, whose definition can be found in Appendix A. The \mathbf{k} -dependent
 223 eigenvalue of $\mathbf{h}(s)$ is represented by $\pm m_n(\mathbf{k})$, $n = 1, 2, \dots$, as a mass term, which can be
 224 solved in a closed manner through equations

$$m_n = m_0(\mathbf{k}) - t_{\perp} \frac{\xi_1^2 g(\xi_1) - \xi_2^2 g(\xi_2)}{g(\xi_1) - g(\xi_2)}, \quad (5a)$$

$$\xi_{\alpha} = \sqrt{-\frac{F}{D} + (-1)^{\alpha-1} \frac{\sqrt{R}}{D}}, \quad \alpha = 1, 2, \quad (5b)$$

225 where

$$\begin{cases} g(\xi) = \tan(\xi L/2)/\xi \\ D = 2t_{\perp}^2 \\ F = -2m_0(k)t_{\perp} + \lambda_{\perp}^2 \\ R = F^2 - 2D(m_0^2(k) - m_n^2) \end{cases} \quad (6)$$

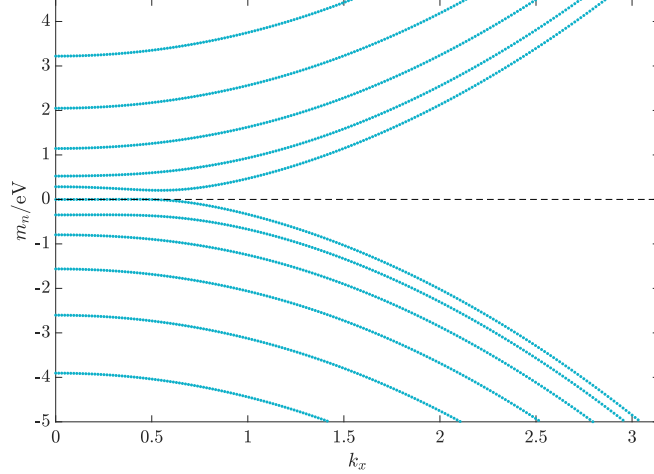


Figure 2: The momentum-dependent mass of Dirac fermions in a TI film as a continuum. Lowest several momentum-dependent $m_n(\mathbf{k})$ along k_x solved from closed equations Eq. (5) are presented, while the homogeneous in-plane nature of the model ensures that the asymptotic behavior of $m_n(\mathbf{k})$ is the same as $k \rightarrow \infty$. Here the film thickness $L = (L_z + 1)c$ with $L_z = 10$ chosen here as a TI film with 10 layers. Index n is assigned in the way that $|m_n|$ increases with n . Especially notice the sign-jump behavior that $\text{sgn}(m_n(\infty)) = (-1)^n$. From here on, the model parameters on lattice for numerical calculations and verifications are set as $\lambda_{\parallel} = 0.41$ eV, $\lambda_{\perp} = 0.44$ eV, $t_{\parallel} = 0.566$ eV, $t_{\perp} = 0.4$ eV, $m_0 = 0.28$ eV, $\mathbf{a} = \mathbf{b} = 1$ nm, $\mathbf{c} = 0.5$ nm if with no specific indication [54]. This parameter choice makes the bulk 3D TI a strong one with single Dirac point at Γ . And for the continuum model discussed here, the substitution $\lambda_{\parallel} \rightarrow \lambda_{\parallel} \mathbf{a}$, $\lambda_{\perp} \rightarrow \lambda_{\perp} \mathbf{c}$, $t_{\parallel} \rightarrow t_{\parallel} \mathbf{a}^2$, $t_{\perp} \rightarrow t_{\perp} \mathbf{c}^2$ should be recognized.

226 Project TI film Hamiltonian on eigenstates of H_{1d} equals to performing an infinite-
 227 dimensional local unitary transformation in \mathbf{k} -space, which gives Hamiltonian equivalent
 228 to the TI film one as (see Appendix A.)

$$H(\mathbf{k}) = \bigoplus_n \lambda_{\parallel} \tau_0(\mathbf{k} \cdot \boldsymbol{\sigma}) + m_n(\mathbf{k}) \tau_z \sigma_z, \quad (7)$$

229 as Eq. (1a), where the projection basis is organized as

$$\begin{aligned} \Phi_1^n &= \begin{pmatrix} \varphi^n(+), \\ 0 \end{pmatrix}, \Phi_2^n = \begin{pmatrix} 0 \\ \chi^n(-) \end{pmatrix}, \\ \Phi_3^n &= \begin{pmatrix} \chi^n(+), \\ 0 \end{pmatrix}, \Phi_4^n = \begin{pmatrix} 0 \\ \varphi^n(-) \end{pmatrix}. \end{aligned} \quad (8)$$

230 We have to emphasize here that although spin is still preserved as $\boldsymbol{\sigma}$ in the transformed
 231 Hamiltonian, the degrees of freedom $\boldsymbol{\tau}$ newly appeared here shares a different meaning
 232 as with the original TI film Hamiltonian. Notice that $\Phi_{1,4}$ ($\Phi_{2,3}$) are \mathbf{z} -parity even (odd)

233 states, while $\Phi_{1,2}$ ($\Phi_{3,4}$) are \mathbf{z} -mirror even (odd) states, which means that under the pro-
 234 jection, the unitary matrices related to two operators are transformed into (see Appendix
 235 A.)

$$P_z = \tau_z \sigma_z, \quad (9a)$$

$$M_z = \tau_z. \quad (9b)$$

236 Meanwhile, the local unitary matrix in \mathbf{k} -space that transforms the continuum model
 237 Hamiltonian under the original representation is formally written as

$$U^c(\mathbf{k}, \mathbf{z}) = (\{\{\Phi(\mathbf{k}, \mathbf{z})\}_i\}^n), \quad (10)$$

238 where the double brackets mean that we arrange $i = 1, 2, 3, 4$ index inside each $n = 1, 2, \dots$,
 239 we see that U^c is topologically trivial in $(\mathbf{k}_x, \mathbf{k}_y)$ space, as it consists of certain arrange-
 240 ment of eigenstates Φ_i^n , which is solved from the separated 1-D Hamiltonian and has a
 241 well-defined global representation within the same gauge choice in $(\mathbf{k}_x, \mathbf{k}_y)$ plane, and is
 242 therefore topologically trivial.

243 Our solution reveals that the 3D topological insulator film is composed of effectively
 244 2D multi-Dirac fermions, different by their mass terms represented in Fig. 2 only. Notice
 245 that for the continuum model, there are in fact an infinite number of \mathbf{m}_n s as a basic
 246 property of bound states in a quantum well, and we just present several lowest branches
 247 of the solutions. Also notice that from the solved \mathbf{m}_n , the mass terms show sign jumping
 248 behavior at high energy (large \mathbf{k}). Comparing the mass configurations in continuum model
 249 with the general classification in Fig. 1 reveals that while all $n \geq 2$ masses serve as trivial
 250 massive Dirac band in the bulk, the lowest states with $n = 1$ are necessarily not, which
 251 in the presented case serve as two possible gapless Dirac cones whose low-energy parts
 252 are localized \mathbf{z} -mirror-symmetrically at top and bottom surfaces. Especially, the analytic
 253 expression for $\mathbf{m}_1(\mathbf{k})$, when the film is thick enough, can be written as [33] (also see
 254 Appendix A, and here $t_\perp > 0$ is assumed without losing generality)

$$\mathbf{m}_1(\mathbf{k}) = \Theta(-m_0(\mathbf{k}))m_0(\mathbf{k}). \quad (11)$$

255 Notice that the Heaviside Theta function appeared here only reveals physics that, at low-
 256 energy zone near the Dirac point, the surface Dirac cone is massless, which preserves
 257 both time-reversal and parity symmetry, while for the high-energy part away from the
 258 Dirac point, the non-vanishing mass term reveals that the surface Dirac cone has emerged
 259 into the bulk state, which breaks both time-reversal and parity symmetry explicitly. The
 260 appearance of such non-vanishing high-energy mass term is analogical to the introduced
 261 regulator [55–57] in quantum field theory. In this sense, one should not worry about the
 262 nonanalytic behavior of the Theta function near $\mathbf{m}_0(\mathbf{k}) = \mathbf{0}$, as it can always be replaced
 263 by its mollifier [31, 58].

264 For the completeness of discussion here, we notice that an ultra-thin TI film bears
 265 an exponentially decaying oscillating small gap $\mathbf{m}(\mathbf{0})$ with varying film thickness [36–38],
 266 which reads upon lowest order (for derivation, also see Appendix A)

$$m_1(\mathbf{0}) \approx -\frac{4m_0}{\sqrt{4\gamma-1}} \sin(u \sqrt{4\gamma-1}L) e^{-uL}, \quad (12)$$

267 with $\gamma = m_0 t_\perp / \lambda_\perp^2$, $u = \lambda_\perp / 2t_\perp$. The numerical result is shown in Fig. 3, with a great
 268 correspondence between the lowest order approximated gap and that from solving the
 269 set of non-linear equations, especially for relatively large L . The exponentially decaying
 270 tendency is best revealed by the logarithmic absolute value of mass gap at $\mathbf{k} = \mathbf{0}$, as its

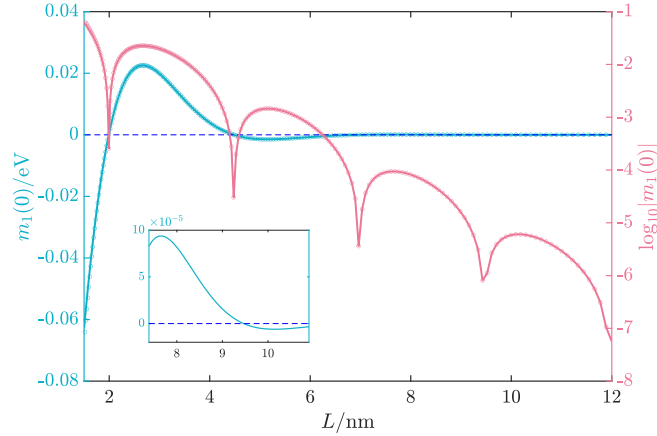


Figure 3: Finite size effect of an ultra-thin TI film in the continuum model, revealed by the exponentially decaying oscillating mass gap $2\mathbf{m}_1(\mathbf{0})$ of surface Dirac cones. Both $\mathbf{m}_1(\mathbf{0})$ and its logarithmic absolute value varying with film thickness L are shown. The solid line represents results from Eq. (12), while the circles are obtained from solving the self-consistent equations Eq. (5) directly. The inner picture shows an amplified area of the $\mathbf{m}_1(\mathbf{0})-L$ diagram.

271 center decreases linearly with thickness, while the oscillating nature is revealed by the
 272 dips, which will extend to minus infinity at strict gap closing point, and the mass gap will
 273 reverse its sign before and after the dip, as shown directly by the $\mathbf{m}_1(\mathbf{0})-L$ diagram and the
 274 inner amplified picture. Since $\mathbf{m}_1(\infty) = \mathbf{m}_0(\infty) < \mathbf{0}$ is certain, we see that the oscillating
 275 behavior of $\mathbf{m}_1(\mathbf{0})$ with thickness L can drive $\mathbf{m}_1(\mathbf{k})$ to share configuration that jumps
 276 between the one shown in Fig. 1(b) and (c), i.e., between a trivial band and a band with
 277 unit Chern number. Then for an ultra-thin film which owns two copies $\pm\mathbf{m}_1(\mathbf{k})$ reflected
 278 by τ_z in Eq. (7), the \mathbb{Z}_2 topological index shows jumping behavior between $\mathbb{Z}_2 = \mathbf{0}$ and
 279 $\mathbb{Z}_2 = \mathbf{1}$, i.e., between a band insulator and a quantum spin Hall insulator [40–42, 59, 60].
 280 We will not discuss further about this phenomenon except for giving an explicit $\mathbb{Z}_2(L_z)$
 281 oscillating diagram below in the lattice model subsection shown in Fig. 5. We emphasize
 282 here that the exponentially decaying gap will not affect physically observable topological
 283 phase, either for an insulating or metallic one, for a TI film with enough thickness.

284 The solution of the continuum model enlightens us to commence with the lattice model
 285 of TI film below.

286 2.2 The lattice model

287 In this subsection, we ask and deal with the same question as above, but in the more
 288 realistic lattice model. Details are present in Appendix B.

289 The Hamiltonian of a 3D TI with nearest-neighbour hopping on cubic lattice is [17, 54]

$$\mathcal{H}_{TI} = \sum_l \Psi_l^\dagger \mathcal{M}_0 \Psi_l + \sum_{l,\mu} \left(\Psi_l^\dagger \mathcal{T}_\mu \Psi_{l+\mu} + \text{h.c.} \right), \quad (13)$$

290 where energy and hopping matrices are $\mathcal{M}_0 = (\mathbf{m}_0 - 2 \sum_\mu t_\mu) \boldsymbol{\beta}$, $\mathcal{T}_\mu = t_\mu \boldsymbol{\beta} - i \frac{\lambda_\mu}{2} \boldsymbol{\alpha}_\mu$, with
 291 \mathbf{l} and $\boldsymbol{\mu}$ denoting site locations and three spatial directions while $\{\boldsymbol{\beta}, \boldsymbol{\alpha}_\mu\}$ denoting Dirac
 292 matrices under standard Dirac representation $\boldsymbol{\beta} = \sigma_0 \tau_z$, $\boldsymbol{\alpha}_\mu = \sigma_\mu \tau_x$, where Pauli matrices
 293 σ_μ and τ_μ represent different degrees of freedom, respectively. For instance, one could
 294 choose they to represent spin and pseudo-spin (like orbital) ones. Ψ_l represents vectorized
 295 Fermionic operator at site \mathbf{l} . Notice that when adopting a full Fourier transformation upon

296 all three spatial dimensions, i.e., an infinite bulk system, the Hamiltonian is transformed
 297 into the standard modified Dirac's equation [27] on lattice $\mathcal{H}_{TI} = \sum_{\mathbf{k}} \Psi_{\mathbf{k}}^\dagger H(\mathbf{k}) \Psi_{\mathbf{k}}$ where

$$H(\mathbf{k}) = \sum_{\mu} \lambda_{\mu} \sin(k_{\mu} a_{\mu}) \alpha_{\mu} + \left[m_0 - 4t_{\mu} \sin^2 \left(\frac{k_{\mu} a_{\mu}}{2} \right) \right] \beta, \quad (14)$$

298 whose continuum model is just an anisotropic version of Eq. (2). This model avoids
 299 the fermion-doubling problem [29, 30] by introducing Wilson terms [34] that break chiral
 300 symmetry explicitly for $\mathbf{k} \neq \mathbf{0}$.

301 Consider such a film with L_z number of sites along \mathbf{z} direction. The Fourier transfor-
 302 mation in \mathbf{x} - \mathbf{y} plane gives

$$\begin{aligned} \mathcal{H}_{\text{Film}} = & \sum_{l_z, \mathbf{k}} \left(\Psi_{l_z, \mathbf{k}}^\dagger \mathcal{M}_0(\mathbf{k}) \Psi_{l_z, \mathbf{k}} + \Psi_{l_z, \mathbf{k}}^\dagger \mathcal{T}_z \Psi_{l_z+1, \mathbf{k}} + \text{h.c.} \right) \\ & + \sum_{l_z, \mathbf{k}} \Psi_{l_z, \mathbf{k}}^\dagger H_{\parallel} \Psi_{l_z, \mathbf{k}}, \end{aligned} \quad (15)$$

303 with

$$H_{\parallel} = \lambda_{\parallel} [\sin(k_x a) \sigma_x \tau_x + \sin(k_y b) \sigma_y \tau_x], \quad (16)$$

304 and $\mathcal{M}_0(\mathbf{k}) = M_0(\mathbf{k}) \sigma_0 \tau_z = [m_0(\mathbf{k}) - 2t_{\perp}] \sigma_0 \tau_z$, where

$$m_0(\mathbf{k}) = m_0 - 4t_{\parallel} \left(\sin^2 \frac{k_x a}{2} + \sin^2 \frac{k_y b}{2} \right). \quad (17)$$

305 Note that we have set $t_x = t_y = t_{\parallel}$, $t_z = t_{\perp}$, $\lambda_x = \lambda_y = \lambda_{\parallel}$, $\lambda_z = \lambda_{\perp}$, $\mathbf{a} = \mathbf{b}$.

306 The solution of lattice model [32] shares much similarity with the continuum one. The
 307 details can be found in Appendix B as a repeat. Separating the Hamiltonian at \mathbf{k} as

$$\mathcal{H}_{\text{Film}}(\mathbf{k}) = \mathcal{H}_{1d}(\mathbf{k}) + \mathcal{H}_S(\mathbf{k}), \quad (18)$$

308 where

$$\mathcal{H}_{1d}(\mathbf{k}) = \sum_{l_z} \left(\Psi_{l_z, \mathbf{k}}^\dagger \mathcal{M}_0(\mathbf{k}) \Psi_{l_z, \mathbf{k}} + \Psi_{l_z, \mathbf{k}}^\dagger \mathcal{T}_z \Psi_{l_z+1, \mathbf{k}} + \text{h.c.} \right), \quad (19a)$$

$$\mathcal{H}_S(\mathbf{k}) = \sum_{l_z} \Psi_{l_z, \mathbf{k}}^\dagger H_{\parallel} \Psi_{l_z, \mathbf{k}}. \quad (19b)$$

309 The eigenvalues of \mathcal{H}_{1d} can be obtained with a set of simultaneous equations below,

$$m_n = M + 2t_{\perp} \frac{\cos \xi_1 g(\xi_1) - \cos \xi_2 g(\xi_2)}{g(\xi_1) - g(\xi_2)}, \quad (20a)$$

$$\cos \xi_{\alpha} = \frac{-Mt_{\perp} + (-1)^{\alpha-1} \sqrt{M^2 t_{\perp}^2 - (t_{\perp}^2 - \lambda_{\perp}^2 / 4)(M^2 + \lambda_{\perp}^2 - m_n^2)}}{2(t_{\perp}^2 - \lambda_{\perp}^2 / 4)}, \quad (20b)$$

310 where

$$\begin{cases} M = M_0(\mathbf{k}), \\ g(\xi) = \frac{\tan(\xi(L_z + 1))/2}{\sin \xi}, \end{cases} \quad (21)$$

311 and the sign of ξ is fixed by

$$\sin \xi_{\alpha} = \sqrt{1 - \cos^2 \xi_{\alpha}}, \quad \alpha = 1, 2. \quad (22)$$

312 Now, different from the continuum model, the set of equations give L_z solutions $\mathbf{m}_n(\mathbf{k}), n = 1, 2, \dots, L_z$
 313 including one surface state and $L_z - 1$ purely trivial bulk states, if within suitable choice
 314 of parameters. This is essentially because now the Dirac equation is put on lattice, and
 315 the number of solutions is constrained by finite lattice constants. And the other set of L_z
 316 masses are just the chiral partners with eigenvalues $-\mathbf{m}_n(\mathbf{k})$.

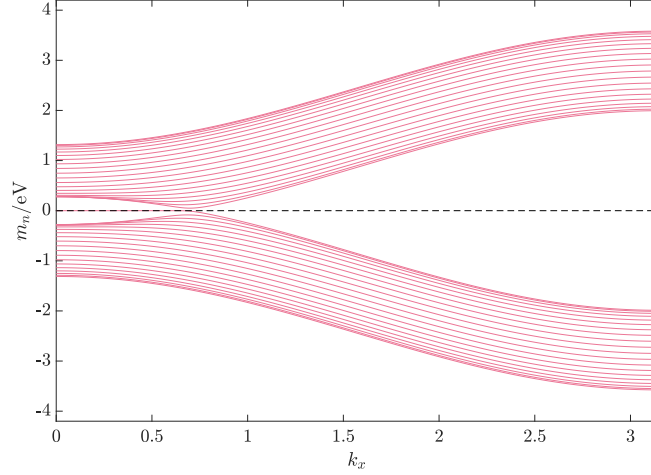


Figure 4: The momentum-dependent mass of Dirac fermions in a TI film on the lattice. Namely, $\mathbf{m}_n(\mathbf{k}), n = 1, 2, \dots, L_z$ along k_x solved from closed equations Eq. (20) of lattice model with $L_z = 40$. Again, index n is assigned in the way that $|\mathbf{m}_n(\pi, \pi)|$ increases with n . Especially notice the sign-jump behavior that $\text{sgn}(\mathbf{m}_n(\pi, \pi)) = (-1)^n$.

317 The projection basis shares the same form as with the continuum model eigenstates,
 318 with only re-defined factor η (for details, refer to Appendix B or [32]). And the projection
 319 of the TI film model offers an equivalent description as

$$H(\mathbf{k}) = \bigoplus_{n=1}^{L_z} [\lambda_{\parallel}(\sin(k_x a)\sigma_x + \sin(k_y b)\sigma_y) + m_n(k)\tau_z\sigma_z], \quad (23)$$

320 as Eq. (1b), where $2L_z$ Dirac fermions $H = \Theta_{n,\chi} h_{n,\chi}(\mathbf{k})$ emerge as

$$h_{n,\chi}(\mathbf{k}) = \lambda_{\parallel}(\sin(k_x a)\sigma_x + \sin(k_y b)\sigma_y) + \chi m_n(k)\sigma_z, \quad (24)$$

321 with $\chi = \pm$ labelling the mirror eigenvalue [33]. An example of $\mathbf{m}_n(\mathbf{k})$ with $L_z = 80$ is pre-
 322 sented in Fig. 4. Among these Dirac fermions, two of them with $\pm\mathbf{m}_1(\mathbf{k})$ are gapless Dirac
 323 cones with their low-energy states localized at top and bottom surfaces, while emerging
 324 into the bulk at their high-energy away from Dirac point, and the remaining fermions are
 325 all gapped. Notice that the same arguments about the projection as a trivial local unitary
 326 transformation and Heaviside Theta function form of lowest solution (see below) can be
 327 made here, as in the continuum model.

328 Generally, the lowest mass reads ($t_{\perp} > 0$ assumed)

$$\mathbf{m}_1(\mathbf{k}) = \Theta[|M_0(\mathbf{k})| - 2t_{\perp}](2t_{\perp} - |M_0(\mathbf{k})|), \quad (25)$$

329 as an analogy with Eq. (11), with respect to the non-trivial condition of \mathcal{H}_{1d} , as a chiral
 330 symmetric 1-D lattice Hamiltonian sharing similar form with the Su-Schrieffer-Heeger
 331 model [27, 61, 62]. And as one can see, since from the continuum model to the lattice
 332 model, the base manifold where momentum \mathbf{k} lives changes from a 2-sphere \mathbf{S}^2 to a 2-
 333 Torus \mathbf{T}^2 , which splits the original infinity point $\mathbf{k} = +\infty$ of the continuum Dirac operator

334 $\mathbf{k} \cdot \boldsymbol{\sigma}$ to three additional Dirac points, $\mathbf{X} = (\boldsymbol{\pi}, \mathbf{0})$, $\mathbf{Y} = (\mathbf{0}, \boldsymbol{\pi})$ and $\mathbf{M} = (\boldsymbol{\pi}, \boldsymbol{\pi})$ of the lattice
 335 Dirac operator $\sin(\mathbf{k}_x)\boldsymbol{\sigma}_x + \sin(\mathbf{k}_y)\boldsymbol{\sigma}_y$ (unit lattice constant), apart from $\boldsymbol{\Gamma} = (\mathbf{0}, \mathbf{0})$, as a
 336 consequence of the periodicity driven fermion-doubling [29,30], the topological property of
 337 the film system is altered by terms on the ‘boundary’ and reflected exactly by the changed
 338 form of $\mathbf{m}_1(\mathbf{k})$. Such a change is known to generate weak topological phases [2,17] apart
 339 from the classification hierarchy, and here for the completeness we give a minor discussion.

340 2.2.1 Strong topological insulator

341 Consider $\mathbf{h}_{1,\mathbf{x}}$, and one finds that Dirac points can exist only at four high symmetry
 342 points $\boldsymbol{\Gamma}, \mathbf{X}, \mathbf{Y}, \mathbf{M}$, then the above general formula can hold gapless Dirac fermions with
 343 linear dispersion only within three parameter regimes

$$\begin{cases} \mathbf{0} < m_0 < 4t_{\perp} \\ 4t_{\parallel} < m_0 < 4t_{\parallel} + 4t_{\perp} \\ 8t_{\parallel} < m_0 < 8t_{\parallel} + 4t_{\perp} \end{cases}, \quad (26)$$

344 inside which $\mathbf{m}_1(\mathbf{k}) = \mathbf{0}$ can be realized for high symmetry points. Here we assume without
 345 losing generality that $\mathbf{0} < t_{\perp} < t_{\parallel}$.

346 Now the first and the third case generates two strong topological insulators (STI), with
 347 the single Dirac point located at $\boldsymbol{\Gamma}$ and \mathbf{M} , respectively. For these two cases, a simplified
 348 mass term can be written separately as

$$\mathbf{m}_1(\mathbf{k}) = \Theta(-m_0(\mathbf{k}))\mathbf{m}_0(\mathbf{k}), \quad (27a)$$

$$\mathbf{m}_1(\mathbf{k}) = \Theta[m_0(\mathbf{k}) - 4t_{\perp}](4t_{\perp} - m_0(\mathbf{k})). \quad (27b)$$

349 And to illustrate the topological phases we are interested in **in this paper**, as to be discussed
 350 in the following sections, we choose parameters so that the first case $\mathbf{0} < m_0 < 4t_{\perp} < 4t_{\parallel}$ is
 351 satisfied, and it will be adequate to write $\mathbf{m}_1(\mathbf{k}) = \Theta(-m_0(\mathbf{k}))\mathbf{m}_0(\mathbf{k})$, which is zero when
 352 $m_0(\mathbf{k}) > \mathbf{0}$ with \mathbf{k} near the $\boldsymbol{\Gamma}$ point, and becomes negative when $m_0(\mathbf{k}) < \mathbf{0}$ away from $\boldsymbol{\Gamma}$
 353 point.

354 2.2.2 Weak topological insulator

355 The second case is also somewhat of interest, however, we will just swipe through its
 356 basic property. At this time, as one can easily verify, two gapless Dirac cones at \mathbf{X}
 357 and \mathbf{Y} form and they are connected through high energy bulk states. Such a phase is
 358 recognized as the weak topological insulator (WTI) in the literature [17] and does not
 359 belong to the usual ten-fold way classification [2]. Especially notice that such a phase can
 360 be recognized as a transition phase between two strong topological insulator phases stated
 361 above, accompanied by the Lifshitz transition of Fermi surface [63].

362 2.2.3 Oscillating \mathbb{Z}_2 invariant

363 As discussed in the continuum model case, in ultra-thin film limit, the strong TI thin
 364 film with single Dirac cone at $\boldsymbol{\Gamma}$ ($\mathbf{k} = \mathbf{0}$) point will show oscillating behavior between
 365 a quantum spin Hall insulator and an ordinary insulator. The topological index of this
 366 kind is carried out explicitly in Fig. 5, with $\mathbb{Z}_2 = (-1)^{\nu}$ with $\nu = \mathbf{0}, \mathbf{1}$, and the latter
 367 corresponds to a non-trivial 2D quantum spin Hall insulator. The mass oscillating and
 368 the index oscillating matches perfectly, as $\mathbb{Z}_2 = -1$ ($\nu = \mathbf{1}$) zones correspond to $\mathbf{m}_1(\mathbf{0}) > \mathbf{0}$,
 369 so do their sign transitions (remind that $\mathbf{m}_1(\boldsymbol{\pi}, \boldsymbol{\pi}) < \mathbf{0}$ and $\mathbf{m}_1(\mathbf{0}) > \mathbf{0}$ leads to a nontrivial
 370 mass configuration, as to be discussed below). Notice that when attributed to lowest $\mathbf{n} = \mathbf{1}$

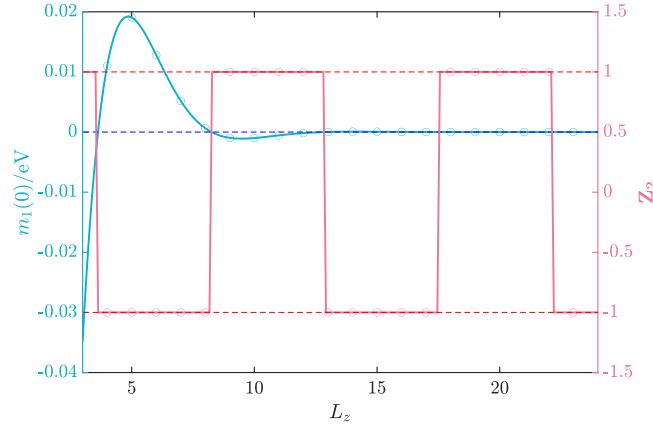


Figure 5: Finite size effect of an ultra-thin strong TI film (Dirac point at Γ) in the lattice model, revealed by the exponentially decaying oscillating gap $2\mathbf{m}_1(\mathbf{0})$ of surface Dirac cones and the oscillating \mathbb{Z}_2 index. The solid blue line of $\mathbf{m}_1(\mathbf{0})$ represents results from solving the self-consistent equations Eq. (20), while the circles are obtained from diagonalizing the TI film Hamiltonian at $\mathbf{k} = \mathbf{0}$ directly. The \mathbb{Z}_2 index is calculated from inversion symmetry indicator [64] method, and the solid red line represents index of $\mathbf{n} = \mathbf{1}$ block Dirac fermions with solved $\mathbf{m}_1(\mathbf{k})$, while circles are indexes calculated from TI film Hamiltonian directly.

371 block in Eq. (23), there is no constraint to force L_z to be integer from Eq. (20), and in this
 372 sense we continue the $\mathbf{n} = \mathbf{1}$ block from integer L_z to a positively real one. This is why
 373 we can do the calculation above. Again we emphasize that we will consider thick-enough
 374 strong TI film for topological phases hereafter, and the exponentially decaying finite size
 375 effect is physically negligible.

376 3 The quantum Hall conductivity of Dirac fermions

377 As stated, in both continuum model and lattice model, the strong topological insulator
 378 film is composed of two gapless Dirac fermions and countable gapped Dirac fermions. We
 379 have also claimed that all of the massive fermions inside are trivial, while saying nothing
 380 about the massless two. Here in this subsection, we shall complete the basic picture of
 381 them. Discussion here is restricted in effectively two-dimension and the zero-temperature
 382 limit.

383 3.1 In the continuum model

384 Our starting point is the continuum model of a two-band Dirac fermion appeared above

$$h_{\text{DF}}^{\text{C}} = \lambda \mathbf{k} \cdot \boldsymbol{\sigma} + m(\mathbf{k}) \sigma_z, \quad (28)$$

385 with $\mathbf{k} = (k_x, k_y)$ and $\boldsymbol{\sigma} = (\sigma_x, \sigma_y)$. Notice that the mass depends on $\mathbf{k} = |\mathbf{k}|$ and
 386 possesses a topologically trivial infinity behavior. Its Hall conductivity can be carried out
 387 by a deformed Kubo formula [27, 65], when the chemical potential μ lies at the valence
 388 band,

$$\sigma_H = -\frac{e^2}{h} \frac{1}{4\pi} \int d^2k \Theta(\mu + d) \frac{(\partial_{k_x} \mathbf{d} \times \partial_{k_y} \mathbf{d}) \cdot \mathbf{d}}{d^3}, \quad (29)$$

389 where $\mathbf{d}(\mathbf{k}) = (\lambda k_x, \lambda k_y, m(\mathbf{k}))$, $d = |\mathbf{d}|$, and to reveal possible topological property, we
 390 have used the Heaviside Theta function with $\Theta(\mathbf{x} > \mathbf{0}) = \mathbf{1}$ and zero otherwise, as the
 391 zero-temperature Fermi-Dirac distribution. The Hall conductivity can then be carried out
 392 easily by defining

$$\cos \theta = \frac{m}{(\lambda^2 k^2 + m^2)^{1/2}}, \quad (30)$$

393 and notice that

$$\frac{\sigma_H}{e^2/h} = \frac{1}{2} \int_{k_F}^{+\infty} dk^2 \frac{\partial \cos \theta}{\partial k^2}, \quad (31)$$

394 which finally leads to

$$\sigma_H = \frac{e^2}{2h} \left[\text{sgn}(m(+\infty)) - \frac{m(k_F)}{d(k_F)} \right], \quad (32)$$

395 with \mathbf{k}_F the Fermi vector determined by $\boldsymbol{\mu} = \mathbf{d}(\mathbf{k}_F)$, and $\text{sgn}(\mathbf{x})$ the sign function. From
 396 this equation, three topological phases are readily to be classified. Notice that we assume
 397 a path connected Fermi surface.

398 3.1.1 Gapless/Metallic case

399 The first case corresponds to a metallic phase with finite \mathbf{k}_F , and if $m(\mathbf{k}_F) = \mathbf{0}$ which
 400 leaves a perfect linearized dispersion near the Fermi surface, we obtain a half-quantized
 401 Hall conductance as

$$\sigma_H(\boldsymbol{\mu} | \mathbf{d}(\mathbf{k}_F) = \lambda \mathbf{k}_F) = \frac{e^2}{2h} \text{sgn}(m(+\infty)), \quad (33)$$

402 where the half-quantization is completely determined by the high-energy mass sign which
 403 may be recognized as the chirality assigned to the low-energy massless Dirac fermion near
 404 the Fermi surface. In our equivalent model, such a case exists for the $\mathbf{n} = \mathbf{1}$ bands

$$\mathbf{h}_{1,\chi} = \lambda_{\parallel}(\mathbf{k} \cdot \boldsymbol{\sigma}) + \chi \Theta(-m_0(\mathbf{k})) m_0(\mathbf{k}) \sigma_z, \quad \chi = \pm. \quad (34)$$

405 Since $m_0(\mathbf{k}) = m_0 - t_{\perp} k^2$, then by assuming $m_0 > 0, t_{\perp} > 0$, we have

$$\sigma_H^{1,\chi}(\mathbf{k}_F < \mathbf{k}_c) = -\chi \frac{e^2}{2h}, \quad (35)$$

406 with $\mathbf{k}_c = \sqrt{m_0/t_{\perp}}$ identified. For each gapless Dirac fermion, the exact half-quantization
 407 [4, 53] comes deeply from the parity ‘anomaly’ [47, 66–71], which manifests itself as an
 408 explicit symmetry breaking term at high energy for a low energetically massless 2D Dirac
 409 fermion. To be more clearer, the 2D parity symmetry is indeed an in-plane Mirror symme-
 410 try [31], say about \mathbf{x} , which forces $(\mathbf{k}_x, \mathbf{k}_y) \xrightarrow{\mathcal{M}_x} (\mathbf{k}_x, -\mathbf{k}_y)$, and in our model, the projected
 411 spin degrees of freedom makes the related unitary transformation to be $\mathbf{U}_{M_x} = \boldsymbol{\sigma}_x$, then
 412 the imposed parity symmetry $\mathbf{U}_{M_x}^{\dagger} \mathbf{h}(\mathbf{k}) \mathbf{U}_{M_x} = \mathbf{h}(\mathcal{M}_x \mathbf{k})$ stands only when $\mathbf{k} < \mathbf{k}_c$, which
 413 forms a parity invariant regime (PIR) inside which the parity symmetry is respected. The
 414 parity invariant regime is recognized as the low energy zone around the Dirac point with
 415 small \mathbf{k} , and for larger $\mathbf{k} > \mathbf{k}_c$ recognized as the high energy zone, the non-vanishing mass
 416 term breaks the 2D parity symmetry explicitly, as a consequence of regulating the effective
 417 low energy theory [55].

418 3.1.2 Insulating case

419 The remaining two phases are insulating with $\mathbf{k}_F = \mathbf{0}$ recognized when the chemical po-
420 tential lies inside the global insulating gap, then simply

$$\sigma_H(|\mu| < d_{\min}) = \frac{e^2}{2h} [\text{sgn}(m(+\infty)) - \text{sgn}(m(\mathbf{0}))], \quad (36)$$

421 for a Dirac cone, where $d_{\min} = \min(d(\mathbf{k}))$ denotes the bound of the global gap. And
422 clearly $\sigma_H/(e^2/h) = \mathbf{0}, \pm 1$ appears notifying trivial or non-trivial phases depending on the
423 relative signs of low and high energy masses, with the ± 1 cases identified as the Chern
424 insulator or equivalently, the quantum anomalous Hall effect. In our equivalent model,
425 one sees from Fig. 2 that all $n \geq 2$ masses contains the same sign, and the corresponding
426 Dirac cones are all trivial. And we come back to the statement that in a TI film, there
427 are two gapless Dirac fermions with opposite half-quantized Hall conductance, while all
428 other bands forming paired trivial massive Dirac fermions. The quantized nature of the
429 Hall conductance in insulating system, $\sigma_H = -C e^2/h$, is referred to the famous TKNN
430 theorem [10], with its robustness against continuous non-gap-closing perturbation rooted
431 in the topological nature of C as the Chern invariant [72, 73].

432 3.2 In the lattice model

433 Now we turn to the lattice model with a starting Dirac Hamiltonian defined on the lattice

$$\mathbf{h}_{\text{DF}}^L = \lambda(\sin(k_x)\sigma_x + \sin(k_y)\sigma_y) + m(\mathbf{k})\sigma_z. \quad (37)$$

434 Firstly we notice that when $\mathbf{m} \equiv \mathbf{0}$, the remaining part is a naive lattice realization of single
435 Weyl fermion, which is strongly constrained by the Nielsen-Ninomiya theorem [29, 30].
436 And there appears to be four connected Dirac points at $\Gamma, \mathbf{X}, \mathbf{Y}, \mathbf{M}$, respectively. Any non-
437 vanishing $\mathbf{m}(\mathbf{k})$ will serve as a lattice regularization of the theory, with only difference
438 as its effectiveness upon gapping which Dirac point. Essentially, here the difference with
439 a continuum model appears, say in the latter case there is only a single gapless Dirac
440 cone, and the infinity is usually treated by one-point compactification and the \mathbf{k} -space is
441 topologically equivalent to a sphere surface \mathbf{S}^2 , while on lattice the Brillouin zone geometry
442 as a torus \mathbf{T}^2 can contain non-trivial property on its periodic boundary. Such a non-trivial
443 property is exactly reflected by the existence of four Dirac points under naive lattice
444 realization of Dirac operator $\mathbf{k} \cdot \boldsymbol{\sigma}$. With an analogical formulation, we write

$$\sigma_H = \frac{e^2}{2h} [S_X + S_Y - S_\Gamma - S_M], \quad (38)$$

445 with $S_{\mathbf{k}}$ an analogy to $\mathbf{m}(\mathbf{k})/d(\mathbf{k})$ appeared in the continuum model. $S_{\mathbf{k}}$ becomes zero when
446 the chemical potential lies in the metallic states around \mathbf{k} , and over those states certain
447 symmetry constraint is imposed in a finite regime around, such as the parity symmetry
448 which requires $\mathbf{m}(\mathcal{M}_x \mathbf{k}) = -\mathbf{m}(\mathbf{k})$, and essentially, the imposed symmetry should ensure
449 that the net Berry curvature integral contributed from the regime (constrained also by
450 chemical potential) is zero wherever we put the Fermi level inside. On the other hand, we
451 recognize $S_{\mathbf{k}} = \text{sgn}(\mathbf{m}(\mathbf{k}))$ when Dirac point \mathbf{k} is gapped, and the Fermi level lies inside.
452 The formula is further classified into two cases under additional conditions.

453 3.2.1 Gapless/Metallic case

454 The first case corresponds to the existence of gapless Dirac fermion(s) inside a parity
455 invariant regime. Give an example as a single gapless Dirac fermion at Γ point, let the

456 Fermi level lie in the symmetry constrained regime (SCR), and we recognize

$$\sigma_H(\mathbf{k}_F \subseteq \text{SCR}) = \frac{e^2}{2h} [\text{sgn}(m(X)) + \text{sgn}(m(Y)) - \text{sgn}(m(M))], \quad (39)$$

457 which is always half-quantized. Notice that $\mathbf{k}_F = \{\mathbf{k} | d(\mathbf{k}) = \mu\}$ is now a set, representing
 458 Fermi surface wavevectors. Also notice that unlike the case in the continuum model where
 459 the regulator comes from only at infinity, here on the square lattice, a single gapless Dirac
 460 fermion owns **three** regulators. At the same time, if $\text{sgn}(m(X)) = \text{sgn}(m(Y)) = \text{sgn}(m(M))$
 461 is recognized which makes the boundary of the Brillouin zone trivial, we get

$$\sigma_H(\mathbf{k}_F \subseteq \text{SCR}) = \frac{e^2}{2h} \text{sgn}(m(M)). \quad (40)$$

462 In our equivalent model on lattice, the lowest two cones

$$h_{1,\chi}(\mathbf{k}) = \lambda_{\parallel} (\sin(k_x a) \sigma_x + \sin(k_y b) \sigma_y) + \chi m_1(\mathbf{k}) \sigma_z, \quad (41)$$

463 satisfy the condition, with $m_1(\mathbf{k}) = \Theta(-m_0(\mathbf{k}))m_0(\mathbf{k})$ identified. Since under our model
 464 parameter choice, it is easy to verify that $\text{sgn}(m_1(X)) = \text{sgn}(m_1(Y)) = \text{sgn}(m_1(M)) < 0$,
 465 and we write

$$\sigma_H^{1,\chi}(m_1(\mathbf{k}_F) > 0) = -\chi \frac{e^2}{2h}, \quad (42)$$

466 inside the symmetry constrained regime which is now the parity invariant regime defined
 467 by $m_0(\mathbf{k}) > 0$.

468 3.2.2 Insulating case

469 The second case corresponding to a globally gapped Dirac band. Now by requiring the
 470 chemical potential to lie inside the gap, the Chern number reads

$$C = \frac{1}{2} [\text{sgn}(m(\Gamma)) + \text{sgn}(m(M)) - \text{sgn}(m(X)) - \text{sgn}(m(Y))], \quad (43)$$

471 which ranges among $0, \pm 1, \pm 2$. This formula has two common versions that we will come
 472 up with in the following. The first version is the most familiar one with a trivial Brillouin
 473 boundary when $\text{sgn}(m(X)) = \text{sgn}(m(Y)) = \text{sgn}(m(M))$ is recognized, and

$$C = \frac{1}{2} [\text{sgn}(m(\Gamma)) - \text{sgn}(m(M))]. \quad (44)$$

474 The mass term generating this formula, is usually written as

$$m(\mathbf{k}) = m_0 - 4t \left(\sin^2 \frac{k_x}{2} + \sin^2 \frac{k_y}{2} \right), \quad (45)$$

475 with a relatively small $|m_0|$ compared to $|t|$, and correspondingly, we have

$$C = \frac{1}{2} [\text{sgn}(m_0) + \text{sgn}(t)], \quad (46)$$

476 which is non-trivial with unit Chern number when $m_0 t > 0$. And when we relax the value
 477 of m_0 , a better formula for this mass term is

$$C = -\frac{\text{sgn}(m(X))}{2} [\text{sgn}(m(\Gamma)) - \text{sgn}(m(M))]. \quad (47)$$

478 In our equivalent model on lattice within our parameter choice as a strong topological
 479 insulator with homogeneous in-film-plane parameters, Eq. (44) is enough to describe all
 480 $n \geq 2$ massive Dirac fermions; and since from Fig. 4, all $m_{n \geq 2}(\mathbf{k})$ do not change sign at Γ
 481 and M , they are evidently all trivial.

482 3.3 A glance in proof of half-quantization

483 The proof [4, 31] for the half-quantization of a general band structure in 2D comes as
 484 follows, with a requirement of parity or time reversal symmetry at the Fermi surface.
 485 Without losing generality we consider connected Fermi surface. Recognizing the infinity
 486 as one point compactifies the \mathbf{k} -space, then the existence of Fermi surface cuts the curvature
 487 integral into two parts with three boundaries where the Stokes theorem applies

$$\frac{-2\pi\sigma_H}{e^2/h} = \oint_{\text{FS}} \mathbf{dk} \cdot \text{Tr}(A^M) + \oint_{\text{FS}} \mathbf{dk} \cdot \text{Tr}(A^L) + \oint_{\overline{\text{FS}}} \mathbf{dk} \cdot \text{Tr}(\tilde{A}^L), \quad (48)$$

488 where A^M refers to non-Abelian Berry connection (convention follows that $\mathcal{A} = i \langle \mathbf{u} | \mathbf{d} | \mathbf{u} \rangle$)
 489 formed by the metallic bands crossed by the Fermi surface with parity or time-reversal
 490 symmetry, while A^L refers to connection of bands with lower energy, on the boundary
 491 formed by \mathbf{k}_F . Essentially, the last two terms are phase integrals around one mutual
 492 boundary with opposite orientations, which will contribute an integer value [74–76] $2\pi\mathbf{C}$.
 493 For the first term, requiring the 2D parity (i.e., mirror) symmetry at the Fermi surface
 494 leads to local unitary transformation U_k^M relating states at parity-symmetric points, which
 495 leads to

$$A_\mu^M(\mathbf{k}) = i(U_k^M)^\dagger \partial_{k_\mu} U_k^M + (U_k^M)^\dagger A_\nu^M(\mathcal{M}\mathbf{k}) U_k^M J_{\nu\mu}, \quad (49)$$

496 where $J_{\nu\mu} = \partial(\mathcal{M}\mathbf{k})_\nu / \partial k_\mu$ is the Jacobian matrix with $\det(J) = -1$. And similarly,
 497 requiring time reversal at Fermi surface leads to

$$A_\mu^M(\mathbf{k}) = i(U_k^T)^\dagger \partial_{k_\mu} U_k^T - (U_k^T)^\dagger A_\mu^M(-\mathbf{k}) U_k^T, \quad (50)$$

498 where U_k^T is the unitary matrix relating time reversal points satisfying that $U_k^T = -(U_{-\mathbf{k}}^T)^T$.
 499 Performing Berry phase loop integral of both sides leads to, for both symmetry restricted
 500 cases,

$$\oint_{\text{FS}} \mathbf{dk} \cdot \text{Tr}(A^M) = \frac{i}{2} \oint_{\text{FS}} \mathbf{dk} \cdot \text{Tr}(U_k^\dagger \nabla_k U_k) = \pi N. \quad (51)$$

501 Combining three terms gives

$$\sigma_H = -\frac{e^2}{h} \left(C + \frac{N}{2} \right), \quad (52)$$

502 with both \mathbf{C} and \mathbf{N} integers. The proof here can be easily generalized to the lattice model,
 503 with simply replacing the base manifold by a torus, and to the case when the Fermi surface
 504 consists of several separately connected components, with the curvature integral cut into
 505 more parts determined by Fermi surface position in \mathbf{k} -space.

506 When bands related to \mathbf{C} and \mathbf{N} are fully separated, the former can be recognized as
 507 the Chern number contributed from these fully occupied bands, while the latter reduces
 508 to a quantized Fermi surface loop integral over metallic bands [77–80]. We would like to
 509 emphasize here that even though reduced to cumulating low energy (refer to Fermi surface
 510 here) quantities, the \mathbf{N} index in our analysis has to be determined by the properties of far
 511 Fermi sea, i.e., high energy regime. This is because the application of the Stokes theorem,
 512 which turns the Fermi sea volume integral over Berry curvature into Fermi surface line
 513 integral over Berry phase, requires a self-consistent gauge choice of the vector field. This
 514 gauge choice must not contain any singularities in the integrated volume, in order to ensure
 515 the existence of a non-singular gauge field throughout the volume.

3.4 View from field theory

The gapless Dirac fermion in a strong topological insulator film can be written as $\mathcal{H}_0(\mathbf{k}) = \lambda_{\parallel} \boldsymbol{\sigma} \cdot (\sin k_x, \sin k_y) + m(\mathbf{k}) \sigma_z$ with $m(\mathbf{k}) = \Theta(-m_0(\mathbf{k})) m_0(\mathbf{k})$ identified, which is constructed on lattice with finite 2D Brillouin zone. The time-ordered Green function is $\mathcal{G}_0(\mathbf{k}) = [\boldsymbol{\omega} - \mathbf{d} \cdot \boldsymbol{\sigma} (1 - i\eta)]^{-1}$ where $\mathbf{k}_{\mu} = (\boldsymbol{\omega}, \mathbf{k})_{\mu}$, $\mathbf{d}(\mathbf{k}) = (\lambda_{\parallel} \sin k_x, \lambda \sin k_y, m(\mathbf{k}))$ and η is infinitesimal small quantity. In order to study a linear electromagnetic response in the film system, we include the electromagnetic fields \mathcal{A} which are coupled to the current through the interaction term $\mathcal{H}_{\text{gauge}} = \mathbf{j} \cdot \mathcal{A}$. The electric current density operator in the momentum space is given by $\mathbf{j} = \nabla_{\mathbf{k}} \mathcal{G}_0^{-1}(\mathbf{k})$. With the electromagnetic fields, the action reads ($e = \hbar = 1$)

$$S = \int_{\mathbf{k}} \psi_{\mathbf{k}}^{\dagger} \mathcal{G}_0^{-1}(\mathbf{k}) \psi_{\mathbf{k}} + \int_{\mathbf{k}} \int_{\mathbf{q}} \mathcal{A}^{\mu}(\mathbf{q}) \psi_{\mathbf{k}+\mathbf{q}/2}^{\dagger} \partial_{\mathbf{k}_{\mu}} \mathcal{G}_0^{-1}(\mathbf{k}) \psi_{\mathbf{k}-\mathbf{q}/2}, \quad (53)$$

where $\int_{\mathbf{k}} = \int \frac{d\boldsymbol{\omega}}{2\pi} \int_{\text{BZ}} \frac{d^2\mathbf{k}}{(2\pi)^2}$ and the momentum \mathbf{k} integral is performed over the whole 2D Brillouin zone. By integrating out the fermions in the action, the effective action for gauge fields $S_{\text{eff}}[\mathcal{A}]$ can be obtained by expanding to the quadratic order

$$S_{\text{eff}} = \frac{1}{2} \int \frac{d^3\mathbf{q}}{(2\pi)^3} \mathcal{A}^{\mu}(-\mathbf{q}) \Pi_{\mu\nu}(\mathbf{q}) \mathcal{A}^{\nu}(\mathbf{q}). \quad (54)$$

where μ, ν run over the space-time indices $(0, 1, 2)$ with the vacuum polarization operator defined as

$$i\Pi_{\mu\nu}(\mathbf{q}) = \int \frac{d^3\mathbf{k}}{(2\pi)^3} \text{Tr}[\partial_{\mathbf{k}_{\mu}} \mathcal{G}_0^{-1}(\mathbf{k}) \mathcal{G}_0(\mathbf{k} + \mathbf{q}/2) \partial_{\mathbf{k}_{\nu}} \mathcal{G}_0^{-1}(\mathbf{k}) \mathcal{G}_0(\mathbf{k} - \mathbf{q}/2)], \quad (55)$$

There is no divergence in $\Pi_{\mu\nu}$ as the momentum integral is performed over a finite Brillouin zone due to the lattice regularization. The antisymmetric terms $\Pi_{\mu\nu}^A(\mathbf{q})$ can be evaluated as follows

$$\Pi_{\mu\nu}^A = \frac{1}{2\pi} \epsilon_{\mu\nu\zeta} \mathbf{q}^{\zeta} C, \quad (56)$$

with Chern number in the case following definition that

$$C = \int_{\text{BZ}} \frac{d^2\mathbf{k}}{4\pi} \hat{\mathbf{d}} \cdot \partial_{k_x} \hat{\mathbf{d}} \times \partial_{k_y} \hat{\mathbf{d}}, \quad (57)$$

where $\epsilon_{\mu\nu\zeta}$ is Levi-Civita symbol and $\hat{\mathbf{d}} = \mathbf{d}/|\mathbf{d}|$. Finally we obtain the Chern-Simons theory for \mathcal{A}_{μ}

$$S_{\text{eff}}[\mathcal{A}] = \frac{C}{2\pi} \int d^3x \epsilon^{\mu\nu\zeta} \mathcal{A}_{\mu} \partial_{\zeta} \mathcal{A}_{\nu}. \quad (58)$$

For the lattice Hamiltonian $\mathcal{H}_0(\mathbf{k})$, we have $C = -\frac{\text{sgn}(m(\pi, \pi))}{2}$ which is a half-integer with its sign determined by the sign of $m(\pi, \pi)$. Restoring physical units, the Chern-Simons term corresponds a half quantum Hall effect

$$\langle j^{\nu} \rangle = \frac{\delta S_{\text{eff}}}{\delta \mathcal{A}_{\nu}} = \frac{\text{sgn}(m(\pi, \pi)) e^2}{2} \frac{e^2}{h} \epsilon^{\mu\nu\zeta} \partial_{\zeta} \mathcal{A}_{\mu}. \quad (59)$$

Notice that upon DC linear response, the result is strict.

If we now focus on the low-energy effective model of the lattice four-band Hamiltonian by neglecting higher energy states ($\propto m(\mathbf{k})$), which can be expressed as $\mathcal{H}_0^{\text{low}}(\mathbf{k}) = \lambda(\mathbf{k}_x \boldsymbol{\sigma}_1 + \mathbf{k}_y \boldsymbol{\sigma}_2)$.

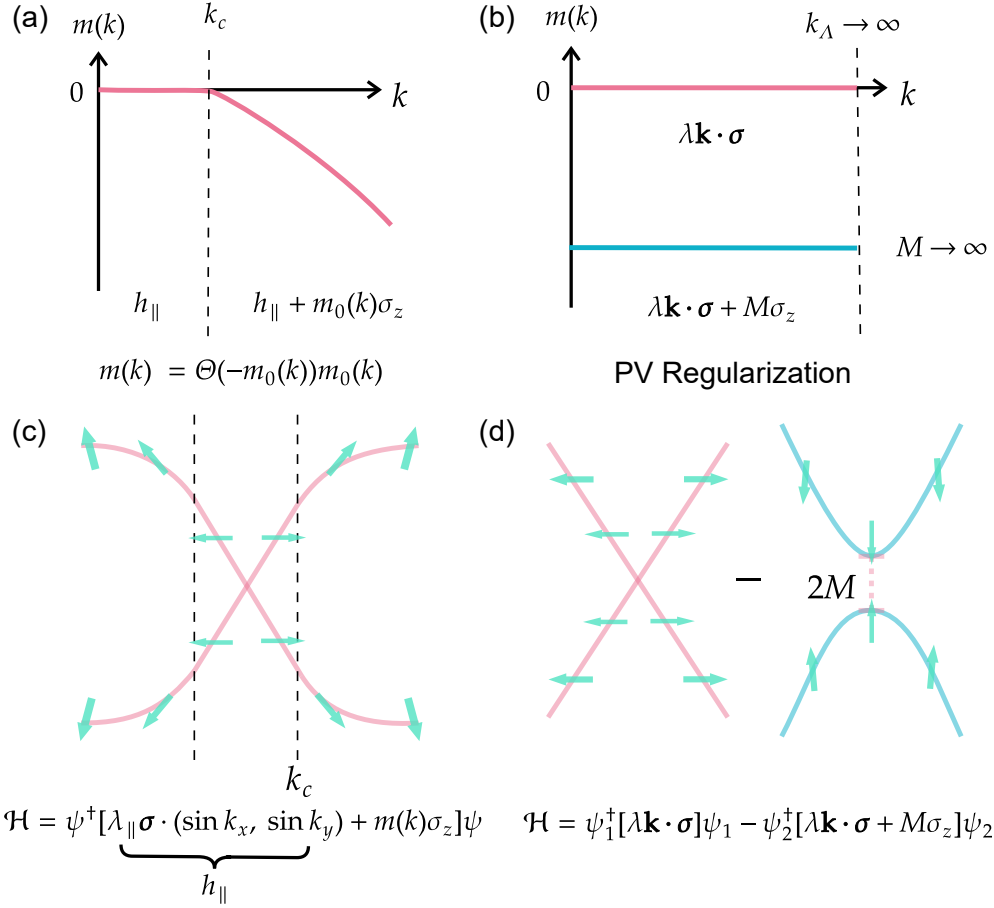


Figure 6: Regulated gapless Dirac fermion on lattice and by Pauli-Villars regularization. (a) Momentum dependent mass of regulated gapless Dirac fermion on lattice, \mathbf{k}_c is defined by $\mathbf{m}_0(\mathbf{k}) = \mathbf{0}$, which splits the mass and the dispersion in (c) of the Dirac fermion into two regions, low energy part with $\mathbf{k} < \mathbf{k}_c$ and high energy part with $\mathbf{k} > \mathbf{k}_c$. (b) Mass of massless Dirac fermion and of its regulator partner by Pauli-Villars treatment. (c) Dispersion of regulated gapless Dirac fermion on lattice with spin orientation. (d) Dispersion of double Dirac fermions, one massless and one massive under Pauli-Villars regularization, and to obtain convergent result, contributions from two fermions should be subtracted.

543 There is a linear ultraviolet divergence in $\Pi_{\mu\nu}(\mathbf{q})$ which should be regularized by Pauli-
 544 Villars method in a gauge-invariant way. In the Pauli-Villars regularization approach, we
 545 need to introduce a second Dirac field mass $M\sigma_3$. In the limit ($M \rightarrow \infty$), the regulator
 546 field decouples from the theory, which removes the divergence in $\Pi_{\mu\nu}$, leaving a finite
 547 contribution for the crossed polarization tensor $\Pi_{\mu\nu} = \frac{\text{sgn}(M)}{4\pi} \epsilon_{\mu\nu\zeta} \mathbf{q}^\zeta$. This also induces a
 548 Chern-Simons term and corresponds to a half-quantum Hall effect.

549 The comparison of mass configuration and band dispersion of two methods are put in
 550 Fig. 6. The advantage of our approach for lattice realization single gapless Dirac fermion
 551 lies in its reality, as it appears naturally in a topological insulator film, and also in its
 552 conciseness of expressing topological property with a single analytical mass term. The
 553 price here, however, is to introduce symmetry breaking term at high energy zone explicitly,
 554 and the form of Theta function (or its mollifier) will introduce long range hopping in real
 555 space.

556 3.5 Unexchangeable limits

557 In the usual context of quantum field theory, a massive $(2+1)$ -D Dirac fermion bears
 558 half-quantized Hall conductivity when the chemical potential lies inside the gap, even if
 559 the mass is infinitesimally small [14, 68, 70], under which one gets in fact a Dirac point.
 560 Such a picture relies on the limit sequence that one firstly takes $\mu \rightarrow 0$, and then the mass
 561 $m \rightarrow 0$, while on the other hand, once the sequence is inverted, say at first place, one stays
 562 at finite chemical potential μ and takes $m \rightarrow 0$, which leads to zero Hall conductivity, one
 563 gets constant zero Hall plateau when pushing $\mu \rightarrow 0$. And in this sense one realizes that
 564 a gapless Dirac point is singular, and different approaches to reach it will lead to different
 565 and even contradictory pictures.

566 The same thing happens in our model. Consider now a gapless Dirac fermion is
 567 perturbed by a small constant mass term

$$h = \lambda_{\parallel}(\mathbf{k} \cdot \boldsymbol{\sigma}) + [\delta m + \Theta(-m_0(\mathbf{k}))m_0(\mathbf{k})]\sigma_z, \quad (60)$$

568 where for simplicity we discuss in the continuum model here. Given $m_0(\mathbf{k}) = m_0 - b\mathbf{k}^2$
 569 with $m_0 b > 0$, by Eq. (32) we have

$$\sigma_H = -\frac{e^2}{2h} \left[\text{sgn}(b) + \frac{\delta m}{\sqrt{\lambda_{\parallel}^2 k_F^2 + \delta m^2}} \right], \quad (61)$$

570 where a small μ near the Dirac point is assumed. The \mathbf{k}_F refers to the Fermi wavevector
 571 defined by $\mu = -\sqrt{\lambda_{\parallel}^2 k_F^2 + \delta m^2}$, inside the valence band and satisfies $m_0(\mathbf{k}_F) > 0$. Now
 572 the two different limits for the Hall conductivity of the gapless Dirac cone in the case read
 573

$$\lim_{\delta m \rightarrow 0} \lim_{\mu \rightarrow 0} \sigma_H = -\frac{e^2}{2h} [\text{sgn}(b) + \text{sgn}(\delta m)], \quad (62a)$$

$$\lim_{\mu \rightarrow 0} \lim_{\delta m \rightarrow 0} \sigma_H = -\frac{e^2}{2h} \text{sgn}(b), \quad (62b)$$

574 i.e., firstly pushing chemical potential to zero and then pushing δm to zero leads an
 575 undefined limit that depends on the limit direction δm takes (positive or negative), while
 576 an admittedly infinitesimal mass gap will not affect the half-quantization of the gapless
 577 Dirac cone by subsequent Fermi level tuning — not only to $\mu \rightarrow 0$ but for all possible

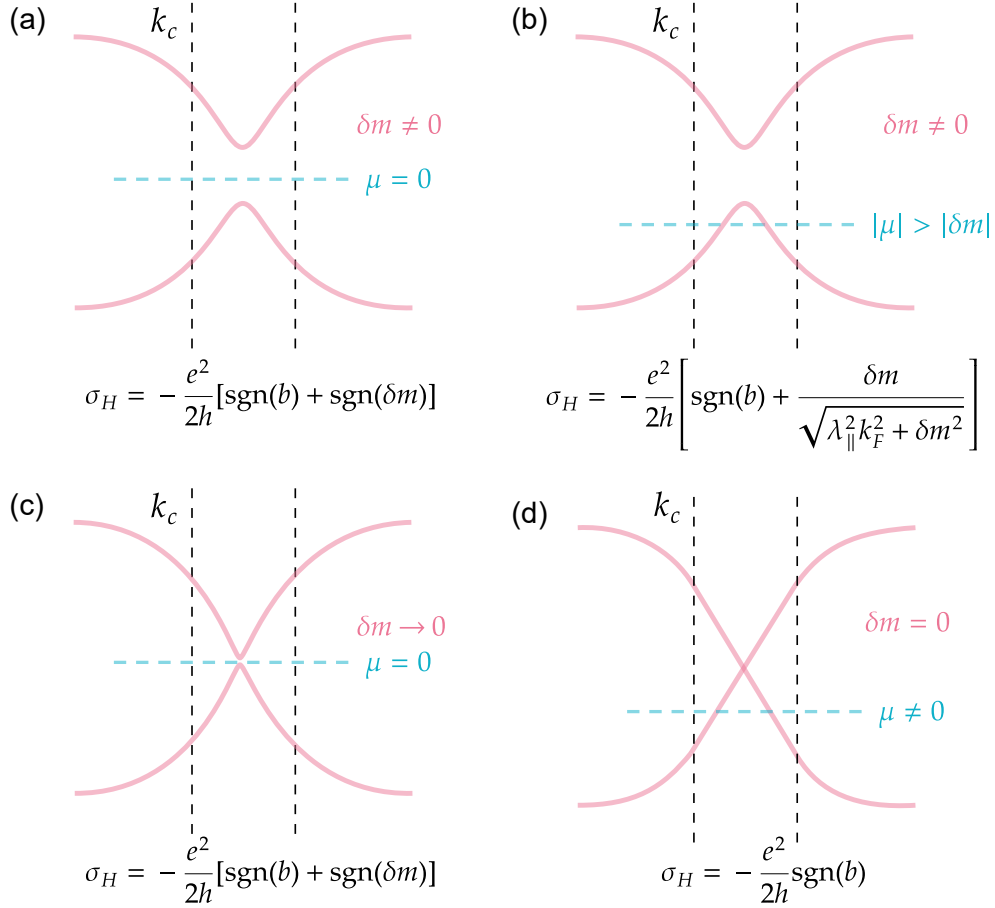


Figure 7: Schematic diagrams illustrating the limits in calculating the Hall conductivity of a regulated gapless Dirac fermion are shown below. In these diagrams, $\mathbf{k}_c = \sqrt{m_0/b}$. (a) Initially tuning the chemical potential to $\mu = 0$ leads to integer quantized Hall conductivity. (b) Initially adjusting the chemical potential finite inside the valence band with Fermi wavevector $\mathbf{k}_F < \mathbf{k}_c$ results in an unquantized Hall conductivity asymptotically proportional to $\delta m/k_F$. (c) Continuing from (a), pushing the small gap $\delta m \rightarrow 0$ while pinning the chemical potential at $\mu = 0$ leaves the integer of the quantized Hall conductivity invariant. (d) Continuing from (b), pushing the small gap $\delta m \rightarrow 0$ while keeping the finite chemical potential inside the valence band with $\mathbf{k}_F < \mathbf{k}_c$ leads to half-quantized Hall conductivity of a gapless Dirac fermion, with the sign of the Hall conductivity determined by its chirality or equivalently its high energy mass sign.

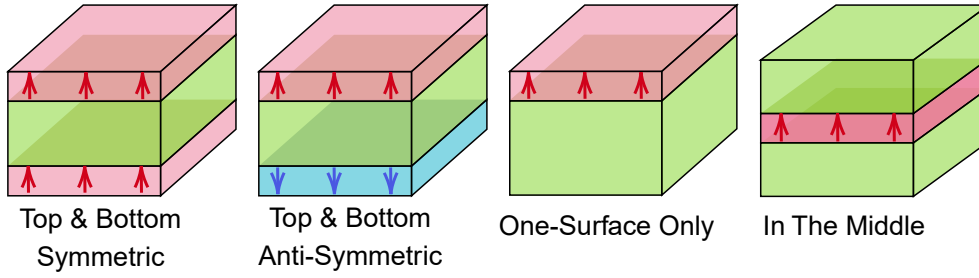


Figure 8: Several basic representative magnetic topological insulator heterostructures. From left to right: Zeeman field at top and bottom surfaces with parallel and anti-parallel polarizations, at top surface and in the middle only, corresponding to basic topological phases in magnetic topological insulator film as Chern insulator, axion insulator, half-quantized anomalous Hall effect, and metallic quantized anomalous Hall effect, respectively. We use color and its gradation to emphasize the direction and strength of the Zeeman field.

578 Fermi wavevectors that lie inside the parity invariant regime [31] defined by $\mathbf{m}_0(\mathbf{k}) > \mathbf{0}$.
 579 The corresponding schematic diagram illustrating the sequential limit taking processes
 580 upon evaluating the Hall conductivity of a regulated gapless Dirac fermion is presented
 581 in Fig. 7. In reality, which limit the measured Hall conductance takes has to depend on
 582 specific situation of the system, while for the Dirac point emerged in a purely magnetic
 583 TI, the second perspective may be deemed more realistic.

584 4 Magnetic and orbital fields in topological insulator films

585 In this section we consider more ingredients, such as exchange interaction, gate-voltage
 586 and orbital orders, to play their roles in the topological insulator film at the mean-field
 587 level. We identify the mean field to be $\mathbf{V}(\mathbf{k}, \mathbf{l}_z)\sigma_\mu\tau_\nu$, with single in plane wavevector and
 588 out of plane position dependence, and transform the field into the Dirac fermion represen-
 589 tation. For instance, an induced \mathbf{z} -Zeeman field $V_z(\mathbf{l}_z)\sigma_z\tau_0$ with solely \mathbf{z} -dependence and
 590 intrinsic spin-orbital coupling $H_{\parallel}(\mathbf{k})$ that only depend on \mathbf{k} are two special cases under
 591 the formulation. For our interest, we will mainly consider magnetic exchange interaction
 592 that has been approximated to affect as an effectively mean-field Zeeman field [81] along \mathbf{z}
 593 direction, and transformation over other spin and orbital related fields are discussed and
 594 summarized later.

595 4.1 Magnetism polarized along \mathbf{z} direction

596 The stated mean \mathbf{z} -Zeeman field is assumed to be uniform intralayer while varies with \mathbf{l}_z ,
 597 and that is to say [32],

$$v_Z(\mathbf{k}) = \sum_{\mathbf{l}_z, k} \Psi_{\mathbf{l}_z, k}^\dagger V_Z(\mathbf{l}_z) \Psi_{\mathbf{l}_z, k}, \quad (63)$$

598 where

$$V_Z(\mathbf{l}_z) \equiv V_z(\mathbf{l}_z)\sigma_z\tau_0, \quad (64)$$

599 which acts on spin \mathbf{z} . For several schematic examples with different Zeeman configura-
 600 tions, see Fig. 8. Its equivalent action by projection $\langle \Phi_m^n | V_Z | \Phi_{m'}^{n'} \rangle$ ($m, m' = 1, 2, 3, 4$;
 601 $n, n' = 1, \dots, L_z$) reads

$$\mathbf{V}(\mathbf{k}) = (\mathbf{I}_S(\mathbf{k})\tau_0 - \mathbf{I}_A(\mathbf{k})\tau_y) \sigma_z. \quad (65)$$

602 In the expression, two projected Hermitian matrices $\mathbf{I}_{S/A}(\mathbf{k})$ have been defined with ele-
603 ments

$$\mathbf{I}_S^{nn'} = |C_n C_{n'}| \sum_{l_z} V_z(l_z) [\lambda_\perp^2 (f_+^n)^* f_+^{n'} + t_\perp^2 \eta^n \eta^{n'} (f_-^n)^* f_-^{n'}] = (\mathbf{I}_S^{n'n})^*, \quad (66a)$$

$$i\mathbf{I}_A^{nn'} = i|C_n C_{n'}| \sum_{l_z} V_z(l_z) \lambda_\perp t_\perp [\eta^{n'} (f_+^n)^* f_-^{n'} + \eta^n (f_-^n)^* f_+^{n'}] = -i(\mathbf{I}_A^{n'n})^*, \quad (66b)$$

604 where $\mathbf{n}, \mathbf{n}' = \mathbf{1}, \dots, L_z$. Notice that $\mathbf{I}_{S/A}$ is non-vanishing only when the symmetric/antisymmetric
605 component of V_z is non-zero. Our formula then illustrates that the Zeeman field in a TI
606 film is brought into two classes by the discrete parity or mirror symmetry, with \mathbf{S} (\mathbf{A})
607 labelling the part respects (disrespects) this symmetry. Bring the transformed Zeeman
608 term into multi-Dirac fermions representation, we obtain

$$\mathbf{H}^V = \bigoplus_{n=1}^{L_z} [\lambda_\parallel (\sin(k_x a) \sigma_x + \sin(k_y b) \sigma_y) + m_n(k) \tau_z \sigma_z] + (\mathbf{I}_S(k) \tau_0 - \mathbf{I}_A(k) \tau_y) \sigma_z. \quad (67)$$

609 Under the local unitary transformation, the Zeeman field in TI film undergoes a trans-
610 formation into the \mathbf{I} matrices, which act as generalized Higgs fields in matrix form, gener-
611 ating mass through the Yukawa-like couplings among Dirac fermions in the film [55, 82].
612 This phenomenon occurs precisely due to the fact that the projected Zeeman terms still
613 act on spin- \mathbf{z} component, similar to how masses affect the system. The emergence of a
614 non-vanishing Higgs expectation value is closely associated with the establishment of the
615 magnetic order in the system, either by intrinsic spontaneous magnetization or a proximate
616 magnetic field.

617 A closer looking then classifies this action into three aspects. Firstly, the intra-Dirac
618 cone elements \mathbf{I}_S^{nn} tell how the Zeeman field directly modifies the mass term m_n , and
619 due to the trace invariance under unitary transformation, such a direct modification is
620 significant in understanding the impact of the Zeeman field on the overall mass generation
621 process. Secondly, the intra-block inter-Dirac cone elements \mathbf{I}_A^{nn} terms couple the two
622 mirror-symmetric Dirac fermions with the same \mathbf{n} -label together, and forces them to re-
623 combine into two new Dirac fermions that break the mirror symmetry. Finally, the general
624 inter-block elements $\mathbf{I}_{S/A}^{nn'} (\mathbf{n} \neq \mathbf{n}')$ couple Dirac cones with different \mathbf{n} -labels. Nevertheless,
625 since the winding part of Dirac fermions in our equivalent TI film model (see Eq. (67)) is
626 identity in subspace spanned by \mathbf{n} and $\boldsymbol{\tau}$, the total effect of the projected Zeeman term is
627 to modify the mass terms, i.e.,

$$\mathbf{M}(k) \sigma_z = \left[\bigoplus_{n=1}^{L_z} m_n \tau_z + \mathbf{I}_S \tau_0 - \mathbf{I}_A \tau_y \right] (k) \sigma_z, \quad (68)$$

628 and further diagonalization of this total mass part will give another set of $2L_z$ mass terms
629 without affecting the winding part, i.e.,

$$\mathbf{M}(k) \xrightarrow{\text{diagonalization}} \bigoplus_{n=1}^{2L_z} \tilde{m}_n(k), \quad (69)$$

630 and accordingly, we can write down the Dirac fermion Hamiltonian under Zeeman field as

$$\tilde{\mathbf{H}}(k) = \bigoplus_{n=1}^{2L_z} [\lambda_\parallel (\sin(k_x a) \sigma_x + \sin(k_y b) \sigma_y) + \tilde{m}_n(k) \sigma_z], \quad (70)$$

631 which describes the $2L_z$ Dirac fermions in a magnetic topological insulator film. Notice
 632 that the Zeeman term alters the mass of Dirac fermions thus their topology, which is the
 633 origin of the fruitful magnetic topological phases in the system.

634 The formula and discussion above are general and applies for any \mathbf{z} -varying Zeeman
 635 configurations. For our consideration here, we separately discuss main cases.

636 4.1.1 Uniform field strength

637 In this case $\mathbf{V}_z(l_z) \equiv V$ for any l_z , and it is easy to check out that

$$I_S^{nn'} = V\delta_{nn'}, \quad (71a)$$

$$I_A^{nn'} = \mathbf{0}, \quad (71b)$$

638 which offers us with an exact projection without further diagonalization as

$$H^V(\mathbf{k}) = \bigoplus_{n=1}^{L_z} [\lambda_{\parallel}(\sin(k_x a)\sigma_x + \sin(k_y b)\sigma_y) + (m_n(k)\tau_z + V\tau_0)\sigma_z] = h_{n,\chi}^V(\mathbf{k}), \quad (72)$$

639 where each sub-block

$$h_{n,\chi}^V(\mathbf{k}) = \lambda_{\parallel}(\sin(k_x a)\sigma_x + \sin(k_y b)\sigma_y) + (\chi m_n(k) + V)\sigma_z, \quad (73)$$

640 describes a Dirac fermion of TI film modified by a uniform Zeeman splitting V . This
 641 formula serves as a clear physical picture to illustrate the formation of higher Chern
 642 number in TI film, with multi-sub-bands inversion [83] generated by the direct Higgs
 643 coupling V , as we shall illustrate in the section thereafter.

644 4.1.2 Weak Zeeman field

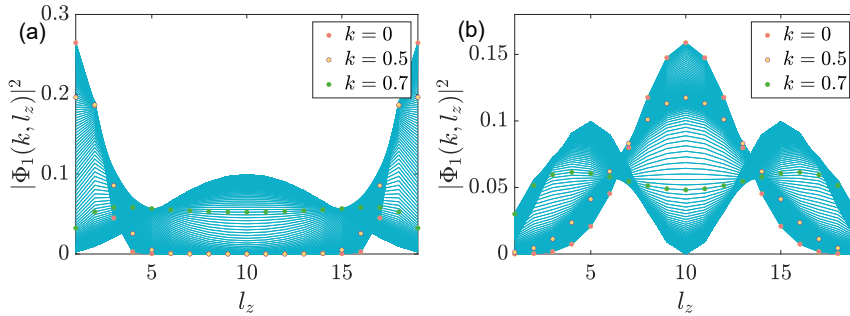


Figure 9: Basis wavefunction distribution along \mathbf{z} for (a) $n = 1$ and (b) $n = 2$, varying from $\mathbf{k}_x = \mathbf{0}$ to $\mathbf{k}_x = \pi$ with $\mathbf{k}_y = \mathbf{0}$. Dots in purple light, yellow and green represent wavefunction at $\mathbf{k}_x = \mathbf{0}$, $\mathbf{k}_x = \mathbf{0.5}$ and $\mathbf{k}_x = \mathbf{0.7}$, respectively. Total layer number $L_z = 19$.

645 When a weak Zeeman field, whose strength is comparably small to major parameters
 646 in topological insulator, especially, the bulk gap m_0 , is applied to the topological insulator
 647 film system, its effective Hamiltonian can be obtained by considering only $n = n' = 1$
 648 elements in the projected matrix as a cut-off approximation. The reason why we can do
 649 this lies in the basis wavefunction distribution along \mathbf{z} -direction. As revealed in Fig. 9,
 650 where we have presented $n = 1$ basis wavefunction distribution for the strong topological
 651 insulator with single Dirac cone at Γ , together with $n = 2$ basis wavefunction distribution
 652 as a representative for higher states, the surface state and higher states have little overlap

653 in the low-energy zone (near Dirac cone, in our case the parity-invariant regime [31] around
 654 Γ point, i.e., small \mathbf{k} area), which makes the overlap integral $I_{S/A}^{1,n \geq 2}$ approaches zero in the
 655 regime. This tells that the low-energy behavior of the system under weak Zeeman field
 656 is dominated by only $I_{S/A}^{1,1}$ terms. And when we turn to high-energy part, the effective
 657 Hamiltonian for $\mathbf{n} = \mathbf{1}$ is dominated by the non-vanishing mass term $\mathbf{m}_1(\mathbf{k})$ since Zeeman
 658 integrals are all perturbative quantities in the case. What is more, since $\mathbf{n} \geq \mathbf{2}$ bands are
 659 naturally gapped with minimal gap \mathbf{m}_0 , weak Zeeman field has no prominent influence to
 660 them. Based on the picture above, it suffices that we only consider $\mathbf{n} = \mathbf{1}$ block with $\mathbf{m}_1(\mathbf{k})$
 661 and preserve $I_{S/A}^{1,1}$ as influence (mass-)source at low energy. This procedure is equivalent
 662 to a cut-off approximation. Notice that since low-energy surface states distribute mainly
 663 at two surfaces, Zeeman field at these two zones should play the major role.

664 Now we ignore $\mathbf{n} = \mathbf{1}$ index and write

$$\begin{cases} I_S(\mathbf{k}) &= \langle \Phi_1(\mathbf{k}) | V_Z | \Phi_1(\mathbf{k}) \rangle \\ iI_A(\mathbf{k}) &= \langle \Phi_1(\mathbf{k}) | V_Z | \Phi_3(\mathbf{k}) \rangle \end{cases}, \quad (74)$$

665 which varies with wavevector \mathbf{k} , then by utilizing basis solutions above we have

$$I_S = |C|^2 \sum_{l_z} V_S(l_z) [\lambda_{\perp}^2 |f_+|^2 + t_{\perp}^2 \eta^2 |f_-|^2], \quad (75a)$$

$$iI_A = i|C|^2 \sum_{l_z} V_A(l_z) \lambda_{\perp} t_{\perp} 2\eta \operatorname{Re}[(f_+)^* f_-], \quad (75b)$$

666 respecting (anti-)symmetric part projection of Zeeman field to \mathbf{z} as

$$V_{S/A}(l_z) = \frac{V_z(l_z) \pm V_z(-l_z)}{2}. \quad (76)$$

667 Note that $I_{S/A}$ are real. The effective Hamiltonian for Zeeman term then reads

$$V_{\text{EFF}}(\mathbf{k}) = (I_S(\mathbf{k})\tau_0 - I_A(\mathbf{k})\tau_y)\sigma_z. \quad (77)$$

668 Adding this term to lowest four-band model leads to

$$H_{\text{EFF}} = \lambda_{\parallel}(\sin(k_x a)\sigma_x + \sin(k_y a)\sigma_y) + \mathbf{m}(\mathbf{k})\tau_z\sigma_z + I_S(\mathbf{k})\tau_0\sigma_z - I_A(\mathbf{k})\tau_y\sigma_z, \quad (78)$$

669 where $\mathbf{m}(\mathbf{k}) = \Theta(-\mathbf{m}_0(\mathbf{k}))\mathbf{m}_0(\mathbf{k})$ for thick-enough film, while $I_{S/A}(\mathbf{k})$ are \mathbf{z} -Zeeman-related
 670 integrals dependent on \mathbf{k} . This effective Hamiltonian serves as the starting point analysing
 671 magnetic phases in a topological insulator film within weak Zeeman regime, and we should
 672 confine the Zeeman distribution to mainly stay at top and bottom surfaces to make best
 673 use of them.

674 **Effective mass treatment** Diagonalization of the mass part in the weak Zeeman field case
 675 shows much less complexity than that in Eq. (69), and is accessible analytically. A careful
 676 look on Eq. (78) tells that we can treat all the latter-three terms as mass terms, since by
 677 τ -space diagonalization

$$U_M^{\dagger} [m\tau_z + I_S\tau_0 - I_A\tau_y] U_M = \begin{pmatrix} \tilde{m}_+ & \\ & \tilde{m}_- \end{pmatrix}, \quad (79)$$

678 where the defined unitary matrix reads

$$U_M = \frac{1}{\sqrt{2}} \begin{pmatrix} i\operatorname{sgn}(I_A)\sqrt{1+\frac{m}{M}} & \sqrt{1-\frac{m}{M}} \\ \sqrt{1-\frac{m}{M}} & i\operatorname{sgn}(I_A)\sqrt{1+\frac{m}{M}} \end{pmatrix}, \quad (80)$$

679 with $M(\mathbf{k}) = \sqrt{m^2(\mathbf{k}) + I_A^2(\mathbf{k})}$, we can write $\tilde{H}_{\text{EFF}} = \oplus_{\chi=\pm} \tilde{H}_\chi$ with

$$\tilde{H}_\chi = \lambda_{\parallel}(\sin(k_x a)\sigma_x + \sin(k_y a)\sigma_y) + \tilde{m}_\chi(\mathbf{k})\sigma_z, \quad (81)$$

680 where the effective mass is defined as

$$\tilde{m}_\chi(\mathbf{k}) \equiv I_S(\mathbf{k}) + \chi \sqrt{m^2(\mathbf{k}) + I_A^2(\mathbf{k})}. \quad (82)$$

681 This equation illustrates minimally the mass generation brought by the matrix form Higgs
682 field, which is reduced into merely two components $I_{S/A}(\mathbf{k})$ here. The ultimate effect given
683 by the Zeeman field action to the system is reduced to a correction of the Dirac mass term,
684 which is responsible for the possible non-trivial topology of the system. The treatment
685 here relies on the sign invariance of I_A inside the parity invariant regime, which insures
686 the global gauge consistence for the transformation.

687 Notice that the gap is now determined by

$$\Delta_\chi = 2|\tilde{m}_\chi(\mathbf{0})| = 2|I_S(\mathbf{0}) + \chi|I_A(\mathbf{0})||, \quad (83)$$

688 which is non-zero (gapped) as long as $|I_S(\mathbf{0})| \neq |I_A(\mathbf{0})|$. The χ -Chern number, according
689 to Eq. (44), for each gapped surface state is written as

$$C_\chi = \frac{1}{2}[\text{sgn}(\tilde{m}_\chi(\mathbf{0})) - \text{sgn}(\tilde{m}_\chi(\pi, \pi))], \quad (84)$$

690 which, by utilizing the fact that $\mathbf{m}(\mathbf{0}) = \mathbf{0}$ and Zeeman field is added perturbatively so
691 that $\mathbf{m}(\mathbf{k})$ dominates at (π, π) , we obtain that

$$\begin{aligned} C_\chi &= \frac{1}{2}[\text{sgn}(I_S(\mathbf{0}) + \chi|I_A(\mathbf{0})|) - \chi] \\ &= -\chi \Theta(-|I_A(\mathbf{0})| - \chi I_S(\mathbf{0})). \end{aligned} \quad (85)$$

692 This formula works in the chosen parameter regime $\mathbf{0} < \mathbf{m}_0 < 4t_{\perp}$ within weak Zeeman
693 treatment.

694 4.1.3 Strong Zeeman field

695 For a general strong Zeeman field whose strength is comparably big enough with the
696 system parameter (mainly bulk gap \mathbf{m}_0) or even stronger, with arbitrary configuration
697 along \mathbf{z} direction, both the uniform and the weak criterion fails, and in this case, we
698 usually have to adopt the most general formula by Eq. (67), whose topological property is
699 revealed after a further diagonalization of mass terms given by Eq. (69), which turns the
700 total Hamiltonian again into a direct sum of a series of Dirac fermions shown in Eq. (70).
701 Then based on our discussion in 3, the Hall conductivity of each single Dirac fermion is
702 determined, from which we can analyse the topological property of the system.

703 4.2 Other fields

704 In the subsection, we present more examples of spin and orbital fields other than the
705 \mathbf{z} -Zeeman field discussed above, and the result is listed in Table 1. The signals appeared
706 here only apply in the subsection. The list of results reveal the power of our general
707 procedure, and is enlightening for discovering more topological phases driven by diverse
708 physical origins.

709 For a given field $\mathbf{V}(\mathbf{k}, l_z)\sigma_\mu\tau_\nu$, the transformation follows similarly by organizing the
710 projected elements $\sum_{l_z} \mathbf{V}(\mathbf{k}, l_z) \langle \Phi_m^n(\mathbf{k}, l_z) | \sigma_\mu\tau_\nu | \Phi_{m'}^{n'}(\mathbf{k}, l_z) \rangle$ ($m, m' = 1, 2, 3, 4$; $n, n' = 1, \dots, L_z$)

Table 1: Different fields and their forms under the transformation.

Name of field	Original field expression	Field after transformation	Kernel
Spin-orbital coupling	$\lambda_{\parallel}[\sin(k_x a)\sigma_x \tau_x + \sin(k_y b)\sigma_y \tau_x]$	$\bigoplus_{n=1}^{l_z} \lambda_{\parallel} \tau_0 (\sin(k_x a)\sigma_x + \sin(k_y b)\sigma_y)$	F_{S+}
Zeeman field	$Z_z(l_z)\sigma_z \tau_0$	$(I_S^z(k)\tau_0 - I_A^z(k)\tau_y)\sigma_z$	F_{S+}, F_{A+}
	$Z_x(l_z)\sigma_x \tau_0$	$(I_S^x(k)\tau_x - I_A^x(k)\tau_z)\sigma_x$	F_{S-}, F_{A-}
	$Z_y(l_z)\sigma_y \tau_0$	$(I_S^y(k)\tau_x - I_A^y(k)\tau_z)\sigma_y$	F_{S-}, F_{A-}
Gate-voltage	$G(l_z)\sigma_0 \tau_0$	$(G_S(k)\tau_0 - G_A(k)\tau_y)\sigma_0$	F_{S+}, F_{A+}
Orbital field	$O_y(l_z)\sigma_0 \tau_y$	$(O_A^y(k)\tau_0 - O_S^y(k)\tau_y)\sigma_z$	F_{S+}, F_{A+}
	$O_x(l_z)\sigma_0 \tau_x$	$(O_A^x(k)\tau_z - O_S^x(k)\tau_x)\sigma_0$	$-F_{S-}, -F_{A-}$
	$O_z(l_z)\sigma_0 \tau_z$	$(O_A^z(k)\tau_x - O_S^z(k)\tau_z)\sigma_z$	$F_{S-}, -F_{A-}$

711 aligned with the sequence of the basis. The form of field after transformation will always
 712 be two $\mathbf{L}_z \times \mathbf{L}_z$ matrix fields different by \mathbf{z} -parity symmetry labels, \mathbf{S} counting for symmetric
 713 distribution and \mathbf{A} for the opposite, with each attached with new 4×4 Dirac matrices.

714 To express matrix quantities $\mathbf{I}, \mathbf{G}, \mathbf{O}$ in Table 1, we introduce the momentum-dependent
 715 matrix-form acting functional \mathcal{F}_k over V field that generates projected matrix component
 716 like

$$\mathcal{F}_k^{nn'}[V] = \sum_{l_z} V(\mathbf{k}, l_z) F_V^{nn'}(\mathbf{k}, l_z) = (\mathcal{F}_k^{n'n}[V])^*, \quad (86)$$

717 where the summation kernel $F_V^{nn'}(\mathbf{k}, l_z)$ depends on different Dirac matrix the untrans-
 718 formed field carries. However, in practice, we find that the non-vanishing components in
 719 the transformed field matrix are only generated by four kinds of summation kernels,

$$F_{S+}^{nn'}(\mathbf{k}, l_z) = |C_n C_{n'}| [\lambda_{\perp}^2 (f_+^n)^* f_+^{n'} + t_{\perp}^2 \eta^n \eta^{n'} (f_-^n)^* f_-^{n'}], \quad (87a)$$

$$F_{A+}^{nn'}(\mathbf{k}, l_z) = |C_n C_{n'}| \lambda_{\perp} t_{\perp} [\eta^{n'} (f_+^n)^* f_-^{n'} + \eta^n (f_-^n)^* f_+^{n'}], \quad (87b)$$

$$F_{S-}^{nn'}(\mathbf{k}, l_z) = |C_n C_{n'}| [-\lambda_{\perp}^2 (f_+^n)^* f_+^{n'} + t_{\perp}^2 \eta^n \eta^{n'} (f_-^n)^* f_-^{n'}], \quad (87c)$$

$$F_{A-}^{nn'}(\mathbf{k}, l_z) = |C_n C_{n'}| (-i) \lambda_{\perp} t_{\perp} [\eta^{n'} (f_+^n)^* f_-^{n'} - \eta^n (f_-^n)^* f_+^{n'}], \quad (87d)$$

720 different by symmetry requirement and an inner sign. In the table the symmetry labels
 721 between the field after transformation and the summation kernel are corresponding.

722 The table can be longer once one considers more kinds of Dirac matrices. This proce-
 723 dure above is general, powerful while easy to understand. Despite the easiness of the trans-
 724 formation, the non-trivial difficult part is to endow physical meaning to the attached fields,
 725 both before transformation and after. For instance, the spin-orbital coupling remains its
 726 meaning after the transformation, while being block-diagonal in the Dirac fermion repre-
 727 sentation; the \mathbf{z} -Zeeman field, as discussed above, is transformed into some matrix form
 728 Higgs field, which stands as the effective mass generator.

729 **Spin-orbital duality** Interestingly, we see that the \mathbf{y} -orbital order is transformed to
 730 attach the same Dirac matrices as the transformed \mathbf{z} -Zeeman field, but with symmetry
 731 indices of matrix quantities exchanged. This relation tells that, as long as some topo-
 732 logical phase is discovered with \mathbf{z} -Zeeman field $\mathbf{Z}_z = \mathbf{Z}_{z,S} + \mathbf{Z}_{z,A}$, another phase with the
 733 same topological index can immediately be identified with \mathbf{y} -orbital order satisfying that
 734 $\mathbf{O}_{y,A} = \mathbf{Z}_{z,S}, \mathbf{O}_{y,S} = \mathbf{Z}_{z,A}$. For instance, we show the dual phases formed by σ_z and τ_y orders
 735 in Table 2, the Chern insulator, aka quantum anomalous Hall effect (QAHE), the axion
 736 insulator, the half QAHE and the metallic QAHE as several typical phases in magnetic
 737 topological insulator as we will discuss below. Here one has to notice that for the metallic

Table 2: Duality of typical topological phases induced by spin order σ_z and orbital order τ_y . $\mathbf{t}, \mathbf{b}, \mathbf{m}$ for top, bottom, middle and \mathbf{S}, \mathbf{A} for symmetric, antisymmetric distribution of fields, respectively.

Name of phase	σ_z configuration	τ_y configuration
Chern insulator	$\mathbf{Z}_z^t = \mathbf{Z}_z^b \neq \mathbf{0}$	$\mathbf{O}_y^t = -\mathbf{O}_y^b \neq \mathbf{0}$
Axion insulator	$\mathbf{Z}_z^t = -\mathbf{Z}_z^b \neq \mathbf{0}$	$\mathbf{O}_y^t = \mathbf{O}_y^b \neq \mathbf{0}$
Half QAHE	$\mathbf{Z}_z^t \neq \mathbf{0}, \mathbf{Z}_z^b = \mathbf{0}$	$\mathbf{O}_y^t \neq \mathbf{0}, \mathbf{O}_y^b = \mathbf{0}$
Metallic QAHE	$\mathbf{Z}_{z,S}^m$ strong	$\mathbf{O}_{y,A}^m$ strong

738 QAHE [32], which requires a relatively strong magnetism in the middle of a topological in-
 739 sulator film, the corresponding τ_y orbital order induced metallic QAHE requires a higher
 740 threshold for the antisymmetric field strength $\mathbf{O}_{y,A}^m$, due to the odd function nature which
 741 forces $\mathbf{O}_{y,A}^m(L_z/2) = \mathbf{0}$.

742 Following the effective mass treatment above, we can furthermore construct quantita-
 743 tive model unifying the two orders. There are now totally five mass terms that read

$$\mathbf{M}(\mathbf{k}) = \left[\bigoplus_{n=1}^{L_z} m_n \tau_z + (\mathbf{I}_S^z + \mathbf{O}_A^y) \tau_0 - (\mathbf{I}_A^z + \mathbf{O}_S^y) \tau_y \right] (\mathbf{k}), \quad (88)$$

744 and a similar diagonalization leads to the effective masses

$$\mathbf{M}(\mathbf{k}) \xrightarrow{\text{diagonalization}} \bigoplus_{n=1}^{2L_z} \tilde{m}_n(\mathbf{k}), \quad (89)$$

745 without affecting the spin-orbital coupling field. On the other hand, in the context of
 746 weak interaction, we only preserve $\mathbf{n} = \mathbf{n}' = \mathbf{1}$ components and write down mass terms for
 747 $\mathbf{n} = \mathbf{1}$ block as

$$\left[m \tau_z + (\mathbf{I}_S^z + \mathbf{O}_A^y) \tau_0 - (\mathbf{I}_A^z + \mathbf{O}_S^y) \tau_y \right] (\mathbf{k}), \quad (90)$$

748 with $\mathbf{n} = \mathbf{1}$ label ignored. Here merely a substitution $\mathbf{I}_S \rightarrow \mathbf{I}_S^z + \mathbf{O}_A^y$, $\mathbf{I}_A \rightarrow \mathbf{I}_A^z + \mathbf{O}_S^y$ happened
 749 compare with Eq. (78), and a similar diagonalization leads to two effective masses for the
 750 surface Dirac bands as

$$\tilde{m}_\chi(\mathbf{k}) = (\mathbf{I}_S^z + \mathbf{O}_A^y)(\mathbf{k}) + \chi \sqrt{m^2(\mathbf{k}) + (\mathbf{I}_A^z + \mathbf{O}_S^y)^2(\mathbf{k})}, \quad (91)$$

751 from which the synergistic and competing relations between σ_z and τ_y orders are shown
 752 more explicitly.

753 5 Topological phases with weak field

754 Counting on the mean strength of the magnetic exchange interaction, our exploration
 755 can be further divided into two main branches as weak and strong Zeeman fields. The
 756 division follows simply from the criterion whether the phase can be described within the
 757 $\mathbf{n} = \mathbf{1}$ frame, or equivalently, whether Eq. (78) from weak Zeeman field approximation is
 758 applicable. If it is the case, we identify the phase to lie inside the weak interaction regime,
 759 as we shall discuss here. From here on, all topological insulator means a strong TI with
 760 single Dirac point at Γ .

761 **5.1 Half quantum mirror Hall effect: a non-magnetic film with mirror symmetry**

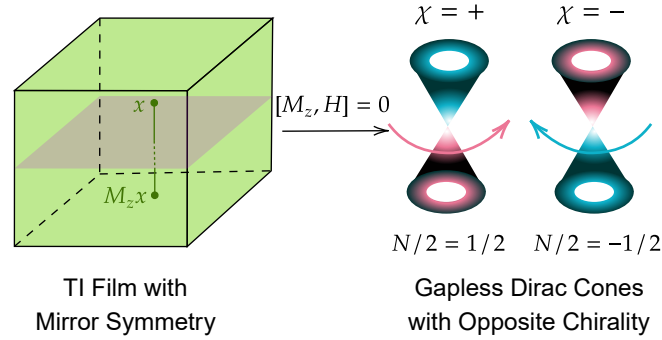


Figure 10: Schematic diagram of the half quantum mirror Hall effect. The lowest four-band of one topological insulator film with mirror symmetry (left) is classified into two gapless Dirac cones with opposite chirality labelled by the eigenvalue of \mathbf{z} -mirror operator.

762 The topological insulator film itself without adding any external ingredients or inter-
 763 actions is already interesting enough and exhibits a novel topological phase [33], namely,
 764 the half quantum Mirror Hall effect shown in Fig. 10, which is deeply related to the
 765 mirror symmetry of the system and reveals measurable parity anomaly physics. A gen-
 766 eral film Hamiltonian reads $\mathcal{H} = \sum_{l_z, l'_z, k} \Psi_{l_z, k}^\dagger H(l_z, l'_z, k) \Psi_{l'_z, k}$, and the out of film plane
 767 mirror symmetry \mathcal{M}_z emerges as a combination of inversion and \mathbf{C}_{2z} rotation that reads
 768 $\mathcal{M}_z \Psi_{l_z, k} \mathcal{M}_z^{-1} = \mathbf{U}_z \Psi_{-l_z, k}$, where \mathbf{U}_z is a unitary matrix. Requiring such symmetry over the
 769 system Hamiltonian leads to the condition $\mathbf{U}_z^\dagger H(l_z, l'_z, k) \mathbf{U}_z = H(-l_z, -l'_z, k)$. It is then
 770 possible to write down the mirror operator under $\{\Psi_{k, l_z}\}$ as $\mathbf{M}_z = \mathbf{C}_{2z} \mathbf{P}$, with \mathbf{U}_z as its off-
 771 diagonal elements, and the Hamiltonian can be projected into decoupled mirror-labelled
 772 parts as

$$\mathbf{H}_\chi = \mathbf{P}_\chi^{M_z} \mathbf{H}, \quad \mathbf{P}_\chi^{M_z} = \frac{1 + i\chi \mathbf{M}_z}{2}, \quad (92)$$

773 with χ labelling the eigenvalue of mirror operator. Each \mathbf{H}_χ is yet again a complete
 774 system whose non-trivial property is revealed by the (zero-temperature, ignored below)
 775 mirror Hall conductivity

$$\sigma_H^\chi = \frac{e^2}{h} \frac{\text{Im}}{\pi} \left[\sum_{E_n^\chi < \mu < E_m^\chi} \int d^2k \frac{\bar{v}_x^{mn, \chi} \bar{v}_y^{nm, \chi}}{(E_n^\chi - E_m^\chi)^2} \right], \quad (93)$$

776 where $\bar{v}_i^{mn, \chi} = \langle \mathbf{n}^\chi | \partial_{k_i} H^\chi | \mathbf{m}^\chi \rangle$ is the expectation value of mirror velocity operator evalu-
 777 ated over eigenstates of the mirror-projected Hamiltonian. Clearly, this is just the usual
 778 Kubo formula [65] evaluated over the projected Hamiltonian \mathbf{H}_χ , and thanks to the im-
 779 posed mirror symmetry, two parts with mirror label $\chi = \pm$ do not communicate with each
 780 other and are totally decoupled.

781 The gapless pair of Dirac fermions in a topological insulator film causes the half quan-
 782 tum mirror Hall effect. Here in the concrete model the off-diagonal elements of mir-
 783 ror operator reads $\mathbf{U}_z = -i\sigma_z \tau_z$, which is projected into τ_z under multi-Dirac fermions
 784 representation (see Appendix B.), indicated by $\chi = \pm$ as its eigenvalue in the effective
 785 Hamiltonian. The gapless $\mathbf{n} = 1$ Dirac fermions in strong topological insulator film read

$$\mathbf{H}_{n=1} = \mathbf{H}_{\text{surf},+} \oplus \mathbf{H}_{\text{surf},=}, \quad (94)$$

786 where each block with mirror label reads

$$H_{\text{surf},\chi} = \lambda_{\parallel}(\sin(k_x \mathbf{a})\sigma_x + \sin(k_y \mathbf{b})\sigma_y) + \chi m(\mathbf{k})\sigma_z, \quad (95)$$

with $m(\mathbf{k}) = \Theta(-m_0(\mathbf{k}))m_0(\mathbf{k})$ identified. To show nature of half quantum mirror Hall

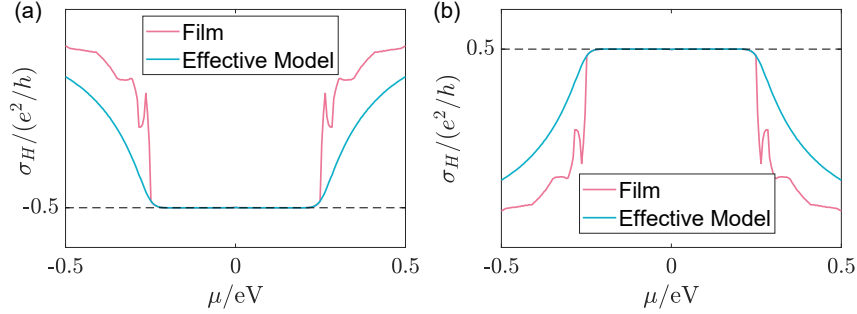


Figure 11: Half-quantized mirror Hall metal: total layer number $L_z = 19$. Results are presented for (a) $\chi = +$, and (b) $\chi = -$. Both results from direct calculation with TI film model and effective model with $\mathbf{h}_{n=1,\chi}$ sub-blocks are shown.

787

788 effect, we calculate the Hall conductivity of H_χ obtained from the mirror-projected TI film
 789 Hamiltonian, and of the split Dirac fermion $H_{\text{surf},\chi}$. The results are shown in Fig. 11, where
 790 the half-quantized transverse conductivity nature is shown for each χ part with inverse
 791 sign, indicating quantum spin Hall like physics [12, 43–45, 84–88], while the topological
 792 origin of the half-quantized mirror Hall conductivity is bounded with the metallic gapless
 793 Dirac fermions [33]. Their massless low-energy parts exist mirror-(anti-)symmetrically
 794 at both top and bottom surfaces of the TI film as a result from the bulk-boundary cor-
 795 respondence of 3D strong topological insulator [17], corresponding to states with mass
 796 $\pm\Theta(-m_0(\mathbf{k}))m_0(\mathbf{k})$ term at $m_0(\mathbf{k}) > 0$. Here, the symmetry statement is traced back
 797 to our basis, which is chosen to distribute along \mathbf{z} either mirror symmetrically or anti-
 798 symmetrically (see Appendix B). As a complete band, the surface Dirac cone does not end
 799 at finite wavevector, but gradually emerges into the bulk with regulated non-zero mass
 800 term represented by $\Theta(-m_0(\mathbf{k}))m_0(\mathbf{k})$ at $m_0(\mathbf{k}) < 0$, and it is this non-vanishing high-
 801 energy part that ultimately gives rise to the half-quantized Hall conductivity, as discussed
 802 in 3, which finally reads by Eq. (42) as $\sigma_H^\chi = -\chi e^2/2h$, when Fermi surface satisfies that
 803 $m_0(\mathbf{k}_F) > 0$.

804 The physically observable effect generated by the phase is embedded in the mirror Hall
 805 conductivity [33], which is defined as

$$\sigma_H^{\text{Mirror}} = \sum_{\chi} \chi \sigma_H^\chi, \quad (96)$$

806 and equals to quantum unit $-e^2/h$ in the case. The quantity reveals that, though, by
 807 opposite Hall conductivity, the charge current by a transverse electrical field vanishes as
 808 $\sigma_H = \sum_{\chi} \sigma_H^\chi = 0$, the ‘mirror’ current does not, similar to that in quantum spin Hall effect.
 809 Nevertheless, a better way looking at the half quantum mirror Hall effect may start from
 810 treating it as an intrinsic ‘spin’ Hall effect in metal, while the effect shows quantization
 811 with its transverse ‘spin’ Hall conductivity that shares a topological origin deeply related
 812 to the parity anomaly, and replacing ‘spin’ with mirror leads to the observation that in
 813 different mirror sectors, the mirror current and the charge current will be either parallel or
 814 anti-parallel with the same quantized magnitude. Such a way of narration also lies at the
 815 lineage of induced dissipationless mirror current and dissipative longitudinal current, as
 816 they are both generated by metallic gapless Dirac fermions. To detect the mirror current,

817 non-local electrical transport signals [89–91] are needed, while to reveal the quantized
 818 nature, one needs to perform a series of measurements to fully separate the dissipationless
 819 and dissipative currents [33], by changing the sample width and notice the scale invariance
 820 of Hall conductance.

821 5.2 Quantum anomalous Hall effect: Chern Insulators

822 The Chern insulator is identified as an insulating phase which hosts quantum Hall ef-
 823 fect [92] with quantized Hall conductance, while without need of applying external mag-
 824 netic field to form Landau levels [93]. The key ingredient lies in the breaking of time
 825 reversal symmetry, which makes the non-vanishing Hall conductivity possible, as studies
 826 extensively in anomalous Hall effect [94]. The quantization nature, on the other hand, is
 827 determined by the Berry phase flux integral over the Brillouin zone, which is an integer
 828 known as the first Chern number [10, 47, 72, 95–97]. An insulator with non-zero Chern
 829 number is known to host gapless chiral edge modes [24] that circulate around the system
 830 dissipationlessly without backscattering [98]. Essentially, the number of the modes is equal
 831 to the Chern invariant, as a physical realization of the index theorem by bulk-boundary
 832 correspondence [13, 25, 26, 99]. It is usually argued that to realize a Chern insulator in a
 833 realistic material, relatively strong spin-orbital coupling together with internal magnetism
 834 are needed [100].

835 With confined geometry, the topological insulator film is predicted [48, 50, 101] to host
 836 the quantum anomalous Hall effect (QAHE) with proper magnetism, either by magnetic
 837 doping approach [49, 102–106] or establishing intrinsic magnetic order [107–109]. In this
 838 sense three typical cases realizing the Chern insulating phase is presented in Fig. 12, with
 839 uniform Zeeman field (to make consistence with discussion here, the Zeeman strength
 840 here is still chosen to be weak, while the uniformly strong strength case is left to be
 841 discussed in the higher Chern number case later on), symmetric top and bottom surface
 842 Zeeman fields configuration and an asymmetric configuration which does not break the
 843 holistic polarization, by which we mean that the symmetric ingredient in the configuration
 844 overwhelms the asymmetric one. The common feature these realizations share is the
 845 parallel polarization of the top and bottom surface-magnetism vertical to the TI film
 846 plane, effectively as the Zeeman field directions that point to both up or down.

847 The verification of the three cases are brought out by numerical calculations with both
 848 TI film and weak Zeeman effective four-band models, as revealed in Fig. 13, Fig. 14 and
 849 Fig. 15, respectively. Besides the bands in (a) that all show Zeeman-gapped feature with
 850 perfect correspondence between two methods, the Hall conductivity in (c) pictures captures
 851 the essence of a Chern insulator with an integer Chern number quantifying the quantized
 852 Hall plateau magnitude. What is more, the calculated $I_{S/A}$ in (b) and Hall conductivity
 853 in (d) for \tilde{H}_χ reveal more about physics behind the phenomenon. Below, based on the
 854 symmetric or asymmetric Zeeman configurations, we further divide the discussion into
 855 two classes.

856 5.2.1 Symmetric magnetic structure

857 In this class,

$$\begin{cases} I_S \neq 0 \\ I_A = 0 \end{cases}, \quad (97)$$

858 and the given first two cases satisfy the condition. In case I and II, the symmetric Zeeman
 859 distribution leads to the vanishing of I_A , and the effective mass, according to Eq. (82), is
 860 written as

$$\tilde{m}_\chi(\mathbf{k}) = I_S(\mathbf{k}) + \chi|m(\mathbf{k})|, \quad I_S > 0, \quad (98)$$

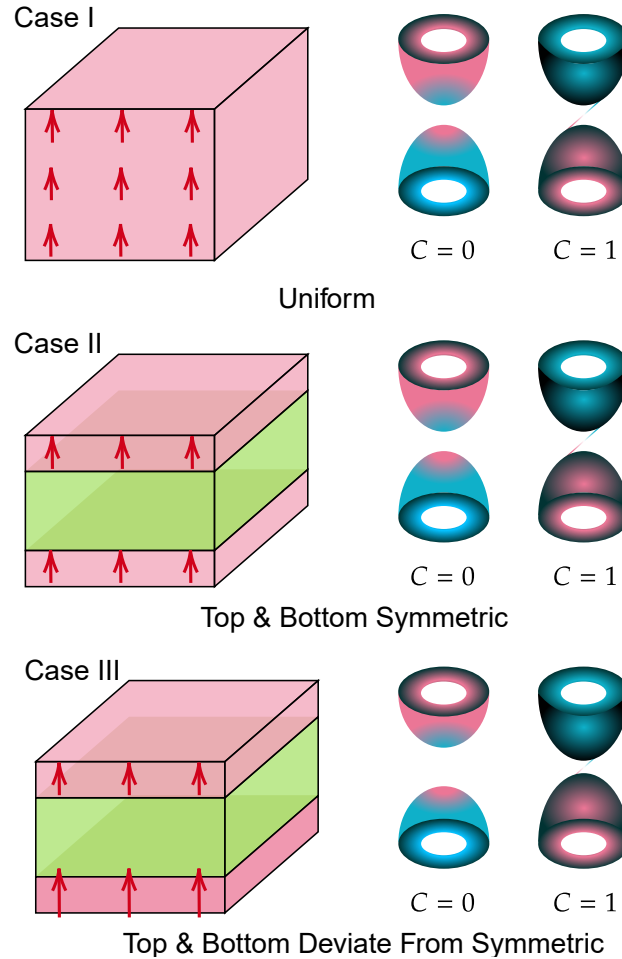


Figure 12: Schematic diagram of three typical Chern insulator cases with pairing gapped lowest Dirac cones responsible for the phase. From top to bottom: Case I: Chern insulator with uniform magnetism whose polarization contains non-vanishing component vertical to the TI film; Case II: Chern insulator with symmetric top and bottom magnetism; Case III: Chern insulator with top and bottom magnetism that deviates from symmetric distribution, but the polarization direction remains the same. In all three cases, two gapped Dirac cones, where the gap comes from the gapped surface states, are present with one trivial cone and one cone with unit Chern number. In the third case we deliberately tune the gap in the diagram to emphasize that it is the cone with a smaller gap that is non-trivial.

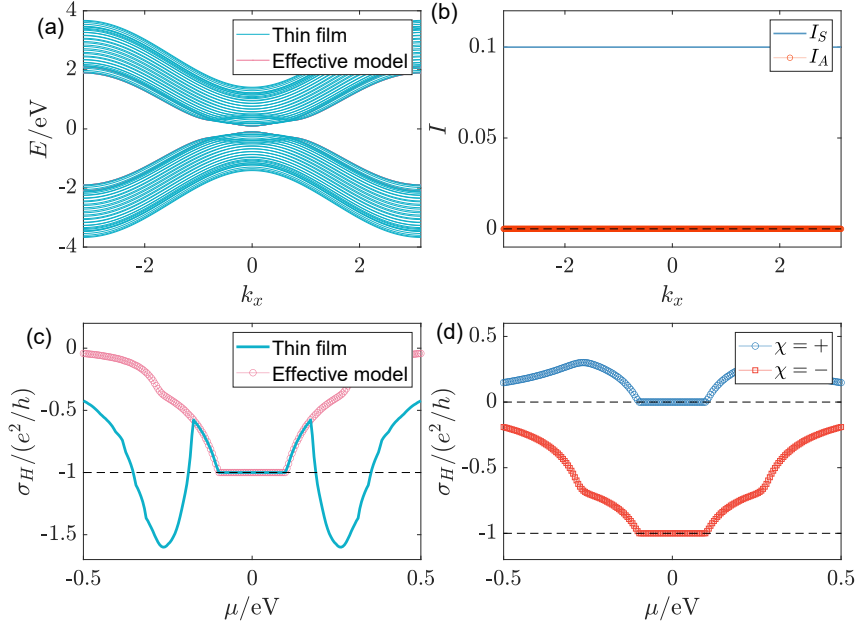


Figure 13: Chern insulator case I: total layer number $L_z = 19$ with uniform Zeeman field $\mathbf{V}_z \equiv \mathbf{0.1} \text{ eV}$. (a) Compare of band structure from TI film model and effective four-band Hamiltonian. (b) Calculated $I_S(\mathbf{k})$ and $I_A(\mathbf{k})$. (c) Calculated Hall conductivity from TI film model and effective four-band Hamiltonian. (d) Hall conductivity for $\chi = \pm$.

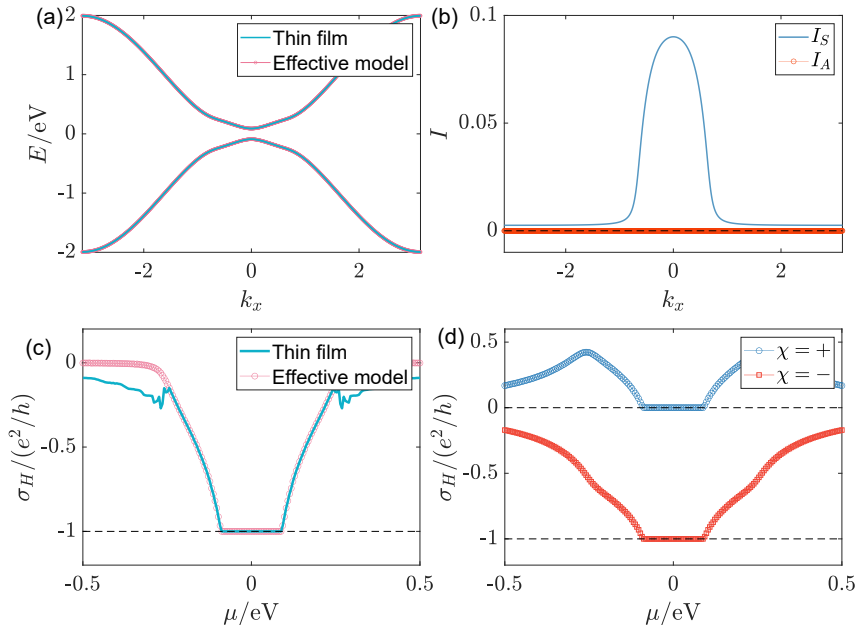


Figure 14: Chern insulator case II: total layer number $L_z = 19$ with top-2-layer Zeeman field $\mathbf{V}_z^t = \mathbf{0.1} \text{ eV}$ and bottom-2-layer field $\mathbf{V}_z^b = \mathbf{0.2} \text{ eV}$. (a) Compare of band structure from the lowest four bands of TI film model and effective four-band Hamiltonian. (b) Calculated $I_S(\mathbf{k})$ and $I_A(\mathbf{k})$. (c) Calculated Hall conductivity from TI film model and effective four-band Hamiltonian. (d) Hall conductivity for $\chi = \pm$.

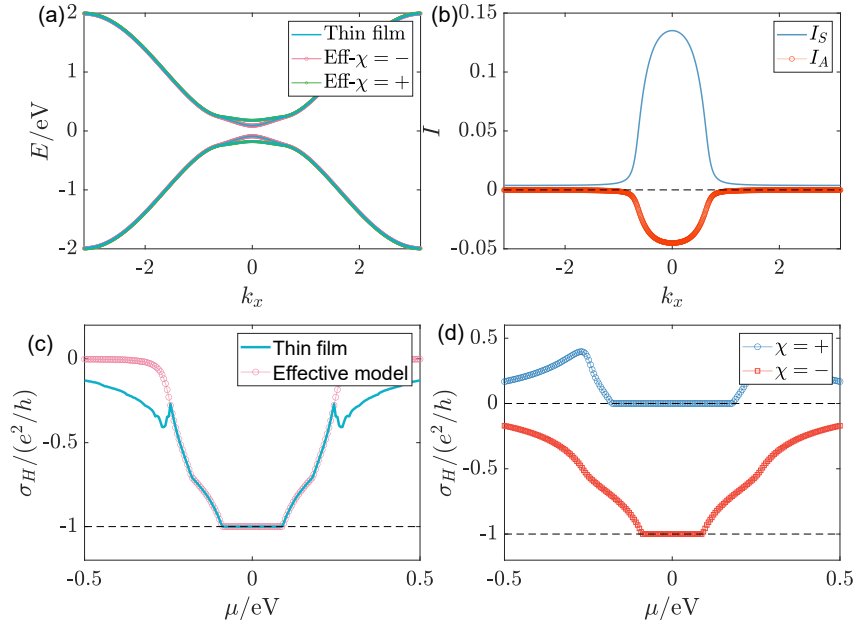


Figure 15: Chern insulator case III: total layer number $L_z = 19$ with symmetric Zeeman field $V_z(\mathbf{l}_z) = 0.1$ eV at top and bottom 2 layers. (a) Compare of band structure from the lowest four bands of TI film model and effective four-band Hamiltonian. (b) Calculated $I_S(\mathbf{k})$ and $I_A(\mathbf{k})$. (c) Calculated Hall conductivity from TI film model and effective four-band Hamiltonian. (d) Hall conductivity for $\chi = \pm$.

861 it is thus clear that under the circumstance, $\chi = -$ branch will contain a mass sign change
 862 from Dirac point $\Gamma = (\mathbf{0}, \mathbf{0})$ to high-energy point $M = (\pi, \pi)$, and is topologically non-
 863 trivial with unit Chern number given by Eq. (84), while $\chi = +$ mass remains positive
 864 and leads to a trivial gapped surface band. And this composes of explanation of the
 865 χ -dependent Hall conductivity for the first two cases.

866 5.2.2 Asymmetric magnetic structure

867 In this case,

$$\begin{cases} I_S \neq 0 \\ I_A \neq 0 \\ |I_S| > |I_A| \end{cases}, \quad (99)$$

868 i.e., an imbalance between top and bottom Zeeman strength appears, while their directions
 869 remain parallel so that the symmetry component overwhelms, as reflected by the case III.
 870 Now we observe that in Fig. 15 (d) $\chi = -$ branch is non-trivial with unit quantized Hall
 871 plateau, and $\chi = +$ branch is trivial with a broader zero-Hall plateau, this means that the
 872 non-trivial $\chi = -$ band has a smaller gap than the $\chi = +$ band, as revealed in Fig. 15 (a).
 873 Lifting this to some principle, we claim that *the surface band with a smaller magnetic gap*
 874 *is non-trivial for Chern insulator film*. To gain insight from the phenomenon, notice that
 875 in this case, both I_S and I_A are non-vanishing, but generally $I_S > |I_A| > 0$ since the Zeeman
 876 configuration is more close to the symmetric case, i.e. $V_S > |V_A| > 0$ near two surfaces in
 877 this case. The above observation leads to

$$\begin{cases} \tilde{m}_\chi(\mathbf{0}) = I_S(\mathbf{0}) + \chi |I_A(\mathbf{0})| > 0 \\ \tilde{m}_\chi(M) = I_S(M) + \chi \sqrt{m^2(M) + I_A^2(M)} \sim \chi |m(M)| \end{cases}, \quad (100)$$

878 and since non-trivial topology requires mass inversion, we conclude that \tilde{m}_- is non-trivial
 879 with unit Chern number while $\chi = +$ is trivial, and clearly the gap $\Delta = 2|\tilde{m}(\mathbf{0})|$ tells that
 880 $\Delta_- < \Delta_+$.

881 Pictures and discussions above complete the case study for the Chern insulator phase
 882 here. Notice that in the typical cases given above, it is always that $\chi = -$ band that has
 883 $-e^2/h$ Hall conductivity while the $\chi = +$ band is trivial with zero Hall contribution, i.e.,
 884 it is a $\mathbf{1} + \mathbf{0}$ combination with the sign of Hall conductivity determined by the polarization
 885 direction of Zeeman field, as we shall illustrate further below.

886 Generalization of the picture above about the Chern insulator phase in TI film to
 887 arbitrary weak Zeeman configuration that varies layer by layer is put here. According
 888 to Eq. (85), the non-trivial condition is satisfied whenever $|I_S| > |I_A|$, i.e., symmetric
 889 Zeeman distribution overwhelms asymmetric configuration, and especially there exists a
 890 χ for which it holds that

$$-\chi I_S(\mathbf{0}) > |I_A(\mathbf{0})|, \quad (101)$$

891 and correspondingly we have

$$C_\chi = -\chi, \quad C_{\bar{\chi}} = \mathbf{0}, \quad (102)$$

892 with $\bar{\chi} = -\chi$ identified. This tells us that while one of the two gapped surface Dirac
 893 fermions becomes topologically non-trivial, carrying non-vanishing Chern index of unit,
 894 the other gapped cone is driven into a topologically trivial band. Then totally the system
 895 owns unit Chern number and quantized Hall conductivity. Meanwhile, by definition of I_S
 896 in Eq. (75a), one deduces that when $I_S(\mathbf{0}) > \mathbf{0}$ which corresponds to a general \mathbf{z} -up V_S
 897 configuration, it is $\chi = -$ that satisfies the condition, vice versa, which allows us to write

$$\begin{cases} C_- = 1, \quad C_+ = 0, & \text{for } I_S(\mathbf{0}) > \mathbf{0} \\ C_+ = -1, \quad C_- = 0, & \text{for } I_S(\mathbf{0}) < \mathbf{0} \end{cases}, \quad (103)$$

898 with $I_S(\mathbf{0})$ contributed mainly contributed from surfaces. There is indeed no threshold
 899 for the Zeeman strength to realize Chern insulator counting the gapless feature of surface
 900 states as long as Eq. (101) is satisfied.

901 We have seen that for the topological insulator based Chern insulator, there are always
 902 one trivially gapped Dirac cone and one with unit Chern number, and a natural question
 903 emerges as which cone is non-trivial? In the symmetric case, gaps of two Dirac fermions are
 904 the same, and we have to rely on χ labelled mirror symmetry together with magnetization
 905 direction to decide which cone is non-trivial. However, for the slightly asymmetric case,
 906 a quick answer to the question can be made: the one with smaller gap is. To see why, we
 907 can consider the gap equation Eq. (83) which can be re-written as

$$\Delta_\chi = 2|(-\chi I_S(\mathbf{0})) - |I_A(\mathbf{0})||, \quad (104)$$

908 we find that for the asymmetric Chern insulator case $-\chi I_S(\mathbf{0}) > |I_A(\mathbf{0})| \geq \mathbf{0}$, and it always
 909 hold that

$$\Delta_\chi < \Delta_{\bar{\chi}}, \quad (105)$$

910 then combined with Eq. (102), we arrive at the conclusion that it is always the cone with
 911 smaller gap which becomes topologically non-trivial carrying unit Chern number, while
 912 the cone with a larger Zeeman gap becomes just trivial.

913 5.2.3 Mirror layer Chern number

914 Notice that there exists a fully symmetric case where $V_A = \mathbf{0}$, and in this special case,
 915 quantity proposed as *mirror layer Chern number* can be defined. Again, the mirror-

916 symmetric Hamiltonian including Zeeman term can be projected into decoupled mirror-
917 labelled parts as

$$H_\chi = P_\chi^{M_z} H, P_\chi^{M_z} = \frac{1 + i\chi M_z}{2}, \quad (92)$$

918 with M_z represented mirror operator, and its off-diagonal elements are recognized to be
919 U_z , which relates quantity at $\pm l_z$.

920 Due to the film geometry, it is natural to introduce the so-called layer Hall conductivity
921 [110–114] by considering layer-dependent eigenstates

$$\sigma_H(l) = \frac{e^2}{h} \frac{\text{Im}}{\pi} \sum_{E_n < \mu < E_m} \sum_{l'} \int d^2k \frac{\bar{v}_x^{nm}(l) \bar{v}_y^{mn}(l')}{(E_n - E_m)^2}, \quad (106)$$

922 where in the usual case, the expectation value of velocity operator is $\bar{v}_i^{mn}(l) = \langle m(l) | \partial_{k_i} H | n(l) \rangle$
923 with only diagonal elements, which, however, fails for the mirror projected Hamiltonian.
924 The key observation lies in the fact that by projection $\partial_{k_i} H_\chi$ contains not only diagonal
925 elements but off-diagonal part, which induces additional non-local transition contribution
926 from exactly mirror symmetrized layers. Work the effect out and one obtains the mirror
927 layer Hall conductivity

$$\sigma_H^\chi(l) = \frac{e^2}{h} \frac{\text{Im}}{\pi} \left[\sum_{E_n^\chi < \mu < E_m^\chi} \sum_{l'} \int d^2k \frac{\bar{v}_{\chi, k_x}^{nm}(l) \bar{v}_{\chi, k_y}^{mn}(l')}{(E_n^\chi - E_m^\chi)^2} \right], \quad (107)$$

928 with

$$\bar{v}_{\chi, k_i}^{nm}(l) = \frac{1}{2} \langle n^\chi(l) | (v_{k_i}(l) | m^\chi(l) \rangle + U_z v_{k_i}(-l) | m^\chi(-l) \rangle), \quad (108)$$

929 where the appeared velocity operator is defined through the original Hamiltonian and is
930 assumed to contain only diagonal element $v_{k_i}(l) = (\partial_{k_i} H)(l)$.

931 Now we turn to our special case. As stated in half quantum mirror Hall effect,
932 the bare Hamiltonian without external field contains mirror symmetry, while the same
933 symmetry constraint imposed on the Zeeman field distribution leads to the restriction
934 that $V_z(l_z) = V_z(-l_z)$, which is equivalent to the requirement that $V_A(l_z) = \mathbf{0}$. Thus,
935 Chern insulator generated by TI film with symmetric Zeeman field owns mirror symme-
936 try, and the corresponding $\sigma_H^\chi(l_z)$ could be carried out, so does its layer-cumulated version
937 $\sigma_{H,c}^\chi(l_z) = \sum_{l=-l_z/2}^{l_z/2} \sigma_H^\chi(l)$, as presented in Fig. 16. The off-diagonal elements of mirror
938 operator reads $U_z = -i\sigma_z \tau_z$ for the TI film.

939 The layer dependent Hall conductivity serves us a new insight to understand the phe-
940 nomenon. Treating the system as a whole, its layer-resolved Hall conductivity, as pre-
941 sented in Fig. 16(c), becomes non-zero mainly near the top and bottom surfaces where
942 time-reversal symmetry is broken explicitly under Zeeman field. And the cumulated Hall
943 conductivity gains approximately half quantum Hall conductivity near two surfaces. On
944 the other hand, as shown in Fig. 16(a), (b), when we split the system by mirror symmetry,
945 the layer-resolved mirror Hall conductivity shows similar top and bottom distribution like
946 the whole system, but with only half the amplitude by mirror splitting, while the Hall
947 conductivity distribution around mirror plane shows opposite-sign peaks inherited from
948 the time-reversal unbroken bulk property like that in the half quantum mirror Hall effect.
949 Once the Hall conductivity contribution is added layer by layer, we immediately see the
950 tri-section configuration: for the non-trivial $C_- = \mathbf{1}$ part, there exists two Hall-plateaus
951 separating the surface and bulk, then following the top-middle-bottom section cut, we
952 see a contribution rather close to $(-1/4) - (-1/2) - (-1/4)$ from each section; and for the
953 trivial $C_+ = \mathbf{0}$ part, the section separation is not that apparent, and we only roughly write
954 $(-c/4) - (c/2) - (-c/4)$ with c approximately one to represent the observed distribution.

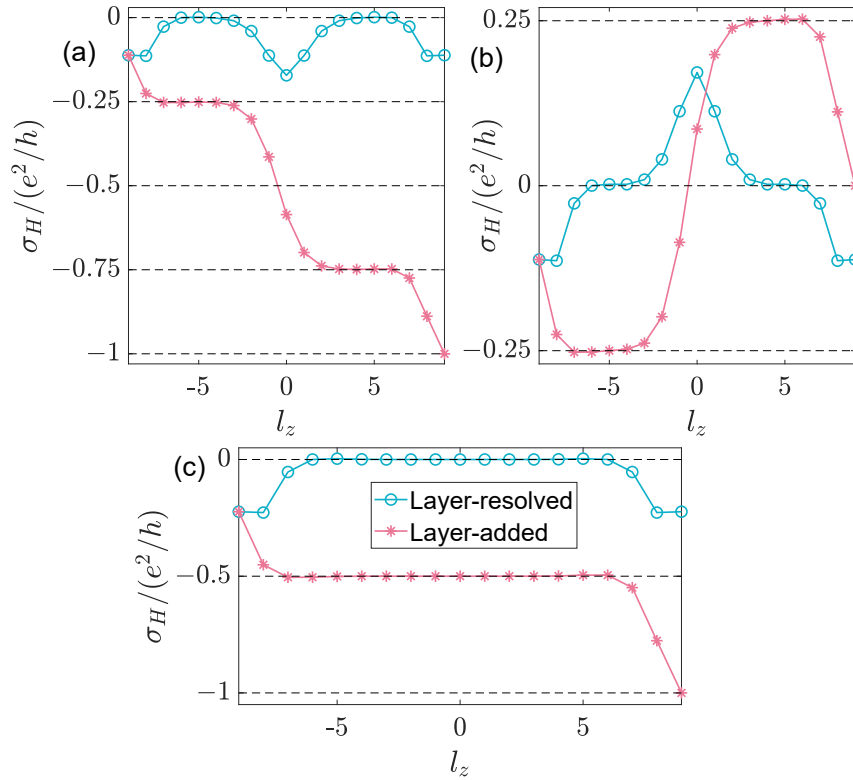


Figure 16: Mirror layer Hall conductivity for topological insulator film with symmetric \mathbf{z} -Zeeman field immersed at top two and bottom **2** layers upon total **19** layers with strength $\mathbf{V}_z = \mathbf{0.1eV}$, and chemical potential is chosen to be $\boldsymbol{\mu} = \mathbf{2.5meV}$, where (a) for $\boldsymbol{\chi} = -$, (b) for $\boldsymbol{\chi} = +$ and (c) for the total result adding two mirror parts together, respectively. Both layer-resolved and layer-added Hall conductivity are presented. To respect the mirror symmetry we put the TI film at origin and layer index becomes $l_z = -\frac{L_z-1}{2}, -\frac{L_z-3}{2}, \dots, \frac{L_z-1}{2}$ with total layer number $L_z = \mathbf{19}$.

955 **5.3 Axion insulator: an antisymmetric magnetic structure**

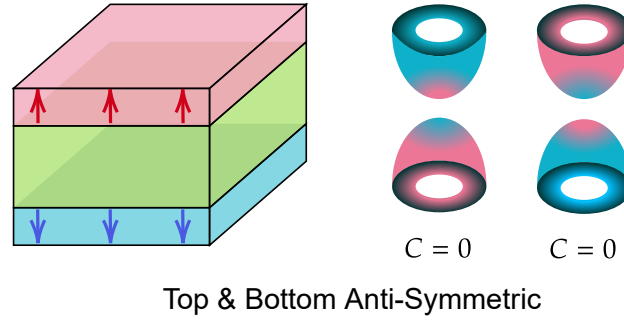


Figure 17: Schematic diagram of the axion insulator. On the left, the magnetic heterostructures of the TI film is presented, with top and bottom surface magnetism containing opposite polarization components vertical to the film. On the right, a pair of trivially gapped Dirac cones are presented, both with zero Chern number. The gap comes from the gapped surface states.

956 Along with the special $(\mathbf{3} + \mathbf{1})$ -D space-time dimension, the Maxwell electrodynamics
 957 is allowed to be decorated with an extra θ term, which generates axion electrodynamic
 958 ics [115, 116] to the space-time dependent θ axion field that couples with the ordinary elec-
 959 tromagnetic field. On a practical level, based on the picture of surface Hall effect [64, 117]
 960 and analogical mathematical structure between Hall current and magnetization current,
 961 people generalize and propose the topological field theory [50], where a θ term is intro-
 962 duced to describe the magnetoelectric effect [110–112, 118–123] in a topological insulator
 963 medium, where the axion field is forced to gain a magnitude of π [124] by symmetry and
 964 topological requirement.

965 Realistically, an anti-ferromagnetic TI represents an example of the axion insulator
 966 [110]. The axion field, proportional to the space-time volume integral field product $\mathbf{E} \cdot \mathbf{B}$
 967 or equivalently the Chern-Simons form [50], is odd under time reversal/inversion. In a
 968 system with such symmetry, the θ field matters only for its absolute value and is defined
 969 only modulo 2π , which is essential for its π magnitude [125]. The anti-ferromagnetic TI
 970 certainly breaks these two symmetries, however, as a 3D system, its θ quantization is
 971 protected by an effective time-reversal symmetry as a combination of time reversal and
 972 translation [126].

973 The magnetic configuration in TI film closest to the proposed axion insulator is the one
 974 in Fig. 17, which shows a zero-Hall plateau and accompanied non-vanishing longitudinal
 975 conductance as an experimental signature [51, 108, 127]. Here then, based on the effective
 976 mass picture, we show that the two Dirac cones with gapped surface states are both trivial,
 977 once high-energy parts are involved. Now the fully antisymmetric magnetic configuration
 978 leads to $\mathbf{I}_S = \mathbf{0}$ for all \mathbf{k} , and the only left Zeeman quantity is \mathbf{I}_A , as shown in Fig. 18(b),
 979 then upon weak Zeeman approximation, the two effective masses become, according to
 980 Eq. (82),

$$\tilde{m}_\chi(\mathbf{k}) = \chi \sqrt{m^2(\mathbf{k}) + I_A^2(\mathbf{k})}, \quad (109)$$

981 which do not show sign reverse in whole Brillouin zone for both χ and are thus trivial.
 982 Numerical result for the Hall conductance related to two masses are shown in Fig. 18 (d),
 983 where the two Hall conductances cancel each other exactly at any chemical potential. Es-
 984 pecially the zero-plateaus, which correspond to chemical potential lying inside the Zeeman
 985 gap, reveal that both bands are trivial with zero Chern number.

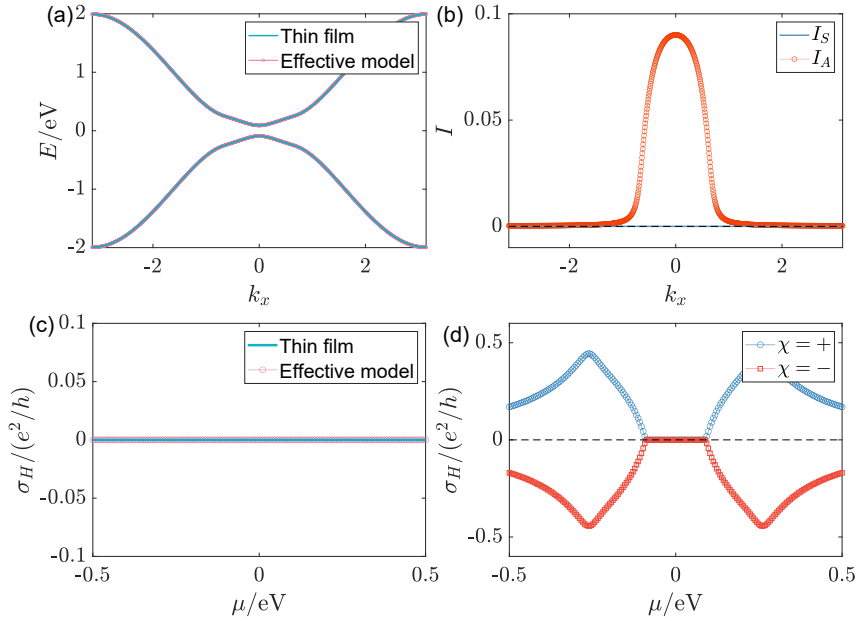


Figure 18: Axion insulator: total layer number $L_z = 19$ with top-2-layer Zeeman field $\mathbf{V}_z^t = \mathbf{0.1}$ eV and bottom-2-layer field $\mathbf{V}_z^b = -\mathbf{0.1}$ eV. (a) Compare of band structure from the lowest four bands of TI film model and effective four-band Hamiltonian. (b) Calculated $I_S(\mathbf{k})$ and $I_A(\mathbf{k})$. (c) Calculated Hall conductance from TI film model and effective four-band Hamiltonian. (d) Hall conductance for $\chi = \pm$.

986 We can also generalize this case. Generally for the axion insulator we need $|I_S(\mathbf{0})| < |I_A(\mathbf{0})|$,
 987 i.e., asymmetric Zeeman distribution overwhelms symmetric configuration at surfaces,
 988 then from Eq. (85) we have

$$\mathbf{C}_+ = \mathbf{C}_- = \mathbf{0}, \quad (110)$$

989 which in fact leads to a trivially insulating phase viewing from the effective 2D model. The
 990 phase is termed as the axion insulator (AI) phase, since the totally asymmetric magnetic
 991 polarization leads to, if one switches a surface-state-representation, a sign difference of
 992 low-energy mass of top and bottom surface states, which gives rise to non-vanishing Berry
 993 curvature at low-energy thus surface Hall contribution, with opposite sign for two surfaces.
 994 However, the Chern number as we have shown for each complete surface band is zero, which
 995 reveals an overall cancellation of transverse transport signals to the linear order, and the
 996 Hall conductivity contributed from the gapped surface states is not protected to be half-
 997 quantized. Furthermore, counting on the zero Chern number nature for each individual
 998 band, the absence of chiral edge state for an \mathbf{x} - \mathbf{y} opened TI film stands firmly, and the
 999 non-vanishing longitudinal conductance measured has to be induced by the side-surface
 1000 states of a topological insulator, and the signal becomes non-zero only when the chemical
 1001 potential is fine-tuned to avoid falling in the finite-size gap $\sim \lambda_{\parallel}^2/L_z^2$ of the side surface.

1002 5.4 MnBi₂Te₄ film: even and odd number of magnetic layers

1003 The first intrinsic antiferromagnetic topological insulator [110], MnBi₂Te₄ (Te-Bi-Te-Mn-
 1004 Te-Bi-Te) [128–130], is composed of septuple layers (SLs), with out-of-plane intralayer
 1005 ferromagnetism and interlayer anti-ferromagnetism, known as the A-type AFM state. It
 1006 is predicted and shown that with odd or even SL layer number, the material will exhibit
 1007 quantum anomalous Hall effect [107, 108, 131–133] or the axion insulating phase [108, 134],

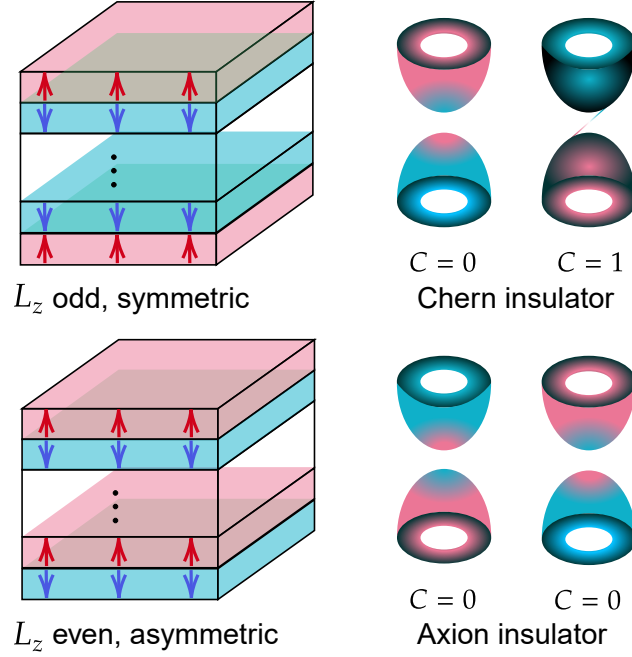


Figure 19: Schematic diagram of the anti-ferromagnetic topological insulator films MnBi_2Te_4 with the magnetic moments along the \mathbf{z} axis. Up: Odd layer number film with net ferromagnetism and symmetric Zeeman distribution, which corresponds a non-trivial Chern insulator; Down: Even layer number film without net ferromagnetism and anti-symmetric Zeeman distribution, which corresponds to the axion insulator with two trivially gapped Dirac cones.

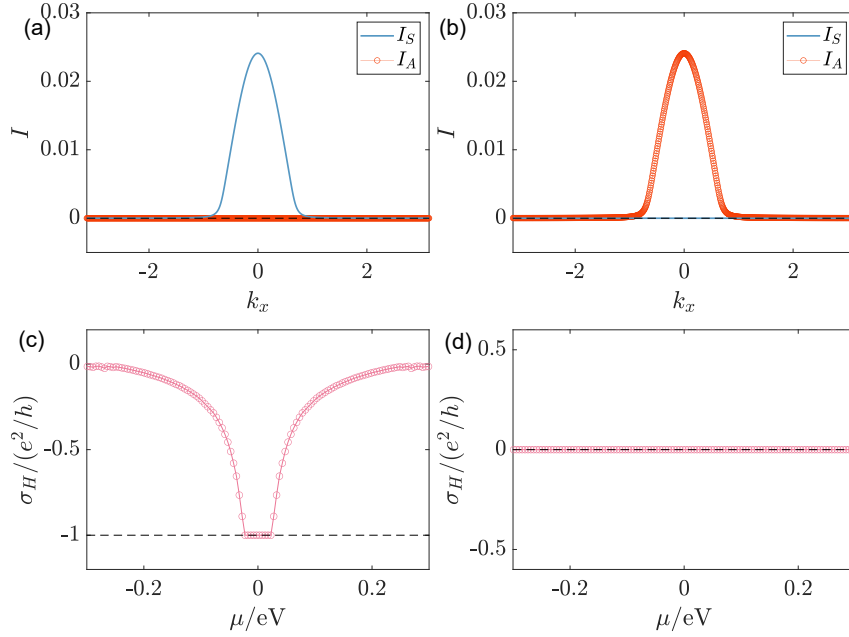


Figure 20: Left (right) pictures are for $L_z = 19(18)$ as an odd (even) one. The Zeeman strength is chosen to be $|\mathbf{V}_z| = 0.1$ eV. (a) (b) Calculated $I_{S/A}(\mathbf{k})$ for the effective model. (c) (d) Calculated Hall conductance from magnetic TI film Hamiltonian.

1008 respectively. Here, based on the lowest four-band model and the discussed Chern and
 1009 axion insulator pictures, we can explain these two phenomenon in a simple and elegant
 1010 way.

1011 The combination of layer-number-odevity determined (anti-)symmetric Zeeman distri-
 1012 bution and the localized nature of surface states leads to two qualitatively distinct physical
 1013 pictures. As revealed in the schematic diagram Fig. 19, when the layer number L_z is odd,
 1014 the Zeeman distribution is symmetric with parallel polarization of the outermost top and
 1015 bottom Zeeman field direction, and vice versa. Based on the symmetry analysis, two cases
 1016 are identified.

1017 5.4.1 Odd layer: Chern insulator

1018 In this case

$$\begin{cases} I_S > 0 \\ I_A = 0 \end{cases}, L_z \bmod 2 = 1, \quad (111)$$

1019 with the maximum value of I_S centralized around Γ as shown in Fig. 20(a), and its sign
 1020 is controlled by the outermost layer Zeeman field direction, given by the fact that the
 1021 low energy states around Γ are localized near two surfaces. I_S almost vanishes for large \mathbf{k}
 1022 since the high energy states emerge into bulk and distribute diffusively, which leads to the
 1023 cancellation of I_S integral counting on the interlayer antiferromagnetism. Discussion above
 1024 classifies the odd SL MnBi_2Te_4 films into Chern insulator phase, as now $\tilde{\mathbf{m}}_\chi = I_S + \chi|\mathbf{m}|$
 1025 following Eq. (98), with $\text{sgn}(\tilde{\mathbf{m}}_\chi(\Gamma)) = \text{sgn}(I_S) > 0$, $\text{sgn}(\tilde{\mathbf{m}}_\chi(M)) = \chi$, and $\tilde{\mathbf{m}}_-$ changes
 1026 signs at Γ and M which gives rise to a unit Chern number, while $\tilde{\mathbf{m}}_+$ is trivially gapped.
 1027 Totally, the odd-layer MnBi_2Te_4 stands as a Chern insulator with unit Hall plateau, as
 1028 revealed in Fig. 20(c), where the relatively narrow quantized Hall plateau for the quantum
 1029 anomalous Hall insulator phase is due to the second-outside-layer Zeeman field which owns
 1030 an inverse polarization direction compared with the outermost field by the interlayer anti-
 1031 ferromagnetic nature, and thus weakens the I_S integral at the Γ point, whose amplitude is
 1032 recognized as the band gap which measures the width of the quantized plateau when the
 1033 chemical potential shifts.

1034 5.4.2 Even layer: axion insulator

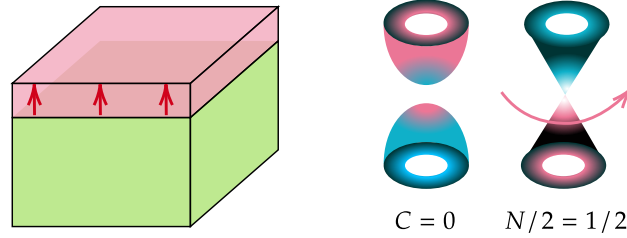
1035 In this case

$$\begin{cases} I_S = 0 \\ I_A > 0 \end{cases}, L_z \bmod 2 = 0, \quad (112)$$

1036 with the maximum value of I_A centralized around Γ as shown in Fig. 20(b), which classifies
 1037 the even SL MnBi_2Te_4 films into axion insulator phase, as now $\tilde{\mathbf{m}}_\chi = \chi\sqrt{m^2 + I_A^2}$ following
 1038 Eq. (109), with $\text{sgn}(\tilde{\mathbf{m}}_\chi(\Gamma)) = \text{sgn}(\tilde{\mathbf{m}}_\chi(M)) = \chi$, and both become trivial since they do
 1039 not change signs. Totally, the even-layer MnBi_2Te_4 shares zero Hall plateau revealed in
 1040 Fig. 20(d).

1041 5.5 Half-quantized anomalous Hall effect: a semi-magnetic film

1042 From a model point of view, there exists a search for a phase characterized by a domain-
 1043 wall separating the axion insulator $|I_A(\mathbf{0})| > |I_S(\mathbf{0})|$ and Chern insulator $|I_A(\mathbf{0})| < |I_S(\mathbf{0})|$,
 1044 and that comes to the celebrated half-quantized anomalous Hall phase [31, 52, 53] with
 1045 condition $|I_S| = |I_A|$ inside the parity-invariant regime. Configurationally, this corresponds
 1046 to a semi-magnetic TI with a Zeeman field applied on only one side, as illustrated in
 1047 Fig. 21. The corresponding numerical results are presented in Fig. 22.



Magnetism at One-Surface Only

Figure 21: Schematic diagram of the half-quantized anomalous Hall effect. In this case only one side of the TI film is immersed with magnetism. The topological property is revealed by one trivially gapped Dirac cone and a gapless Dirac fermion that carries half-quantized Hall conductivity.

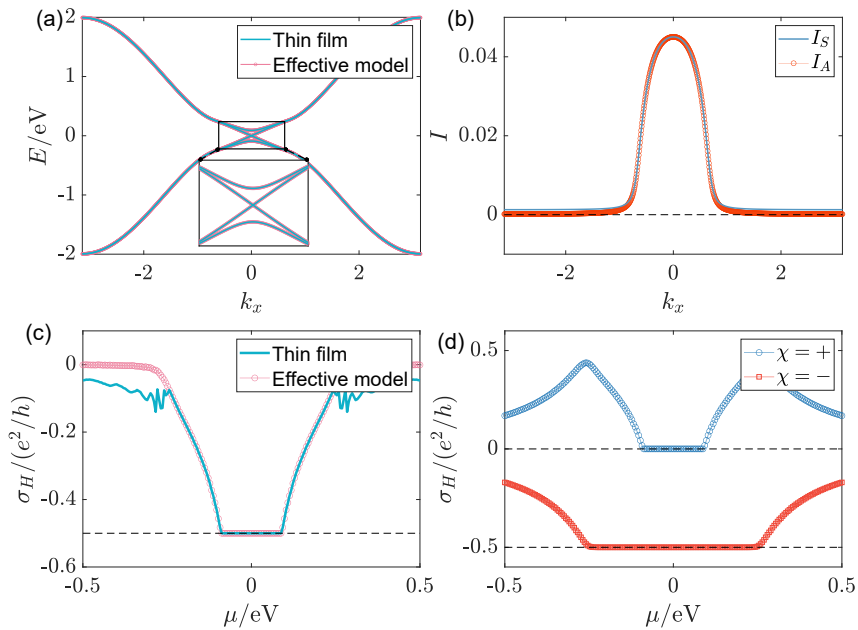


Figure 22: Half-quantized anomalous Hall metal: total layer number $L_z = 19$ with top-2-layer Zeeman field $\mathbf{V}_z^t = \mathbf{0.1}$ eV. (a) Compare of band structure from the lowest four bands of TI film model and effective four-band Hamiltonian. (b) Calculated $I_S(\mathbf{k})$ and $I_A(\mathbf{k})$. (c) Calculated Hall conductance from TI film model and effective four-band Hamiltonian. (d) Hall conductance for $\chi = \pm$.

1048 Another motivation for searching such a phase lies deeply at the lattice realization of
 1049 single Dirac fermion, which serves as a basis for the lattice gauge theory [135, 136]. The
 1050 Nielsen-Ninomiya theorem [29, 30], however, imposes strong constraints on this realization.
 1051 Tremendous approaches have been proposed like the Wilson fermion [4, 34], the SLAC
 1052 fermion [35, 137, 138], the Tan fermion [139, 140], etc. These realizations either break one
 1053 or more conditions required by the fermion-doubling theorem, such as symmetry or locality,
 1054 or evade the physical requirements like existence of first order derivative of wavefunction
 1055 and finite bandwidth on lattice.

1056 In this context, by introducing magnetism to gap out surface states of one Dirac cone
 1057 through magnetism, the remaining gapless Dirac cone, as depicted in Fig. 22(a), essentially
 1058 serves as one lattice realization of single Dirac fermion. As stated, the gapless Dirac cone
 1059 on lattice has to boil one or more conditions required by the fermion-doubling problem, and
 1060 it is the 2D parity symmetry together with the locality that are broken. To avoid doubling
 1061 caused by periodicity of Brillouin zone, the mass term of this gapless Dirac fermion has to
 1062 contain non-vanishing bulk-like high-energy part, as captured by Eq. (11), which breaks the
 1063 parity symmetry explicitly, while the vanishing low energy mass preserves the symmetry.
 1064 Such a low-energy symmetry-preserving while high-energy symmetry-breaking term shares
 1065 similarity with the ‘quantum anomaly’ [47, 66–71] in field theory, specifically the parity
 1066 anomaly in this case. However, the gapless Dirac fermion appeared here manifests itself
 1067 as a regularized complete condensed matter system with explicit symmetry breaking at
 1068 high-energy, which should be distinguished from the spontaneous symmetry breaking case
 1069 under the frame of quantum anomaly. The locality principle is violated by the massless
 1070 to massive transition.

1071 The gapless Dirac fermion, identified as the band with gapless surface states contributes
 1072 a half-quantized Hall conductance. From Fig. 22 (d), $\chi = +$ band is trivial with zero-Hall
 1073 plateau inside the Zeeman gap, i.e., the Zeeman gapped band is trivial, while the $\chi = -$
 1074 band contains a relatively large Hall plateau quantized to $-e^2/2h$, which correspond to
 1075 the Hall conductance contributed the high-energy part of the gapless Dirac band [31]. To
 1076 explain this behavior, it is important to note that we now have $I \equiv I_S = I_A > 0$ around
 1077 the Dirac point revealed in Fig. 22 (b) (valid in the parity invariant regime bounded by
 1078 k_c), and the effective masses become, according to Eq. (82),

$$\tilde{m}_\chi = I(k) + \chi \sqrt{m^2(k) + I^2(k)}, \quad (113)$$

1079 from which we see that $\tilde{m}_+ > 0$ holds for any k and is trivial, while

$$\tilde{m}_- = \begin{cases} 0, & k < k_c \\ I - \sqrt{m^2 + I^2} \sim -|m(k)|, & k > k_c \end{cases}, \quad (114)$$

1080 which is nontrivial and offers us with a half-quantized Hall conductance within the regime
 1081 $k < k_c$, as read from Eq. 40.

1082 To realize this phase generally, we need $|I_S(k)| = |I_A(k)|$ when $k < k_c$. Under the
 1083 situation, one specifies the χ such satisfying that

$$-\chi I_S(k < k_c) = |I_A(k < k_c)|, \quad (115)$$

1084 which gives the gaps according to Eq. (83) that $\Delta_\chi = 0$ while $\Delta_{\bar{\chi}} = 4|I_A(0)|$, i.e., one
 1085 gapless band plus one gapped band. For the gapped band, the Chern number description
 1086 still works and gives

$$C_{\bar{\chi}} = -\bar{\chi} \Theta(-2|I_A(0)|) = 0, \quad (116)$$

1087 while for the gapless band, we can not use Chern number to define its topology in principle,
 1088 since it describes a metallic phase with a non-vanishing Fermi surface. Nevertheless, the
 1089 effective masses now have property

$$\begin{cases} \tilde{m}_\chi(k < k_c) = 0 \\ \tilde{m}_{\bar{\chi}}(k < k_c) = 2\bar{\chi}|I_A(k)| \end{cases}, \quad (117)$$

1090 then combined with the high-energy condition $\tilde{m}_\chi(\pi, \pi) \sim \chi|m(\pi, \pi)|$, one obtains that

$$\begin{cases} \sigma_H^\chi = \frac{\chi}{2} \frac{e^2}{h} \\ \sigma_H^{\bar{\chi}} = 0 \end{cases}, \quad |\mu| < 2|I_A(0)|, \quad (118)$$

1091 in line with Eq. 40, i.e., the gapless Dirac cone provides half-quantized Hall conductance,
 1092 accompanied by a trivial gapped cone. This phenomenon is known as the half-quantized
 1093 anomalous Hall effect [31, 52, 53]. It is important to note that the chemical potential should
 1094 lie within the gapped band to avoid non-quantized contributions from the trivial $\bar{\chi}$ band.
 1095 Additionally, the weak Zeeman field presumption ensures that the Zeeman gap, smaller
 1096 than the bulk gap, does not exceed the energy limit of the parity-invariant regime. The
 1097 metallic nature of the non-trivial gapless Dirac fermion indicates that the system stays
 1098 inside a metallic topological phase. Notice that the non-trivial gapless band requirement
 1099 Eq. (115) gives $\chi = -\text{sgn}(I) = -\text{sgn}(V)$ with $I = I_S(\mathbf{0})$ and $V = V_S^{\text{top}}$, and we can write
 1100 down the asymptotic Hamiltonian for this band as

$$H_{\text{half}} \sim \lambda_{\parallel}(\sin(k_x a)\sigma_x + \sin(k_y b)\sigma_y) + \text{sgn}(V)m(k)\sigma_z, \quad (119)$$

1101 counting for the fact that $m(\mathbf{k}) \leq 0$. This effective Hamiltonian offers with half-quantized
 1102 Hall conductance $-\text{sgn}(V)e^2/2h$, which does not depend on whether the magnetism is
 1103 put at the top or bottom of TI film, but only on its polarization direction. Under an
 1104 external magnetic field, such a single gapless Dirac fermion will step into the quantum
 1105 Hall regime [52, 92] and exhibits quantized Hall conductance whenever an integer number
 1106 of Landau levels become fully filled [141]. Especially, the ‘anomaly’ contribution will
 1107 manifest itself to compensate the half quantization contributed from the lowest Landau
 1108 level, so to keep the integer value of Chern invariant for this gapped Landau level system.

1109 5.6 Phase diagram

1110 To appreciate more on the phases mentioned, especially on the phase transitions among,
 1111 we go back to the effective model and assume that the immersed depth of top and bottom
 1112 Zeeman field, if exists, is relatively longer than the characteristic exponentially decaying
 1113 length of surface states while being much smaller than the film thickness, with uniform
 1114 strength for the top or bottom field. Then we can adopt the substitution

$$I_{S/A} \rightarrow V_{S/A} = V_{S/A}^{\text{top}}. \quad (120)$$

1115 And the effective model reads

$$\begin{cases} \tilde{H}_\chi = \lambda_{\parallel}(\sin(k_x a)\sigma_x + \sin(k_y a)\sigma_y) + \tilde{m}_\chi(k)\sigma_z \\ \tilde{m}_\chi(k) = V_S + \chi \sqrt{m^2(k) + V_A} \\ m(k) = \Theta(-m_0(k))m_0(k) \\ m_0(k) = m_0 - 4t_{\parallel} \left(\sin^2 \frac{k_x a}{2} + \sin^2 \frac{k_y b}{2} \right) \end{cases}, \quad (121)$$

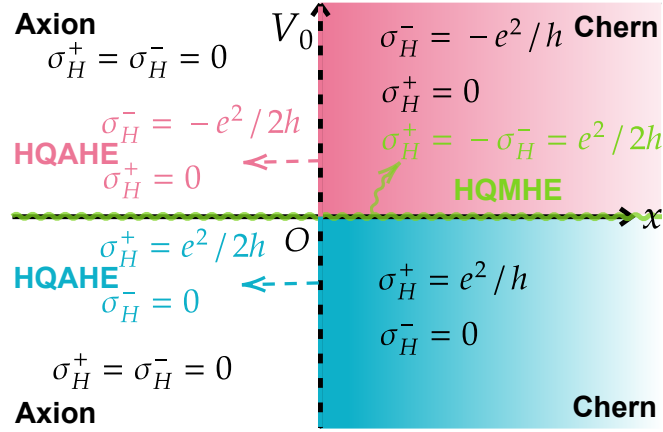


Figure 23: Phase diagram topological phases with weak field. Four distinct phases have been labelled as Chern insulator phase in the first and fourth quadrants differed by sign of Hall conductance, Axion insulator phase in the second and third quadrants, the half quantum mirror Hall effect (HQMHE) along the \mathbf{x} -axis (indicated by the green wave line), and the half-quantized anomalous Hall effect (HQAHE) along \mathbf{V}_0^+ and \mathbf{V}_0^- rays (indicated by red or blue dot lines) differed by sign of Hall conductance. The effectiveness of the phase diagram should be confirmed for chemical potential lying in the parity invariant regime or (smaller) Zeeman gap of surface states, and the Zeeman strength should be constrained to be relatively weak compared with the bulk gap, while playing its role mainly at top and bottom surfaces under the discussed frame.

1116 from which one reads the Hall conductance as (in the Zeeman gap or the parity invariant
1117 regime)

$$\sigma_H^\chi = \frac{e^2}{h} \frac{1}{2} [\chi - \text{sgn}(V_S + \chi|V_A|)]. \quad (122)$$

1118 Now let us introduce the top Zeeman strength $\mathbf{V}_z^{\text{top}} = \mathbf{V}_0$, and the bottom Zeeman strength
1119 $\mathbf{V}_z^{\text{bottom}} = \mathbf{x} \mathbf{V}_0$ described by the collaboration between $\mathbf{V}_z^{\text{top}}$ and a phenomenological pa-
1120 rameter \mathbf{x} characterizing their relative strength. Then accordingly we have

$$\begin{cases} V_S = V_0 \frac{1+x}{2} \\ V_A = V_0 \frac{1-x}{2} \end{cases}, \quad (123)$$

1121 which gives further the Hall conductance

$$\sigma_H^\chi = \frac{e^2}{h} \frac{1}{2} \left[\chi - \text{sgn}(V_0) \text{sgn} \left(\frac{1+x}{2} + \chi \text{sgn}(V_0) \left| \frac{1-x}{2} \right| \right) \right], \quad (124)$$

1122 whose dependence on parameters $(\mathbf{x}, \mathbf{V}_0)$ are presented in Fig. 23 as a phase diagram
1123 emphasizing the role the relative strength \mathbf{x} played here. Notice that we have defined
1124 $\text{sgn}(\mathbf{0}) = \mathbf{0}$ here, corresponding to realistic physical phenomenon when $\mathbf{V}_0 = \mathbf{0}$. From the
1125 diagram, except for $\mathbf{V}_0 = \mathbf{0}$ line, which represents a pure topological insulator film with
1126 half quantum mirror Hall effect, it is always $\mathbf{x} \geq \mathbf{0}$ side that gives rise to phases with
1127 non-vanishing Hall conductance, belonging to either Chern insulator or half-quantized
1128 anomalous Hall metal phase, while the $\mathbf{x} < \mathbf{0}$ side termed as axion insulator phase always
1129 contain two trivially gapped Dirac cones/fermions.

1130 Focusing on the phase transition, we observe that a phase characterized by an anoma-
 1131 lous half-quantized index always emerges upon the integer index phase transition. This
 1132 phenomenon echoes transitions observed in integer quantum Hall systems [102, 142], where
 1133 the renormalization group flow diagram exhibits a generic fixed point with half-quantized
 1134 Hall conductance and finite longitudinal conductance, suggesting a phase transition in 2D
 1135 from a field theoretical point of view. However, the physics here should differ, as the
 1136 robustness of the gapless surface state is protected by the bulk and corresponding surface
 1137 time-reversal symmetry as an intrinsic feature of 3D strong topological insulators [17]. Put
 1138 the statement differently, the additional dimension in our system exhibits robust topolog-
 1139 ical/geometric effects, making it plausible that phases characterized by half-integers here
 1140 are more likely to be symmetry-protected metallic topological phases, while this protection
 1141 only occurs in a finite regime over the whole Brillouin zone. Especially, the half QAHE
 1142 here is protected by a parity invariant regime, and is different from a critical quantum
 1143 Hall transition phase without protection from any non-conformal symmetries.

1144 In the phase diagram we draw, the line of half quantum mirror Hall effect is crossed
 1145 changing between two Chern insulator phases characterized by opposite Chern number,
 1146 since such a phase transition relies on changing of Zeeman polarization direction, thus
 1147 crossing $\mathbf{V}_0 = \mathbf{0}$ where half quantum mirror Hall effect happens. A similar thing happens
 1148 for the transition between axion insulator phases differed by Zeeman direction. On the
 1149 other hand, lines representing half QAHE are crossed when stepping between the Chern
 1150 insulator and axion insulator phases, with the sign of Hall conductance determined by
 1151 Zeeman direction.

1152 6 Topological phases with strong field

1153 A more extensive and complex regime exists beyond the weak Zeeman field approxima-
 1154 tion, and the criterion tells that the topological phase appearing here can not be simply
 1155 described under $\mathbf{n} = \mathbf{1}$ frame. In this scenario, we step into the strong interaction regime,
 1156 where the appearance of $\mathbf{n} \geq \mathbf{2}$ cones is unavoidable. Surprisingly, the inter-Dirac-cone
 1157 interaction can sometimes play the ultimate role deciding the topological property of the
 1158 system. It is in such situations that our effective mass picture from Eq. (68) and Eq. (69)
 1159 serves as the ultimate criterion for the topological property in the system.

1160 6.1 Metallic quantized anomalous Hall effect: a film with a magnetic sandwich 1161 structure

1162 One another novel metallic topological phase bearing a pair of gapless Dirac fermions
 1163 has been recently proposed [32], which shows a quantized Hall conductivity of unit that
 1164 originates from two metallic bands, each with one-half quantum. To further enhance our
 1165 understanding of magnetic topological phases, the key findings related to this phase are
 1166 summarized below.

1167 The schematic diagram is shown in Fig. 24. We set total layer number $L_z = 22$ which
 1168 is even, and the \mathbf{z} -symmetric site positions read

$$1169 \quad l_z = \pm \frac{1}{2}, \dots, \pm \frac{L_z - 1}{2}. \quad (125)$$

1170 Accordingly, \mathbf{z} -symmetric Zeeman field in magnetically doped layers at the middle of the
 1171 TI film is set as

$$1172 \quad V_z(l_z) = \begin{cases} \alpha t_\perp, & l_z = \pm 1/2, \dots, \pm(m_z - 1)/2 \\ \mathbf{0}, & \text{otherwise} \end{cases}, \quad (126)$$

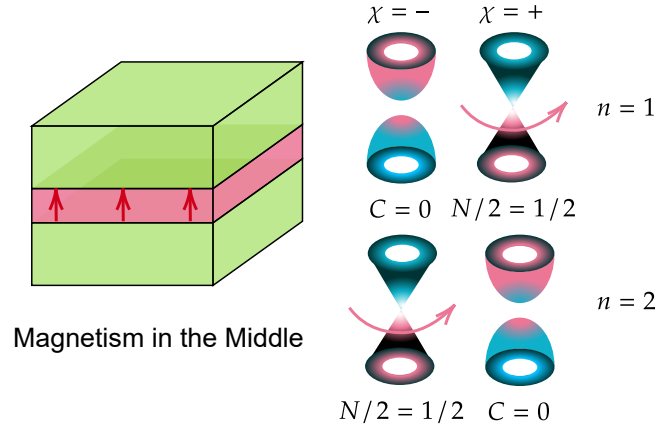


Figure 24: Schematic diagram of the metallic quantized anomalous Hall effect. In the case a relatively strong magnetic interaction exists in the middle of the film. The topological property of the system is reflected by a pair of gapless Dirac cones with the same high energy mass sign, each carrying half quantized Hall conductivity.

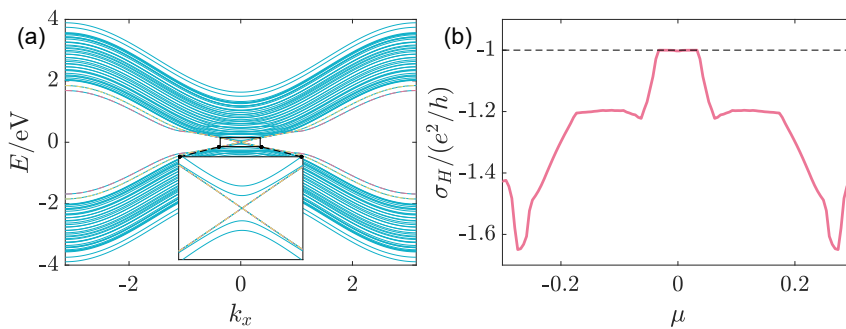


Figure 25: (a) The band structure near the Γ point with $\mathbf{k}_y = \mathbf{0}$ with the presence of magnetic doping ($\alpha = 0.9$). The gapless dispersions for the surface states are doubly degenerated, as shown by the red and yellow lines. (b) Corresponding Hall conductivity as a function of the chemical potential μ at $\alpha = 0.9$. The thickness $L_z = 22$ and the magnetic layers $m_z = 6$.

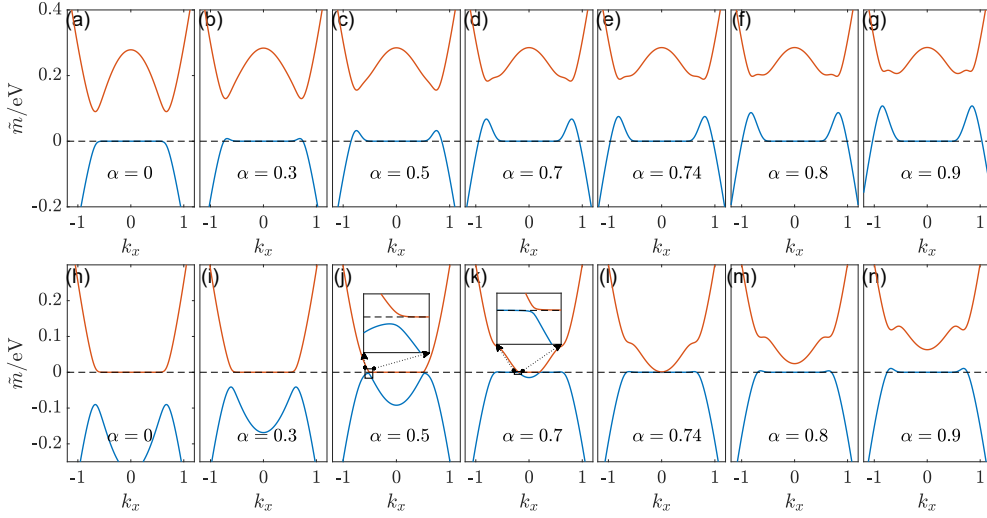


Figure 26: The evolution of the effective mass $\tilde{m}_{n,\chi}(\mathbf{k}_x, \mathbf{k}_y = \mathbf{0})$ ($n = 1, 2$). (a)~(g) and (h)~(n) show lowest-two **effective masses** varying with changing Zeeman field strength α belonging to set $[0, 0.3, 0.5, 0.7, 0.74, 0.8, 0.9]$ for $\chi = +$ and $\chi = -$, respectively. (a) (g) (h) (n) have already been shown as Fig. 3 in the main text but with a finer structure here. Adapted from [32].

1171 with magnetic layer number $m_z = 6$. By \mathbf{z} -symmetric $V_S(\mathbf{l}_z) = V_z(\mathbf{l}_z)$, $V_A(\mathbf{l}_z) = \mathbf{0}$, the
 1172 projection only contains \mathbf{I}_S term proportional to α . Then we bring α to the front explicitly
 1173 as

$$\mathbf{I}_S(\alpha, \mathbf{k})\tau_0\sigma_z \mapsto \alpha\mathbf{I}_S(\mathbf{k})\tau_0\sigma_z, \quad (127)$$

1174 with $\mathbf{I}_S(\alpha = 1, \mathbf{k}) \mapsto \mathbf{I}_S(\mathbf{k})$ is a re-definition.

1175 The metallic feature and quantized Hall conductivity nature are revealed in Fig. 25.
 1176 The band structure of the film is shown in the presence of strong enough magnetism
 1177 ($\alpha = 0.9$), with a pair of massless Dirac fermions. The pairing nature is reflected by the
 1178 double degeneracy of band dispersion near the Γ point, as labelled by the red and yellow
 1179 lines. The unbroken surface states picture is possible due to the localized nature of the
 1180 surface states inside the bulk-gap, which is not affected by the far-away magnetism in
 1181 the middle of the film. Meanwhile, a quantized Hall conductivity is observed, when the
 1182 chemical potential lies inside both the bulk and magnetic gap. And as we shall see later,
 1183 essentially the quantization comes from the two gapless Dirac fermions, each sharing a
 1184 half-quantized Hall conductivity with the same sign, based on which we further identify
 1185 that the effect is not only superficially metallic, but originates from such metallic bands.
 1186 And it is in this circumstance that we term this new phase as the ‘metallic quantized
 1187 anomalous Hall effect’ (metallic QAHE), indicating that it differs from the conventional
 1188 QAHE, aka the Chern insulator in an insulating phase.

1189 Attributed to the mass exchange mechanism over the effective mass picture presented
 1190 in Section 4, such a topological phase transition with the increasing of α as Zeeman
 1191 strength in the middle can be explained. Absorbing the α -dependent Zeeman term into
 1192 the one-dimensional Hamiltonian separated from the TI film leads to an α -dependent 1-D
 1193 Hamiltonian $\mathbf{H}_{1d}(\alpha)$, with $\mathbf{H}_{1d}(\alpha = \mathbf{0})$ coming back to the 1-D Hamiltonian extracted
 1194 from TI film and solved exactly before. Projecting $\mathbf{H}_{1d}(\alpha)$ over solutions of $\mathbf{H}_{1d}(\mathbf{0})$ leads
 1195 to $(\bigoplus_{n=1}^{L_z} m_n \tau_z + \alpha \mathbf{I}_S(\mathbf{k}) \tau_0) \sigma_z$, and further diagonalizing this provides a bijection which
 1196 maps the projected Hamiltonian form into the mass term $\bigoplus_{n=1, \chi=\pm}^{L_z} \tilde{m}_{n,\chi}(\mathbf{k}, \alpha) \sigma_z$. Notice
 1197 that both σ_z and τ_z here are good quantum numbers, as spin and mirror indices ($\chi = \pm$),

1198 respectively. Confining to the subspace with $\sigma_z = +$, we could then track the evolution
 1199 and interaction of the mass terms $\tilde{m}_{n,\chi}$ between $n = 1$ and $n = 2$ blocks with increasing α
 1200 for given χ . As shown in Fig. 26, $\tilde{m}_{n,+}(n = 1, 2)$ maintain their shapes increasing α , while
 1201 $\tilde{m}_{n,-}(n = 1, 2)$ have effectively exchanged their high-energy parts through the low-energy
 1202 mass exchange, which leads to the high-energy mass sign change of the gapless Dirac cone,
 1203 and alters its Hall conductivity from $e^2/2h$ to $-e^2/2h$, when Fermi surface lies inside the
 1204 parity invariant regime. Then combined with the unaltered $-e^2/2h$ from $\tilde{m}_{1,+}$, totally
 1205 a topological phase transition happens, driving the system from zero Hall conductivity
 1206 to quantized Hall conductivity, with Hall contribution coming from two metallic bands,
 1207 which makes the system a metallic topological phase. We can identify

$$\alpha_c \approx 0.74 \quad (128)$$

1208 in this case to indicate $0 \rightarrow -1$ plateau transition. Notice that although we have explicitly
 1209 exploited the \mathbf{z} -mirror symmetry to separate our effective masses into two groups, this
 1210 symmetry consideration is not necessary here and the metallic QAHE is not protected by
 1211 the symmetry. For example, from Eq. (68), Eq. (69) we see clearly that a general Zeeman
 1212 field configuration can still generates $2L_z$ independent Dirac masses, and if we place a
 1213 strong enough Zeeman field in the middle of the film deviating from the symmetric case,
 1214 still we can see the effect with unit Hall plateau.

1215 The key difference between our metallic QAHE and the conventional QAHE or equiv-
 1216 alently the Chern insulator lies in the unconventional bulk boundary correspondence. As
 1217 discussed in [31], the half quantized Hall conductivity bears no chiral edge states, while its
 1218 corresponding surface physics lies in the existence of the chiral current, which is indeed a
 1219 bulk states contribution and decays algebraically along the metallic surface, starting from
 1220 the middle magnetic zone where time reversal symmetry is broken most severely.

1221 6.1.1 A qualitatively model with $n = 1, 2$

1222 A qualitative understanding of the phenomenon within a cut-off approximation based on
 1223 the $n = 1, 2$ blocks can be deduced. In the mass exchange picture above, we have used the
 1224 fully diagonalized $\tilde{m}_{1,2}$ to illustrate the physics behind, while the picture with only $n = 1$
 1225 involved based on the weak Zeeman field approximation breaks down. This is essentially
 1226 because, the weak field approximation heavily relies on effect the magnetism has upon the
 1227 surface states, which is not the case here since the magnetism in the middle will not directly
 1228 affect the surface states, and were there to be any physics effects, they must be conducted
 1229 through the bulk states, whose wavefunction has maximal overlap with the magnetic areas.
 1230 Here, the metallic QAHE is just the first non-trivial case of such kind, where the inter- n
 1231 blocks interaction conducted through magnetism is deterministic, and luckily, we have
 1232 found a way to directly observe the overall effect by a second diagonalization, yielding the
 1233 effective masses \tilde{m}_n . While the process and the results are straightforward and conclusive,
 1234 it will be more satisfying if a simplified model exists and grasps the core of physics even
 1235 qualitatively. Interestingly, a model incorporating the $n = 1, 2$ blocks plays a crucial role
 1236 in achieving this.

1237 For simplicity, we consider the symmetric Zeeman field in the middle, and by preserving
 1238 $n = 1, 2$, the mass terms read

$$M(\alpha) = \begin{pmatrix} m_1 & \\ & m_2 \end{pmatrix} \tau_z + \alpha \begin{pmatrix} I_S^{11} & I_S^{12} \\ I_S^{21} & I_S^{22} \end{pmatrix} \tau_0, \quad (129)$$

1239 with \mathbf{k} -dependence in m_n and I_S terms. The Hamiltonian for $n = 1, 2$ reads

$$H^{n=1,2}(\mathbf{k}) = \lambda_{\parallel} \rho_0 \tau_0 (\sin(k_x a) \sigma_x + \sin(k_y b) \sigma_y) + M \sigma_z, \quad (130)$$

1240 with ρ another pseudo-spin degrees of freedom for two blocks.

1241 Following the effective mass treatment, we further block-diagonalize $H^{1,2}$ into 2×2 sub-
1242 blocks. Notice that again the projected mirror operator τ_z in M serves as a good quantum
1243 number due to the chosen symmetric Zeeman distribution, then a split $M = \oplus_{\chi} M_{\chi} (\chi = \pm)$
1244 can be made, so does that for the Hamiltonian $H^{1,2} = \oplus_{\chi} H_{\chi}^{1,2}$, where

$$H_{\chi}^{1,2} = \lambda_{\parallel} \rho_0 (\sin(k_x a) \sigma_x + \sin(k_y b) \sigma_y) + \alpha \operatorname{Re}(I_S^{12})(k) \rho_x \sigma_z - \alpha \operatorname{Im}(I_S^{12})(k) \rho_y \sigma_z \\ + E_{\pm}(k) \rho_0 \sigma_z + \Delta_{\pm}(k) \rho_z \sigma_z, \quad (131)$$

1245 with

$$\begin{cases} E_{\chi} = [\chi(m_1 + m_2) + \alpha(I_S^{11} + I_S^{22})]/2 \\ \Delta_{\chi} = [\chi(m_1 - m_2) + \alpha(I_S^{11} - I_S^{22})]/2 \end{cases}. \quad (132)$$

1246 Clearly, diagonalization in ρ -space is accessible without altering the linear part, which
1247 leads to

$$\tilde{H}_{\chi\zeta}^{1,2} = \lambda_{\parallel} (\sin(k_x a) \sigma_x + \sin(k_y b) \sigma_y) + \tilde{m}_{\chi,\zeta} \sigma_z, \quad (133)$$

1248 where

$$\tilde{m}_{\chi,\zeta} = (E_{\chi}(k) + \zeta \Lambda_{\chi}(k)) \sigma_z, \quad \chi, \zeta = \pm, \quad (134)$$

1249 with $\Lambda_{\chi} = \sqrt{\Delta_{\chi}^2 + \alpha^2 |I_S^{12}|^2}$ defined. This is reached by a unitary transformation $U_{\chi} = U_2^{\chi} U_1^{\chi}$
1250 for each χ , where $U_2^{\chi} = e^{i\rho_x \theta_2^{\chi}}$, $U_1^{\chi} = e^{i\rho_y \theta_1^{\chi}}$, with definitions $\tan 2\theta_1^{\chi} = \alpha \operatorname{Re}(I_S^{12})/\Delta_{\chi}$,
1251 $\tan 2\theta_2^{\chi} = \alpha \operatorname{Im}(I_S^{12})/\delta_{\chi}$, $\delta_{\chi} = \sqrt{\alpha^2 \operatorname{Re}(I_S^{12})^2 + \Delta_{\chi}^2}$.

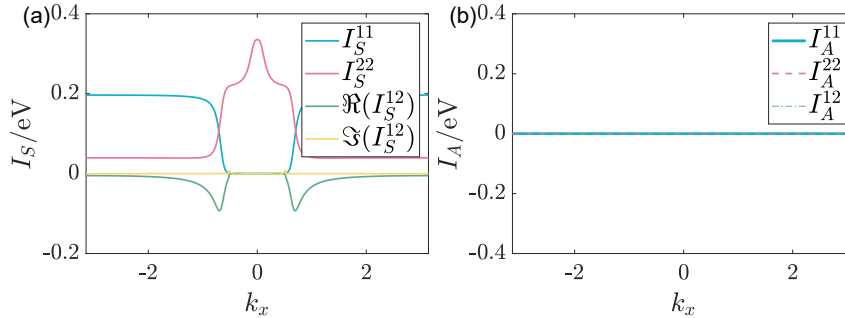


Figure 27: $I_{S/A}^{11}, I_{S/A}^{22}$ and $I_{S/A}^{12}$ calculated with total layer number $L_z = 22$ and middle Zeeman layer number $m_z = 6$. Re-plot from [32].

1252 Now we choose case $\alpha > 0$ so that $\alpha I_S^{nn} > 0$ to illustrate the physics. Topological phase
1253 transition happens when $\alpha I_S^{22} > m_2(0) > 0$ (for $m_2(0) > 0$ see Fig. 4) with the help of
1254 I_S^{12} . In the case now, we identify the Hall conductivity for each sub-block as

$$\sigma_H^{\chi\zeta} = \frac{e^2}{2h} \left[\operatorname{sgn}(\tilde{m}_{\chi,\zeta}(M)) - \operatorname{sgn}(\tilde{m}_{\chi,\zeta}(k_F^{\chi,\zeta})) \right], \quad (135)$$

1255 with $\tilde{m}_{\chi,\zeta}(k_F^{\chi,\zeta})$ recognized as $\tilde{m}_{\chi,\zeta}$ at Fermi surface of the band, and for an insulating
1256 band with Fermi level inside the gap, it is $\tilde{m}_{\chi,\zeta}(0)$. For unification and simplicity, we will
1257 always assume Fermi level to lie inside insulating gap and the parity invariant regime of
1258 a gapless band near Γ point so to always recognize $k_F = 0$, and those worrying about the
1259 singular gapless Dirac point for the metallic case can always take the unambiguous second

1260 limit in Section 3.5. Then by treating

$$\begin{cases} m_1(0) = 0, m_2(0) > 0 \\ -m_1(M) \approx m_2(M) \gg \alpha |I_S(M)| > 0 \\ I_S^{11}(0) = I_S^{12}(0) = 0, I_S^{22}(0) > 0 \\ I_A = 0 \end{cases},$$

1261 where quantities $I_{S/A}$ can be read from Fig. 27, we can write

$$\begin{cases} \tilde{m}_{\chi,\zeta}(0) = \frac{\chi m_2(0) + \alpha I_S^{22}(0)}{2} + \zeta \left| \frac{\chi m_2(0) + \alpha I_S^{22}(0)}{2} \right| \\ \tilde{m}_{\chi,\zeta}(M) \approx \zeta m_2(M) \end{cases}. \quad (136)$$

1262 Clearly, $\tilde{m}_{\chi,\zeta}(M)$ are almost unchanged since the Zeeman field is not that strong here,
1263 and the Hall conductivity formula is reduced into

$$\sigma_H^{\chi\zeta} = \frac{e^2}{2h} [\zeta - \text{sgn}(\tilde{m}_{\chi,\zeta}(0))]. \quad (137)$$

1264 For $\tilde{m}_{\chi,\zeta}(0)$ two cases should be distinguished. When $\alpha I_S^{22}(0) < m_2(0)$,

$$\begin{cases} \tilde{m}_{++}(0) = m_2(0) + \alpha I_S^{22}(0) > 0 \\ \tilde{m}_{+-}(0) = 0 \\ \tilde{m}_{-+}(0) = 0 \\ \tilde{m}_{--}(0) = -m_2(0) + \alpha I_S^{22}(0) < 0 \end{cases}, \quad (138)$$

1265 and we obtain

$$\begin{cases} \sigma_H^{++} = 0 \\ \sigma_H^{+-} = -e^2/2h \\ \sigma_H^{-+} = e^2/2h \\ \sigma_H^{--} = 0 \end{cases}, \quad (139)$$

1266 with total Hall conductivity zero. Interestingly, in this case the symmetric magnetism in
1267 the middle does not even quantitatively change the half quantum mirror Hall phase. On
1268 the other hand, for $\alpha I_S^{22}(0) > m_2(0)$,

$$\begin{cases} \tilde{m}_{++}(0) = m_2(0) + \alpha I_S^{22}(0) > 0 \\ \tilde{m}_{+-}(0) = 0 \\ \tilde{m}_{-+}(0) = -m_2(0) + \alpha I_S^{22}(0) > 0 \\ \tilde{m}_{--}(0) = 0 \end{cases}, \quad (140)$$

1269 and we obtain

$$\begin{cases} \sigma_H^{++} = 0 \\ \sigma_H^{+-} = -e^2/2h \\ \sigma_H^{-+} = 0 \\ \sigma_H^{--} = -e^2/2h \end{cases}, \quad (141)$$

1270 with total Hall conductivity unit upon e^2/h . This unit is fundamentally different the $\mathbf{C} = \mathbf{1}$
1271 as Chern insulator case, since here $\mathbf{1} = \mathbf{1}/2 + \mathbf{1}/2$, with non-vanishing contribution coming
1272 from two metallic bands describing gapless Dirac fermions. It is recognized that the phase

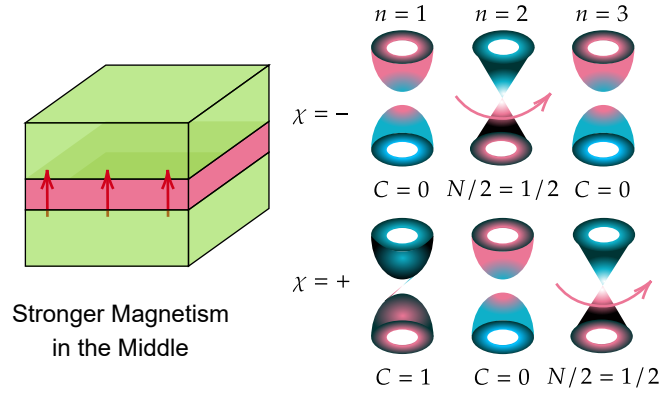


Figure 28: Schematic diagram a stronger magnetic field in the middle of the topological insulator film. The system now contains a pair of gapless Dirac fermions with the same high energy mass signs, together with one non-trivial gapped Dirac cone with unit Chern number. The contributions of these Dirac fermions are synergistic.

1273 transition happens only within $\chi = -$ sub-blocks, where $\zeta = \pm$ Dirac fermions exchange
 1274 their low-energy mass when crossing the qualitative phase transition point $I_S^{22}(\mathbf{0}) = m_2(\mathbf{0})$,
 1275 and by treating approximately $I_S^{22} \approx \alpha t_\perp$, $m_2(\mathbf{0}) \approx m_0$, we see the qualitative critical point
 1276 as

$$\alpha_c^{\text{quali}} = \frac{m_0}{t_\perp} \approx 0.7, \quad (142)$$

1277 which is close to the numerical result.

1278 I_S^{12} as inter- n Dirac fermions coupling plays an important role here. Without this term,
 1279 $n = 1$ and $n = 2$ Dirac fermions will totally be decoupled from Eq. (129), which makes
 1280 the mass exchange between ζ -Dirac fermions with $\chi = -$ impossible. With this term,
 1281 which serves as an avoid-crossing source between ζ -Dirac fermions masses, and obtains its
 1282 maximum nearly after surface to bulk transition of $n = 1$ gapless Dirac fermions, we see
 1283 that the crossing behavior of $\tilde{m}_{-, \zeta}$ at $\Delta_-(\mathbf{k}_{\text{cross}}) = \mathbf{0}$ is prohibited by a non-zero $I_S^{12}(\mathbf{k}_{\text{cross}})$,
 1284 and the two bands are forced to exchange masses before and after $\mathbf{k}_{\text{cross}}$. This is possible
 1285 since $\Delta_-(\mathbf{k}) = \mathbf{0}$ requires that $I_S^{11}(\mathbf{k}) > I_S^{22}(\mathbf{k})$, which can happen only when $n = 1$ surface
 1286 states emerge into the bulk at $\mathbf{k} > \mathbf{k}_c$, where $I_S^{12}(\mathbf{k})$ is also non-zero.

1287 6.1.2 Stronger field in the middle

1288 Encouraged by the mass exchange series diagrams, a natural question to ask is what hap-
 1289 pens when we increase Zeeman strength in the middle further. A first step answer to the
 1290 ask is we will meet a system with higher Hall conductance. For instance, after increasing
 1291 Zeeman field strength to $\alpha = 1.2$, we see from Fig. 29(a) that the Hall conductivity of
 1292 the system becomes $-2e^2/h$ now. For the reason behind, we again look on the effective
 1293 masses presented in Fig. 29(b), where a pair of gapless Dirac cones and one non-trivial
 1294 gapped Dirac cone with mass sign reverse emerge, and essentially, from Eq. 40 and Eq. 44,
 1295 they contribute synergistically to the Hall conductivity, i.e., $1/2 + 1/2 + 1 = 2$ units over
 1296 $-e^2/h$. A careful trace over the effective mass evolution upon increasing α reveals that,
 1297 at this time, $n = 3$ band of $\chi = +$ closes and reopens gap, during which an avoid crossing
 1298 happens and forces it to exchange low energy mass with $n = 1$ band of $\chi = +$, which leads
 1299 to the result above.

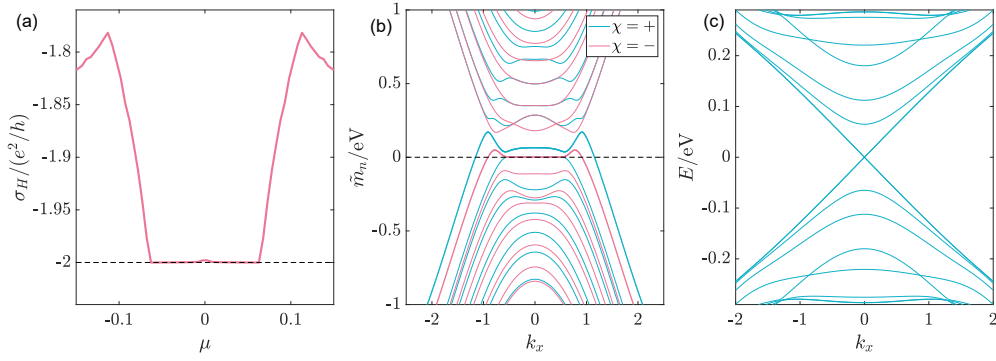


Figure 29: (a) Hall conductance of a metallic QAHE with a stronger magnetic field in the middle. (b) Momentum-dependent effective masses of Dirac fermions in Eq. (70). The masses for gapped surface states have been stressed in the same color. (c) Band dispersion for the system, where the gapless bands at Γ are doubly degenerate. Specifically, here the total layer number of TI film is $L_z = 22$, the magnetic layer number is the middle is 6 , and the Zeeman strength is $V = \alpha t_{\perp}$ with $\alpha = 1.2$.

1300 6.2 Higher Chern Number Insulator

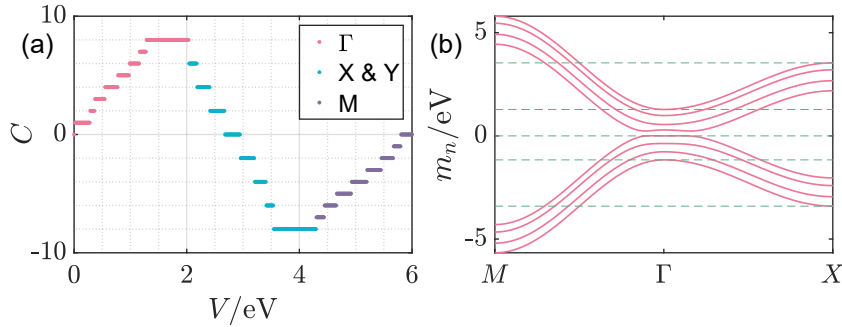


Figure 30: (a) Chern numbers of magnetic TI film with varying uniform Zeeman field strength V . Red, blue and purple dots represent Chern numbers caused by Γ , X/Y and M mass inversions, respectively. (b) Calculated mass $m_n(\mathbf{k})$ along $M-\Gamma-X$ high symmetry line. Green guidance lines have been imposed to reveal either zero-energy surface state plateau or relative magnitude of masses among high symmetry points. Total layer number $L_z = 8$.

1301 Based on magnetic TI film, several proposals to realize higher Chern number has been
 1302 provided [83, 133, 143], among which one theoretical proposal [83] utilizes one-by-one sub-
 1303 band inversion to illustrate the increasing Chern number process. Here the physics behind
 1304 is brought out in a more strict way with a similar picture.

1305 Still we firstly present an example shown in Fig. 30(a) as the Chern numbers of a
 1306 uniformly magnetized TI film with total layer number $L_z = 8$. The algorithm follows [144].
 1307 With increasing the uniform Zeeman strength V , the change of Chern numbers experiences
 1308 three stages: For the relatively weak Zeeman field, the Chern number plateau increases
 1309 step by step, from 0 to 8 , as revealed by red dots; For the Zeeman field with medium
 1310 strength, the Chern number plateau drops from 8 to -8 with 2 as a step, illustrated by
 1311 blue dots; Finally for the relatively strong Zeeman field, the Chern number plateau again
 1312 increases from -8 to 0 one-by-one, shown by purple dots. Notice that under our parameter
 1313 choice we have $m_1(\pi, 0) \sim 2$ eV and $m_1(\pi, \pi) \sim 4.3$ eV.

1314 The Hamiltonian Eq. (72) now best suits to describe the phenomenon, where the
 1315 uniform Zeeman field makes it exact to preserve diagonal blocks. However, due to the
 1316 largely adjustable magnitude of the Zeeman field, Eq. (84) becomes inapplicable here, and
 1317 a more general formula following Eq. 47 is written as [27, 50, 100]

$$C_\chi = -\frac{\text{sgn}(\tilde{m}_\chi(X))}{2}[\text{sgn}(\tilde{m}_\chi(\Gamma)) - \text{sgn}(\tilde{m}_\chi(M))], \quad (143)$$

1318 i.e., it counts for the mass sign-change induced topological phase transition at $\mathbf{X} = (\boldsymbol{\pi}, \mathbf{0})$.
 1319 In this case, the χ -Chern number for each $n = 1, \dots, L_z$ is written as

$$C_\chi^n = -\frac{\text{sgn}(V + \chi m_n(X))}{2}[\text{sgn}(V + \chi m_n(\Gamma)) - \text{sgn}(V + \chi m_n(M))]. \quad (144)$$

1320 In our case, $|m_n(\Gamma)| < |m_n(X)| < |m_n(M)|$, and admittedly, all bulk bands $n \geq 2$ are
 1321 trivial by which I mean $m_n(\Gamma/X/M)$ share the same sign, then focusing on one band and
 1322 increasing V from zero, we see that when V just crosses $|m_n(\Gamma)|$, the band with $\chi m_n < \mathbf{0}$
 1323 increases its Chern number from zero to one; continue to increase V so that it is bigger
 1324 than $m_n(X)$, the corresponding Chern number reverses its sign from $\mathbf{1}$ to $-\mathbf{1}$; and finally
 1325 when V goes beyond the bandwidth $|m_n(M)|$, the band goes back to its trivial phase with
 1326 zero Chern number. Notice that under our assumption $V > \mathbf{0}$, the band $\tilde{\chi} m_n > \mathbf{0}$ is always
 1327 trivial.

1328 It is now clear that the sub-band mass-inversion at Γ , \mathbf{X} and \mathbf{M} points are responsible
 1329 for the change of Chern numbers, or equivalently the anomalous Hall plateaus with quan-
 1330 tum units conductance revealed in Fig. 30(a). As presented in Fig. 30(b), the masses $m_n(\mathbf{k})$
 1331 now shares the property that $\max[m_n(\Gamma)] < \min[m_n(X)]$, $\max[m_n(X)] < \min[m_n(M)]$,
 1332 as revealed by the green guidance lines. Then the Chern number change can be divided
 1333 into three regions with increasing Zeeman field V labelled in Fig. 30(a), i.e., the Γ -mass
 1334 inverse region, the $\mathbf{X}(\mathbf{Y})$ -mass inverse region and the \mathbf{M} -mass inverse region, without cross-
 1335 ing among distinct regions. The physics happened in each region is exactly $L_z = \mathbf{8}$ copies
 1336 illustrated above with increasing V , i.e., the Chern number increases one-by-one in the
 1337 Γ -region each time Zeeman field V crosses some $|m_n(\Gamma)|$ and makes the band non-trivial,
 1338 until it reaches its maximum $C_{\max} = L_z = \mathbf{8}$, then decreases two-by-two in the \mathbf{X} -region
 1339 once V gets bigger than some $|m_n(X)|$, where topological phase transition happens with
 1340 both sides non-trivial, until bottom touching $C_{\min} = L_z - 2L_z = -\mathbf{8}$, and finally the Chern
 1341 number goes back to zero step-by-step in the \mathbf{M} -region as long as V becomes bigger than
 1342 some bandwidth $|m_n(M)|$ and makes corresponding band trivial again. The inverse pro-
 1343 cess happens for an opposite Zeeman field, with Chern number reverse its sign.

1344 6.3 Cooperation between middle and surfaces

1345 Similar to the approach of gapping out surface(s) of a topological insulator film, we can
 1346 gap out the surface states in metallic QAHE with surface magnetism polarized along \mathbf{z}
 1347 direction. In this sense we explore the cooperation between magnetism in the middle and
 1348 at surface(s).

1349 The surface magnetism is chosen to be weak compared to the smallest gap in metallic
 1350 QAHE, and it can thus be treated again as a perturbation. This is simply because gapping
 1351 out the gapless surface needs no threshold over surface magnetic strength. Based on such
 1352 a picture, the physics beneath comes from perturbing two gapless Dirac fermions with
 1353 the same high-energy mass signs in metallic QAHE, whose simplified model Hamiltonian
 1354 reads $H_{\text{MQAHE}} = \mathbf{h} \oplus \mathbf{h}$ with single Dirac cone Hamiltonian

$$\mathbf{h}(\mathbf{k}) = \lambda_{\parallel}(\sin(k_x a)\sigma_x + \sin(k_y b)\sigma_y) + \text{sgn}(V^{\text{mid}})\tilde{m}(\mathbf{k})\sigma_z, \quad (145)$$

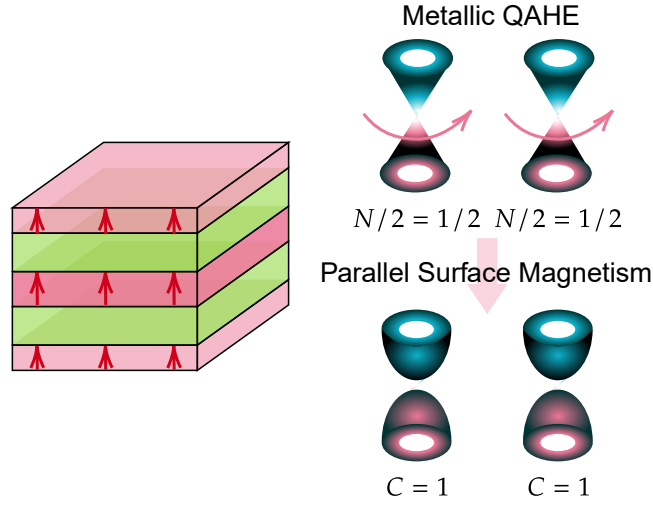


Figure 31: Schematic diagram of the metallic quantized anomalous Hall effect with top and bottom symmetric magnetism parallel to that in the middle. In the case a relatively strong magnetic interaction exists in the middle of the film, while top and bottom states are gapped out by a weak Zeeman field. The system is now an insulator again, and contains a pair of gapped Dirac cones, each carrying Chern number one.

1355 with $\tilde{m}(\mathbf{k}) = \Theta(-m_0(\mathbf{k}))m_0(\mathbf{k})$ identified. Considering now in metallic QAHE, the middle
 1356 Zeeman field does not affect the gapless surface states, then the projection of top and
 1357 bottom Zeeman fields onto the mirror-symmetric surface states can still be written as
 1358 $I_S(\mathbf{k})\tau_0\sigma_z - I_A(\mathbf{k})\tau_y\sigma_z$. And by approximation, we recognize $I_S \equiv V_S^{\text{top}}$, $I_A \equiv V_A^{\text{top}}$ so that
 1359 the phenomenological mass terms read

$$\text{sgn}(V^{\text{mid}})\tilde{m}(\mathbf{k})\tau_0 + V_S^{\text{top}}\tau_0 + V_A^{\text{top}}\tau_y, \quad (146)$$

1360 which can be diagonalized without affecting linear term as

$$\tilde{m}_\zeta(\mathbf{k}) = \text{sgn}(V^{\text{mid}})\tilde{m}(\mathbf{k}) + V_S^{\text{top}} + \zeta V_A^{\text{top}}, \quad (147)$$

1361 with $\zeta = \pm$. Attributing to Eq. (44), we have for a gapped Dirac cone with $V_S^{\text{top}} + \zeta V_A^{\text{top}} \neq 0$,

$$C^\zeta = \frac{1}{2} [\text{sgn}(V_S^{\text{top}} + \zeta V_A^{\text{top}}) + \text{sgn}(V^{\text{mid}})], \quad (148)$$

1362 while for a gapless Dirac cone with $V_S^{\text{top}} + \zeta V_A^{\text{top}} = 0$, according to Eq. (40) we have

$$N^\zeta = \text{sgn}(V^{\text{mid}}), \quad (149)$$

1363 and the corresponding Hall conductivity reads $\sigma_H^\zeta = -Ce^2/h$ or $\sigma_H^\zeta = -Ne^2/2h$ depending
 1364 on gapped or gapless nature, which serves as the starting point for analyzing phases below.

1365 For an instance, adding gap opening \mathbf{z} -Zeeman field at both top and bottom surfaces
 1366 parallel to magnetic polarization in the metallic QAHE system leads to $C = 2$ state, com-
 1367 posed of a pair of non-trivial gapped Dirac fermions each carrying unit Chern number, as
 1368 represented in Fig. 31. Such $C = 2$ state has been observed [143] in a similar magnetic
 1369 structure with an alternate explanation based on the assumption that magnetic layers
 1370 dividing topological insulator film does not hold side surface states, which then turn the
 1371 magnetic insulator-topological insulator multilayer structure into individual $C = 1$ insu-
 1372 lators, each can be explained by discussion over Chern insulator in weak Zeeman field

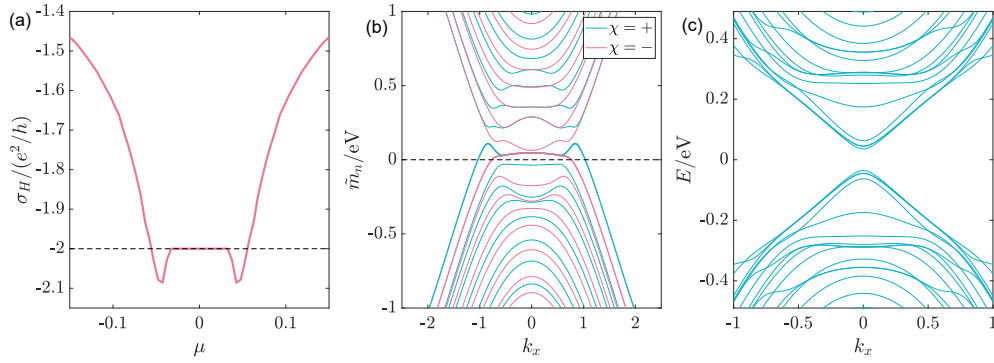


Figure 32: (a) Hall conductance of a metallic QAHE with its top and bottom surface states also gapped by magnetism, whose polarization direction is parallel to the field in the middle. (b) Momentum-dependent effective masses of Dirac fermions in Eq. (70). Due to the symmetric Zeeman configurations, masses are again divided into mirror classes by $\chi = \pm$. The masses for gapped surface states have been stressed in the same color. (c) The band structure of the system. Specifically, here the total layer number of TI film is $L_z = 22$, the magnetic layer numbers at top, middle and bottom are $2, 6, 2$, with mean Zeeman strengths chosen to be $V^{\text{top}} = 0.05$ eV, $V^{\text{mid}} = \alpha t_{\perp}$ with $\alpha = 0.9$, and $V^{\text{bot}} = 0.05$ eV, respectively.

1373 section. Here instead we assume that the magnetism does not alter the bulk gap m_0 very
 1374 much, so that the side surface state goes throughout zone with magnetism. The calculated
 1375 Hall conductivity for one configuration following the assumption is shown in Fig. 32(a),
 1376 where a $C = 2$ plateau is presented inside the top/bottom Zeeman gap for surface states.
 1377 The system is thus identified as a Chern insulator by the gapped band structure shown in
 1378 Fig. 32(c). For simplicity, we have chosen a symmetric surface Zeeman distribution with
 1379 $V_A^{\text{top}} = 0$. Now since $V_S^{\text{top}} > 0, V^{\text{mid}} > 0$, we have mass sign changes at Γ and M for both
 1380 surface states as revealed by mass configurations in Fig. 32(b), and by Eq. (148)

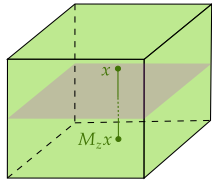
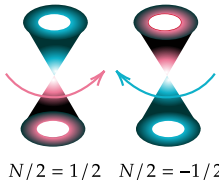
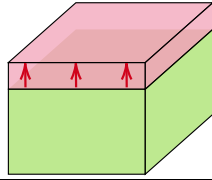
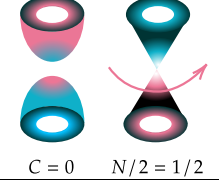
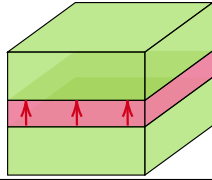
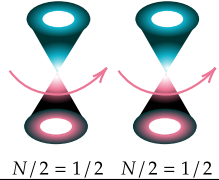
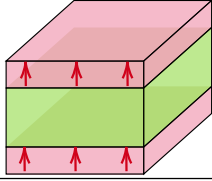
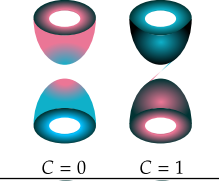
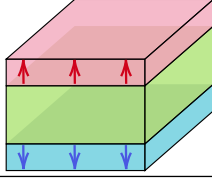
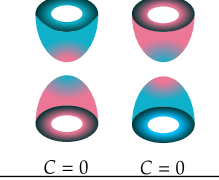
$$C^+ = C^- = 1, \quad (150)$$

1381 which leads to totally a $C = 2$ state.

1382 Now let us switch down V^{top} , which makes $V_S^{\text{top}} = -V_A^{\text{top}} > 0$, accordingly we have
 1383 $N^+ = 1, C^- = 1$, which corresponds to a system with Hall conductivity $3e^2/2h$. Further we
 1384 re-add $V^{\text{top}} = -V^{\text{bottom}} < 0$, which leads to $V_S^{\text{top}} = 0, V_A^{\text{top}} > 0$, and we see $C^+ = 1, C^- = 0$,
 1385 which makes the system a Chern insulator again with unit Chern number. Next we
 1386 reverse V^{bottom} to minus, and $V_S^{\text{top}} < 0, V_A^{\text{top}} = 0$, which makes the system trivial with
 1387 $C^+ = C^- = 0$. Finally, we switch down again V^{top} , and now $V_S^{\text{top}} = -V_A^{\text{top}} < 0$, accordingly
 1388 we have $N^+ = 1, C^- = 0$, which leaves half quantization of Hall conductivity in the system.

1389 Totally, we see that there exists five more additional topologically distinct phases
 1390 upon tuning surface magnetism of metallic QAHE, with Hall conductivities quantized
 1391 into $2, 3/2, 1, 1/2$ and 0 over quantum units, respectively. The topological property of
 1392 these additional phases can be easily verified by calculating their Hall conductivities, or
 1393 reading from their effective mass pictures. The signs of Hall conductivities are inverted
 1394 once we overturn magnetism at both surfaces and in the middle.

Table 3: Summation of main magnetic topological phases discussed. C represents Chern number for a fully occupied band, while N is the half-integer index for a metallic band. The Hall conductance $\sigma_H = -(C + N/2)(e^2/h)$ when the chemical potential lies inside the insulating gap and symmetry constrained regime of the metallic band.

Name of phase	Magnetic structure	Responsible Dirac fermion(s)	Topological index
Half quantum mirror Hall effect		 $N/2 = 1/2$ $N/2 = -1/2$	$N^{\text{mirror}} = 1 - (-1) = 2$
Half quantized anomalous Hall effect		 $C = 0$ $N/2 = 1/2$	$C = 0, N = 1$
Metallic quantized anomalous Hall effect		 $N/2 = 1/2$ $N/2 = 1/2$	$N = 1 + 1 = 2$
Chern insulator		 $C = 0$ $C = 1$	$C = 0 + 1 = 1$
Axion insulator		 $C = 0$ $C = 0$	$C = 0 + 0 = 0$

7 Discussion and conclusion

It is quite remarkable and surprising that so many topologically distinct phases already emerge under such a relatively simple model describing a magnetic topological insulator film. At the core of physics, however, such a descriptive and predictive power of the frame should be estimated. Although, admittedly infinite possibilities exist to explain the phenomena, down to the ground several principles, such as symmetry, topology, emergence and conciseness, have almost fixed the formalism we are willing to adapt in addressing the problem. In our focused questions, particularly regarding the Hall conductance for different species of Dirac fermions in the system, the property of several points in the spectrum is already sufficient to solely determine the result. And to endow physical meaning to these points, we name the points to represent low energy and anomaly. The invariance of laws of physics then suggests that, once we have grasped these key ingredients, the complexities of the more intricate components will naturally fall into place. Below we summarize key points in our paper and extend to further discussions.

The introduced local unitary transformation in \mathbf{k} -space, based on the exact solution, unveils the existence of a pair of gapless Dirac fermions and a series of massive gapped Dirac fermions in a 3D topological insulator film, when viewed as 2D system effectively. This comprehensive understanding of the constitutes inside the TI film is paramount in our discussion.

The Hall conductivity associated with the gapless and gapped Dirac fermions in the TI film are $\pm e^2/2h$ and $\mathbf{0}$, respectively. This results in a half-quantized topological phase, serving as a metallic partner to the insulating quantum spin Hall effect, namely, the half quantum mirror Hall effect in TI film itself. The pairing feature of the gapless Dirac fermions in half quantum mirror Hall effect is summarized in Table 3. It is noteworthy that their existence here is not a result from the Nielsen-Ninomiya theorem, since they are two separable fermions in whole Brillouin zone; rather, it is the mirror symmetry along the opened direction of the TI film that requires the doubling — symmetric and antisymmetric.

The mass term of the gapless Dirac fermion in our study is a regularized one that can be directly expressed on a lattice. However, this regularization comes at the cost of introducing an explicitly parity symmetry-breaking term away from the Dirac point. As a result, the gapless Dirac fermion remains massless at low energy but becomes massive at high energy. In the article, a Heaviside Theta function is utilized to grasp the feature of such a mass term, which exhibits long-range algebraic decay with first power modified by a sinusoidal function, when Fourier transformed into real space. Specifically, it contains a hopping term proportional to $\sim \sin(\Delta l)/\Delta l$, with Δl the distance between sites. Not accidentally, a similar hopping term with the same algebraic decaying order has been used as one way to construct single gapless Dirac fermion on lattice, known as the SLAC fermion [35, 137, 138]. However, it is important to note that in our theory, the phenomenological evasion of locality by the gapless Dirac fermion, residing in effectively 2D space, is a consequence of the bulk property of the 3D TI, where locality is preserved. This phenomenon underscores the concept of bulk-boundary correspondence and suggests that a seemingly unphysical theory in lower dimensions can be attributed to a projection from a higher-dimensional theory. It is noteworthy that the procedure employed here is different from a dimensional reduction, and is not an effective field theory because the Dirac fermion naturally obtains completeness on lattice. Rather, a better similarity can be shared with the quasicrystal containing aperiodic order, which can arise from projections of higher-dimensional periodic lattices [145]. Essentially, both the gapless Dirac fermion containing surface states of a 3D TI, and the quasicrystal from tilings, are physically

1444 realizable systems.

1445 The formalism introduced here, involving the transformation of a confined spatially
 1446 $(n + 1)$ D Dirac Hamiltonian into n D Dirac fermions through the construction of a local
 1447 unitary matrix using solutions from a decomposed 1D Hamiltonian along the confined
 1448 direction, can be generalized to arbitrary dimensions, with the aid of Clifford algebra. In
 1449 particular, initiating from a 4D space modified Dirac equation, a unitary transformation
 1450 yields a pair of gapless Dirac fermions effectively in 3D space. This extension holds the
 1451 potential to enhance our comprehension of the chiral anomaly in the system [56,57]. What
 1452 is more, given that the high-energy components of the two Dirac fermions explicitly break
 1453 the chiral symmetry, they are not obliged to be paired by violating conditions stipulated by
 1454 the Nielsen-Ninomiya theorem. As a result, we can anticipate that when the constrained
 1455 4D Hamiltonian becomes ‘semi-magnetic’, a single gapless Dirac fermion will be observed,
 1456 similar to that in half QAHE.

1457 The introduced magnetism, initially presented as an out-of-plane Zeeman field at the
 1458 mean field level, undergoes the unitary transformation into two momentum-dependent
 1459 matrix Higgs fields $\mathbf{I}_{S/A}(\mathbf{k})$, which obtain non-vanishing values along with the spontaneous
 1460 symmetry breaking that establishes intra-plane ferromagnetic order. The two fields play
 1461 a pivotal role in generating mass to the Dirac fermions through Yukawa-like couplings.
 1462 The nature of the magnetic structure, influencing the distribution and strength of the
 1463 Zeeman field along the open direction, leads to the classification of several topologically
 1464 distinct phases, including the Chern insulator, axion insulator, half-quantized anomalous
 1465 Hall effect and metallic quantized anomalous Hall effect. A summary of their main features
 1466 is presented in Table 3. Essentially, \mathbf{I}_S predominates in the Chern insulator and metallic
 1467 QAHE phases, \mathbf{I}_A takes precedence in the axion insulator, while a collaborative effort
 1468 between both \mathbf{I}_S and \mathbf{I}_A is necessary to achieve the half QAHE.

1469 In the presence of a uniform Zeeman field, the mass of each Dirac fermion in TI film
 1470 is directly modified by a Zeeman field. By tuning the strength of magnetism, sub-band
 1471 inversion happens step-by-step for each Dirac fermion, whose Chern character changes
 1472 correspondingly. Summing those mass-modified Dirac fermions together gives a Chern
 1473 insulator that carries jumping Hall conductance among integers in $[-L_z, L_z]$ over quantum
 1474 unit e^2/h , with L_z the total layer number.

1475 With a relatively weak Zeeman field compared with the bulk gap, focusing solely on
 1476 $n = 1$ matrix elements that act on two gapless Dirac fermions becomes feasible. In this
 1477 scenario, only fields near the two surfaces maximally tune the topological property of the
 1478 TI film by influencing the surface states. This approximation, referred to as the weak
 1479 Zeeman field condition, elucidates the underlying physics behind the Chern insulator,
 1480 axion insulator and half QAHE clearly, with Hall conductance showing $\mathbf{1} + \mathbf{0}$, $\mathbf{0} + \mathbf{0}$ and
 1481 $\mathbf{1}/2 + \mathbf{0}$ quantized nature upon quantum unit.

1482 Under a general strong Zeeman field, the gapped series of Dirac fermions have to be
 1483 involved, and the $n \neq 1$ Higgs components can play a crucial role. The most general
 1484 description is conducted by a further diagonalization over mass terms \mathbf{m}_n and Higgs fields
 1485 $\mathbf{I}_{S/A}$, and the procedure leads to effective masses $\tilde{\mathbf{m}}_n$ for the Dirac fermions, which deter-
 1486 mine the topological property of the system. As discussed, the avoid crossing between $\tilde{\mathbf{m}}_1$
 1487 and $\tilde{\mathbf{m}}_2$ leads to for formation of two gapless Dirac fermions with the same chirality (high
 1488 energy mass sign), which bears a doublet of half quantized Hall conductivity and leads to
 1489 the metallic QAHE. Interestingly, in the case another cut-off over $n = 1, 2$ blocks can be
 1490 made, since the Zeeman field applied should not alter the $n \geq 3$ states dramatically.

1491 When $\mathbf{I}_A = \mathbf{0}$, the mirror symmetry is respected by the system, allowing for the separa-
 1492 tion of the total Hamiltonian by projection operator of mirror symmetry. This separation
 1493 provides valuable insights, such as the application of mirror layer Chern number in a

1494 Chern insulator with a unit Chern number.

1495 It is certainly reasonable but lamentable that we cannot exhaustively list all relevant
1496 topological phases in magnetic topological insulators in the article. The sheer multitude
1497 of possible magnetic distributions makes it impractical to cover every potential scenario.
1498 However, our work lays down a unified framework that enables the depiction of both
1499 discovered and yet-to-be-discovered topological phases in a uniform and consistent manner,
1500 grounded in the conceptualization of the grouped Dirac fermions and the associated mass
1501 generation mechanism. We believe that the diversity and variety of different magnetic
1502 configurations can lead to even richer topological phases within our framework.

1503 Furthermore, as elaborated in Section 4.2, our exploration is not confined solely to
1504 topological phases induced by magnetism, especially a Zeeman field in the TI film. One
1505 illustrative example, as highlighted earlier, involves the duality between \mathbf{z} -Zeeman field
1506 $\boldsymbol{\sigma}_z$ and a special orbital order $\boldsymbol{\tau}_y$. This duality has the potential to generate all topo-
1507 logical phases discussed in the paper, with symmetric and antisymmetric distribution
1508 exchanged for the time reversal breaking $\boldsymbol{\tau}_y$ field. This approach extends beyond the
1509 commonly studied ferromagnetism (or layer-by-layer antiferromagnetism, as observed in
1510 materials like MnBi_2Te_4) induced quantum anomalous Hall effect (QAHE). Moreover,
1511 leveraging the superconducting effect, we can include the superconducting pairing field
1512 into the frame across all pairing symmetries. This inclusion opens avenues for exploration
1513 and determination of the possibilities and conditions necessary for realizing topological
1514 superconductors [146–149] within the solid framework we have established.

1515 An additional intriguing aspect to consider pertain to the symmetries in the system.
1516 The modified Dirac equation model we employed for the topological insulator film encapsu-
1517 lates fruitful symmetries, like the standard time reversal, particle hole, chiral symmetries,
1518 together with the inversion symmetry in each dimension and the 1D mirror symmetry
1519 along each direction. Some of these symmetries play crucial roles in determining our so-
1520 lutions and topological phases in the system. For instance, in solving the separated 1D
1521 Hamiltonian, the utilization of oneDimensional parity and chiral symmetry is essential; the
1522 \mathbf{z} -mirror symmetry becomes decisive for the manifestation of the half quantum mirror Hall
1523 effect, contributing to quantized mirror Hall conductance; despite not a protecting symme-
1524 try in the metallic quantized anomalous Hall effect, the ever existence of the same mirror
1525 symmetry helps us to cut the effective masses into two groups by their mirror labels and
1526 clarifies the mass exchange mechanism. It may prove worthwhile to contemplate a start-
1527 ing point Hamiltonian with lower symmetry or introduce additional symmetry-breaking
1528 fields to assess the stability of these effects. For instance, the half quantum mirror Hall
1529 effect is clearly a metallic twin partner of the quantum spin Hall effect, and it should also
1530 share a general \mathbb{Z}_2 classification scheme depending on the time reversal symmetry solely.
1531 Consequently, it is worthy to give a unified expression for this invariant. Moreover, as we
1532 have shortly discussed, the half-quantization of the gapless Dirac fermion is protected by
1533 the parity invariant regime around the Dirac point, and indeed, this 2D parity symmetry
1534 coexists with the time reversal in our model, which warrants further discussion regarding
1535 their individual impacts on half-quantization. This exploration can be extended to encom-
1536 pass broader symmetries and other kinds of metallic topological phase classes, providing
1537 a comprehensive understanding.

1538 Besides, the exploration of disorder and interaction effects in metallic phases presents
1539 a rich avenue for investigation. As previously discussed, metallic topological phases inher-
1540 ently grapple with disorder effects on their metallic side, wherein mechanisms like skew-
1541 scattering and side-jump alter the transverse transport behavior [91, 94]. The stability of
1542 these phases against disorder, addressed through parameter renormalization, poses a signif-
1543 icant question, akin to considerations in their insulating counterparts [96, 150–152]. More-

1544 over, while the adiabatic criterion justifiably establishes a connection between a gapped
 1545 interacting phase and a non-interacting one by preserving gap opening, it remains elu-
 1546 sive in what way we can say something similar in those metallic phases. Clarifying how
 1547 this linkage can be articulated in the context of these metallic phases poses an ongoing
 1548 challenge.

1549 In short, the interplay between magnetism and topology in 3D TI film is investigated
 1550 under a unified frame, exploiting the Dirac fermion physics and mass generating mecha-
 1551 nism.

1552 Acknowledgements

1553 **Author contributions** S.Q. S. conceived the project. K.-Z. B. and B. F. performed the
 1554 theoretical analysis and simulation. K.-Z. B. and S.Q. S. wrote the manuscript with inputs
 1555 from all authors. All authors contributed to the discussion of the results.

1556 **Funding information** This work was supported by the National Key R&D Program of
 1557 China under Grant No. 2019YFA0308603 and the Research Grants Council, University
 1558 Grants Committee, Hong Kong under Grant Nos. C7012-21G and 17301823.

1559 A Derivation of Eq. (1a)

1560 We start from solving

$$\mathbf{h}(\mathbf{s}) = -is\lambda_{\perp}\partial_z\tau_x + (m_0(\mathbf{k}) + t_{\perp}\partial_z^2)\tau_z, \quad (\text{A.1})$$

1561 with \mathbf{s} defined by eigenvalue of σ_z . All parameters are real with $m_0(\mathbf{k}) = m_0 - t_{\parallel}k^2 > 0$
 1562 to be the criterion for the region where surface states emerge. For the purpose of keeping
 1563 consistence with the lattice model in 2.2, one in fact needs to substitute parameters as

$$\lambda_{\perp} \rightarrow c\lambda_{\perp}, \quad \lambda_{\parallel} \rightarrow a\lambda_{\parallel}, \quad t_{\perp} \rightarrow c^2t_{\perp}, \quad t_{\parallel} \rightarrow a^2t_{\parallel}.$$

1564 However, we would not write in that way explicitly for simplicity. Also, to make discussion
 1565 pithy, we shall omit \mathbf{s} in wavefunction below.

1566 The eigen-problem of $\mathbf{h}(\mathbf{s})$ is a second-order differential equation and allows us to
 1567 set solutions with trial function $\phi = \phi_{\xi}e^{i\xi z}$. Using $\partial_z\phi = i\xi\phi$, $\partial_z^2\phi = -\xi^2\phi$, one has
 1568 equation below:

$$\begin{pmatrix} m_0(\mathbf{k}) - t_{\perp}\xi^2 & s\lambda_{\perp}\xi \\ s\lambda_{\perp}\xi & -m_0(\mathbf{k}) + t_{\perp}\xi^2 \end{pmatrix} \phi = E\phi, \quad (\text{A.2})$$

1569 which readily leads to

$$E^2 - (m_0(\mathbf{k}) - t_{\perp}\xi^2)^2 - \lambda_{\perp}^2\xi^2 = 0, \quad (\text{A.3})$$

1570 and gives

$$\xi_{\alpha}^p = p\xi_{\alpha} = p\sqrt{-\frac{F}{D} + (-1)^{\alpha-1}\frac{\sqrt{R}}{D}}, \quad p = \pm, \quad \alpha = 1, 2, \quad (\text{A.4})$$

1571 where

$$D = 2t_{\perp}^2, \quad F = -2m_0(\mathbf{k})t_{\perp} + s\lambda_{\perp}^2, \quad R = F^2 - 2D(m_0^2(\mathbf{k}) - E^2).$$

1572 For each ξ_{α}^s , one has

$$\phi_{\alpha p} = \begin{pmatrix} s\lambda_{\perp}p\xi_{\alpha} \\ E - m_0(\mathbf{k}) + t_{\perp}\xi_{\alpha}^2 \end{pmatrix}, \quad (\text{A.5})$$

1573 and the general solution would be

$$\Phi = \sum_{ap} C_{ap} \phi_{ap} e^{ip\xi_a z}. \quad (\text{A.6})$$

1574 Now considering finite size along \mathbf{z} direction with top and bottom surfaces located at
1575 $\pm \frac{L}{2}$, respectively, one would have boundary condition

$$\Phi(\pm \frac{L}{2}) = \mathbf{0}, \quad (\text{A.7})$$

1576 applying which one would get four linear equations for coefficients

$$\mathbb{P}(C_{1+}, C_{1-}, C_{2+}, C_{2-})^T = \mathbf{0}, \quad (\text{A.8})$$

1577 and requirement $\det(\mathbb{P}) = 0$ leads to two transcendental equations

$$\frac{m_1 \xi_2}{m_2 \xi_1} = \frac{\tan \xi_2 L/2}{\tan \xi_1 L/2} \quad (\text{A.9a})$$

$$\frac{m_1 \xi_2}{m_2 \xi_1} = \frac{\tan \xi_1 L/2}{\tan \xi_2 L/2} \quad (\text{A.9b})$$

1578 which gives two energies varying with \mathbf{k} , designated as E_+ and E_- , respectively. To be
1579 clearer,

$$E_+ = m_0(k) - t_\perp \frac{\xi_1^2 g^+(\xi_1) - \xi_2^2 g^+(\xi_2)}{g^+(\xi_1) - g^+(\xi_2)}, \quad g^+(\xi) = \frac{\tan(\xi L/2)}{\xi}, \quad (\text{A.10a})$$

$$E_- = m_0(k) - t_\perp \frac{\xi_1^2 g^-(\xi_1) - \xi_2^2 g^-(\xi_2)}{g^-(\xi_1) - g^-(\xi_2)}, \quad g^-(\xi) = \frac{1}{\tan(\xi L/2)\xi}. \quad (\text{A.10b})$$

1580 In common sense, it is time taking E_\pm into expressions of ξ s, together with the coefficients
1581 equations again and solve them. However, that not only is tricky but lacks of physical
1582 insight, and we shall change our perspective.

1583 Notice that under parity operation $\mathbf{z} \leftrightarrow -\mathbf{z}$, $\tau_x \leftrightarrow -\tau_x$ and $\mathbf{h}(\mathbf{s}) \leftrightarrow \mathbf{h}(\mathbf{s})$, then both
1584 $\mathbf{h}(\mathbf{s})$ and \mathbf{H}_{1d} has parity symmetry and the general solution should contain two factors
1585 below considering the boundary condition:

$$\begin{cases} f_+(z) = \frac{\cos(\xi_1 z)}{\cos(\xi_1 L/2)} - \frac{\cos(\xi_2 z)}{\cos(\xi_2 L/2)} \\ f_-(z) = \frac{\sin(\xi_1 z)}{\sin(\xi_1 L/2)} - \frac{\sin(\xi_2 z)}{\sin(\xi_2 L/2)} \end{cases}, \quad (\text{A.11})$$

1586 where the subscripts refer to even or odd parity. Now we can assume that for energy E ,
1587 $\mathbf{h}(\mathbf{s})$ has solution

$$\phi = \tilde{c} f_+ + \tilde{d} f_- = \begin{pmatrix} \tilde{c}_1 f_+ + \tilde{d}_1 f_- \\ \tilde{c}_2 f_+ + \tilde{d}_2 f_- \end{pmatrix}, \quad (\text{A.12})$$

1588 and the two-line eigen-equation $\mathbf{h}(\mathbf{s})\phi = E\phi$ gives, for the first line

$$\tilde{d}_2 = it_\perp \eta_1 \tilde{c}_1 / s \lambda_\perp, \quad (\text{A.13a})$$

$$\tilde{c}_2 = -it_\perp \eta_2 \tilde{d}_1 / s \lambda_\perp, \quad (\text{A.13b})$$

1589 which leads to

$$\phi_1^+ = C_1^+ \begin{pmatrix} -is\lambda_\perp f_+ \\ t_\perp \eta_1 f_- \end{pmatrix}, \quad E = E_+, \quad (\text{A.14a})$$

$$\phi_1^- = C_1^- \begin{pmatrix} is\lambda_\perp f_- \\ t_\perp \eta_2 f_+ \end{pmatrix}, \quad E = E_-; \quad (\text{A.14b})$$

1590 and for the second line,

$$\tilde{d}_1 = -it_\perp \eta_1 \tilde{c}_2 / s\lambda_\perp, \quad (\text{A.15a})$$

$$\tilde{c}_1 = it_\perp \eta_2 \tilde{d}_2 / s\lambda_\perp, \quad (\text{A.15b})$$

1591 which leads to

$$\phi_2^+ = C_2^+ \begin{pmatrix} t_\perp \eta_1 f_- \\ is\lambda_\perp f_+ \end{pmatrix}, \quad E = -E_+, \quad (\text{A.16a})$$

$$\phi_2^- = C_2^- \begin{pmatrix} t_\perp \eta_2 f_+ \\ -is\lambda_\perp f_- \end{pmatrix}, \quad E = -E_-, \quad (\text{A.16b})$$

1592 by defining two coefficients

$$\eta_1 = \frac{\xi_1^2 - \xi_2^2}{\xi_1 \cot(\xi_1 L/2) - \xi_2 \cot(\xi_2 L/2)}, \quad (\text{A.17a})$$

$$\eta_2 = \frac{\xi_1^2 - \xi_2^2}{\xi_1 \tan(\xi_1 L/2) - \xi_2 \tan(\xi_2 L/2)}, \quad (\text{A.17b})$$

1593 with \mathbf{C} is the norm, and super and lower indices represent E_\pm and line index, respectively.
1594 Clearly, $\mathbf{C}_1^\iota = \mathbf{C}_2^\iota$ is identified, and $\phi_1^\iota = -i\tau_y \phi_2^\iota$ as they are chiral partners ($\iota = \pm$).

1595 Solution above seems to give four solutions, mathematical restriction, however, tells
1596 that equations from different lines for the same set of coefficients must stand simulta-
1597 neously, i.e., (A.14a) \Leftrightarrow (A.16b) and (A.14b) \Leftrightarrow (A.16a), which gives us two relations as
1598

$$\mathbf{1} = \left| \frac{it_\perp \eta_1}{s\lambda_\perp} \cdot \frac{it_\perp \eta_2}{s\lambda_\perp} \right| \Rightarrow |\eta_1 \eta_2| = \frac{\lambda_\perp^2}{t_\perp^2}, \quad (\text{A.18a})$$

$$E_+ = -E_-, \quad (\text{A.18b})$$

1599 and the latter is also a physical result from Dirac equation. Then, we only have two
1600 independent solutions for one $\mathbf{h}(\mathbf{s})$ sub-block, say Eq. (A.14a) and Eq. (A.16a). Formal
1601 combination of equations for the simultaneous-standing equations from different lines again
1602 leads to

$$E^2 - (m_0(\mathbf{k}) - t_\perp \xi^2)^2 - \lambda_\perp^2 \xi^2 = 0. \quad (\text{A.19})$$

1603 Then we see that the guessing solution not only satisfies the boundary condition, but also
1604 satisfies all $E - \xi$ equations, thus it is indeed our solution.

1605 Notice that, by Eq (A.4), ξ_α are both complex or not complex for a given energy,
1606 where complex means both real and imaginary parts of ξ are non-vanishing, determined
1607 by the sign of \mathbf{R} . This information, combined with property of trigonometric/hyperbolic
1608 function leads to the conclusion that quadratic form $f_+^* f_-$ and η (at certain $(\mathbf{k}, \mathbf{z}, \mathbf{E})$) are
1609 always real. Essentially, f_\pm are either real or purely imaginary.

1610 Now, we restore \mathbf{s} explicitly and extract

$$\varphi(\mathbf{s}) = \phi_1^{s,+}, \quad \chi(\mathbf{s}) = \phi_2^{s,+} \quad (\text{A.20})$$

1611 as two solutions for $\mathbf{h}(\mathbf{s})$ for basis construction. Then by defining

$$\begin{cases} m = E_+ = m_0(k) - t_\perp \frac{\xi_1^2 g(\xi_1) - \xi_2^2 g(\xi_2)}{g(\xi_1) - g(\xi_2)}, \\ g(\xi) = \frac{\tan(\xi L/2)}{\xi}, \\ \eta = \frac{\xi_1^2 - \xi_2^2}{\xi_1 \cot(\xi_1 L/2) - \xi_2 \cot(\xi_2 L/2)}, \\ C = C_1^+ = C_2^+, \end{cases} \quad (\text{A.21})$$

1612 one obtains four projecting basis in certain sequence as

$$\begin{aligned} \Phi_1 &= \begin{pmatrix} \varphi(+) \\ 0 \\ 0 \end{pmatrix} = C \begin{pmatrix} -i\lambda_\perp f_+ \\ t_\perp \eta f_- \\ 0 \end{pmatrix}, \\ \Phi_2 &= \begin{pmatrix} 0 \\ \chi(-) \\ -i\lambda_\perp f_+ \end{pmatrix} = C \begin{pmatrix} 0 \\ 0 \\ t_\perp \eta f_- \end{pmatrix}, \\ \Phi_3 &= \begin{pmatrix} \chi(+) \\ 0 \\ 0 \end{pmatrix} = C \begin{pmatrix} t_\perp \eta f_- \\ i\lambda_\perp f_+ \\ 0 \end{pmatrix}, \\ \Phi_4 &= \begin{pmatrix} 0 \\ \varphi(-) \\ t_\perp \eta f_- \end{pmatrix} = C \begin{pmatrix} 0 \\ 0 \\ i\lambda_\perp f_+ \end{pmatrix}, \end{aligned} \quad (\text{A.22})$$

1613 with energy $(\mathbf{m}, -\mathbf{m}, -\mathbf{m}, \mathbf{m})$, respectively. Notice that $\Phi_{3,4}$ are chiral partners of $\Phi_{1,2}$ by
1614 $-\mathbf{i}\tau_y$, respectively. To obtain \mathbf{m} , a set of closed equations need to be solved

$$m = m_0(k) - t_\perp \frac{\xi_1^2 g^+(\xi_1) - \xi_2^2 g^+(\xi_2)}{g^+(\xi_1) - g^+(\xi_2)}, \quad (\text{A.23a})$$

$$\xi_\alpha = \sqrt{-\frac{F}{D} + (-1)^{\alpha-1} \frac{\sqrt{R}}{D}}, \quad \alpha = 1, 2, \quad (\text{A.23b})$$

1615 where

$$\begin{cases} g^+(\xi) = \tan(\xi L/2)/\xi \\ D = 2t_\perp^2 \\ F = -2m_0(k)t_\perp + \lambda_\perp^2 \\ R = F^2 - 2D(m_0^2(k) - m^2) \end{cases} \quad (\text{A.24})$$

1616 Basically, there are three variables $(\mathbf{m}, \xi_1, \xi_2)$ with three equations, then they could be
1617 determined exactly.

1618 A.1 Symmetry analysis of solutions

1619 Firstly, as we have stated, the chiral symmetry τ_y is respected in Eq. (A.1) since $\{\mathbf{h}(\mathbf{s}), \tau_y\} = \mathbf{0}$,
1620 and this symmetry is reflected in our solutions by $\varphi(\mathbf{s}) = -i\tau_y\chi(\mathbf{s})$ with opposite energies.

1621 Meanwhile, we have relied on the help from the 1D parity symmetry which is a reflection
1622 along \mathbf{z} direction, or simply, the \mathbf{z} -parity \mathcal{P}_z , which acts on the basis as

$$\Phi(\mathbf{z}) \xrightarrow{\mathcal{P}_z} \tau_z \Phi(-\mathbf{z}), \quad (\text{A.25})$$

1623 with τ_z the unitary matrix related to inner degrees of freedom transformation. Now since
1624 $f_{\pm}(\mathbf{z}) = \pm f_{\pm}(-\mathbf{z})$, we identify that $\Phi_{1,4}$ ($\Phi_{2,3}$) are even (odd) under \mathbf{z} -parity, and corre-
1625 spondingly, under representation of Φ , the unitary matrix related to \mathbf{z} -parity is written as
1626 $\tau_z \sigma_z$.

1627 There exists in fact a hidden symmetry in the model, namely, the mirror symmetry
1628 about the \mathbf{x} - \mathbf{y} plane. Effectively, it will also bring \mathbf{z} to $-\mathbf{z}$ as an inversion, but with an
1629 additional operation that rotates spin angular momentum by π phase, i.e., such a \mathbf{z} -Mirror
1630 symmetry \mathcal{M}_z is a combination of \mathcal{P}_z and a \mathcal{C}_{2z} rotation, which then acts on the basis as

$$\Phi(\mathbf{z}) \xrightarrow{\mathcal{M}_z} \sigma_z \tau_z \Phi(-\mathbf{z}), \quad (\text{A.26})$$

1631 and classifies $\Phi_{1,2}$ ($\Phi_{3,4}$) into \mathbf{z} -mirror even (odd) states. Accordingly, under Φ represen-
1632 tation this operator has form $\tau_z \sigma_0$. Then combined with the spin index $\mathbf{s} = \pm$ appeared
1633 in $\varphi(\mathbf{s}), \chi(\mathbf{s})$, we can further assign Φ_i to be $\Phi_{\chi, \mathbf{s}}$ with χ, \mathbf{s} labelling mirror and spin- \mathbf{z}
1634 index as

$$\begin{aligned} \Phi_{++} &= \Phi_1, & \Phi_{+-} &= \Phi_2, \\ \Phi_{-+} &= \Phi_3, & \Phi_{--} &= \Phi_4. \end{aligned} \quad (\text{A.27})$$

1635 The single $\mathbf{h}(\mathbf{s})$ does not share time reversal symmetry, since under $\mathcal{T} = i\sigma_y \mathcal{K}$,
1636 $\mathbf{h}(+) \leftrightarrow \mathbf{h}(-)$, i.e., H_{1d} owns this symmetry. Also given by the fact that time rever-
1637 sal keeps energy unconverted, one finds $\Phi_4 = e^{i\theta} \mathcal{T} \Phi_1$, $\Phi_2 = e^{i\theta} \mathcal{T} \Phi_3$, where $\theta = \mathbf{0}$ or π
1638 depending on \mathbf{k}, \mathbf{E} . The essential point to get avoid of subtle f_{\pm}^* is to notice that they are
1639 either both real or imaginary, as stated above, while η is always real. Also notice that we
1640 did not write \mathbf{k} explicitly since $H_{1d}(\mathbf{k}) = H_{1d}(-\mathbf{k})$.

1641 The combination of time reversal and chiral symmetries gives rise to a particle hole
1642 symmetry, which, when implanted over basis, reads $\varphi(\mathbf{s}) = e^{i\theta} \varphi^*(\bar{\mathbf{s}}) = e^{i\theta} [-i\tau_y \chi(\bar{\mathbf{s}})]^*$,
1643 with $\bar{\mathbf{s}} = -\mathbf{s}$ identified.

1644 Similar analysis applies for the lattice model, and the projected $\mathcal{P}_z, \mathcal{M}_z$ share the same
1645 matrix form above.

1646 A.2 Equivalent block Hamiltonian

1647 The projection procedure works under the given basis representation $H_{TI}(\mathbf{k})$, which is
1648 formally $H = \langle \Phi | H_{TI}(\mathbf{k}) | \Phi \rangle$, with

$$(H)_{ij}^{nn'} = \int d\mathbf{z} (\Phi_i^n(\mathbf{z}))^\dagger H_{TI}(\mathbf{k}, \mathbf{z}) \Phi_j^{n'}(\mathbf{z}), \quad (\text{A.28})$$

1649 where the integral is done from $-L/2$ to $L/2$. Clearly, projection on H_{1d} would give
1650 $\text{diag}(m, -m, -m, m)$, then we only need to deal with $H_{\parallel}(\mathbf{k}) = \lambda_{\parallel}(\mathbf{k} \cdot \boldsymbol{\sigma}) \tau_x = \lambda_{\parallel}(k_x \sigma_x + k_y \sigma_y) \tau_x$
1651 term. Since $H_{\parallel}(\mathbf{k})$ is purely off-diagonal, it is easy to conclude that

$$\begin{aligned} \langle \Phi_i^n | H_{\parallel} | \Phi_i^{n'} \rangle &= 0, \quad i = 1, 2, 3, 4 \\ \langle \Phi_1^n | H_{\parallel} | \Phi_3^{n'} \rangle &= 0 = \langle \Phi_2^n | H_{\parallel} | \Phi_4^{n'} \rangle. \end{aligned}$$

1652 Then only four terms need consideration by hermicity, among which

$$\begin{aligned}\langle \Phi_1^n | H_{\parallel} | \Phi_4^{n'} \rangle &= \lambda_{\parallel} k_{\perp} |C^n C^{n'}| \int d\mathbf{z} i \lambda_{\perp} t_{\perp} [\eta^n (f_+^n)^* f_-^{n'} + \eta^{n'} (f_-^n)^* f_+^{n'}] = 0, \\ \langle \Phi_2^n | H_{\parallel} | \Phi_3^{n'} \rangle &= \lambda_{\parallel} k_{\perp} |C^n C^{n'}| \int d\mathbf{z} i \lambda_{\perp} t_{\perp} [\eta^n (f_-^n)^* f_+^{n'} + \eta^{n'} (f_+^n)^* f_-^{n'}] = 0,\end{aligned}$$

1653 as $f_- f_+$ is odd to \mathbf{z} . Here $k_{\pm} = k_x \pm i k_y$ is defined. Then, the only remaining terms are

$$\begin{aligned}\langle \Phi_1^n | H_{\parallel} | \Phi_2^{n'} \rangle &= \int d\mathbf{z} \lambda_{\parallel} k_{\perp} \varphi^{\dagger}(\lambda_{\perp}) \tau_x \chi(-\lambda_{\perp}) = \lambda_{\parallel} k_{\perp} \delta_{nn'}, \\ \langle \Phi_3^n | H_{\parallel} | \Phi_4^{n'} \rangle &= \int d\mathbf{z} \lambda_{\parallel} k_{\perp} \varphi^{\dagger}(\lambda_{\perp}) \tau_x \chi(-\lambda_{\perp}) = \lambda_{\parallel} k_{\perp} \delta_{nn'},\end{aligned}$$

1654 where the normalization condition is used. And finally we arrive at the block Hamiltonian

$$H(\mathbf{k}) = \bigoplus_n \lambda_{\parallel} \tau_0 (\mathbf{k} \cdot \boldsymbol{\sigma}) + m_n(\mathbf{k}) \tau_z \sigma_z, \quad (\text{A.29})$$

1655 as Eq. (1a). Here, notice that the spin degree of freedom is fully preserved as $\boldsymbol{\sigma}$, while the
1656 newly-defined $\boldsymbol{\tau}$ owns different meaning from the original one.

1657 To make the transformation more formal, we define the transformation matrix

$$U^c(\mathbf{k}, \mathbf{z}) = (\{\{\Phi\}_i\}^n)(\mathbf{k}, \mathbf{z}), \quad (\text{A.30})$$

1658 where the double brackets mean that we arrange $i = 1, 2, 3, 4$ index inside each $n = 1, 2, \dots$,
1659 and by written more straightforwardly,

$$U^c = (\Phi^1, \Phi^2, \dots), \quad \Phi^n = (\Phi_1^n, \Phi_2^n, \Phi_3^n, \Phi_4^n). \quad (\text{A.31})$$

1660 This transformation then brings the Hamiltonian of the boundary constrained topological
1661 insulator film $H_{TI}(\mathbf{k}, -i\partial_z)$ into the direct sum form of Dirac fermions by

$$H(\mathbf{k}) = \int d\mathbf{z} (U^c)^{\dagger}(\mathbf{k}, \mathbf{z}) H_{TI}(\mathbf{k}, -i\partial_z) U^c(\mathbf{k}, \mathbf{z}). \quad (\text{A.32})$$

1662 A.3 Analytic expression for mass term

1663 The proof has been posted separately [33], and here is a repetition. Analytic expression
1664 for effective mass $\mathbf{m}(\mathbf{k})$ is obtained in the $L \rightarrow \infty$ case as a thick limit, however, notice
1665 that finite-size correction to $\mathbf{m}(\mathbf{k})$ decays exponentially with thickness [38], our proof here
1666 is suitable even for a thin film. Closed $E - \xi$ equations are

$$\begin{cases} \xi_1^2 + \xi_2^2 = \frac{2m_0(k)t_{\perp} - \lambda_{\perp}^2}{t_{\perp}^2} \\ \xi_1^2 \xi_2^2 = \frac{m_0(k)^2 - E^2}{t_{\perp}^2} \\ E = m_0(k) - t_{\perp} \frac{\xi_1^2 g^+(\xi_1) - \xi_2^2 g^+(\xi_2)}{g^+(\xi_1) - g^+(\xi_2)} \end{cases}, \quad (\text{A.33})$$

1667 where $g^+(\xi) = \tan(\xi L/2)/\xi$. We shall assume $\lambda_{\perp} > 0$, $t_{\perp} > 0$ in the following discussion,
1668 without losing generality, and $m_0(\mathbf{k})$ controls the expression form.

1669 The classification on $\tan(\xi L/2)$ leads to

$$\lim_{L \rightarrow +\infty} \tan(\xi L/2) = \begin{cases} i, & \text{Im}(\xi) > 0 \\ \text{N.A.}, & \text{Im}(\xi) = 0 \\ -i, & \text{Im}(\xi) < 0 \end{cases} \quad (\text{A.34})$$

1670 And three basic cases are separated as

$$\begin{cases} \text{Im}(\xi_1) > 0 > \text{Im}(\xi_2) \\ \text{Im}(\xi_{1,2}) > 0 \\ \text{Im}(\xi_1) = 0, \text{Im}(\xi_2) > 0 \end{cases}, \quad (\text{A.35})$$

1671 while other cases could be obtained similarly.

1672 **Case I.** ($\text{Im}(\xi_1) > 0 > \text{Im}(\xi_2)$)

1673 Now $\tan(\xi_1 L/2) = i = -\tan(\xi_2 L/2)$ ($L \rightarrow +\infty$ ignored), and

$$\begin{cases} \xi_1^2 + \xi_2^2 = \frac{2m_0(k)t_\perp - \lambda_\perp^2}{t_\perp^2} \\ \xi_1^2 \xi_2^2 = \frac{m_0(k)^2 - E^2}{t_\perp^2} \\ E = m_0(k) - t_\perp \xi_1 \xi_2 \end{cases}, \quad (\text{A.36})$$

1674 where the second and third equations lead to

$$m_0(k)^2 - E^2 = (m_0(k) - E)^2, \quad (\text{A.37})$$

1675 which offers two possible solutions $E = 0$ or $E = m_0(k)$.

1676 **I.** ($E = 0$) This leads to

$$\begin{cases} \xi_1 \xi_2 = \frac{m_0(k)}{t_\perp} \\ \xi_1^2 + \xi_2^2 = \frac{2m_0(k)t_\perp - \lambda_\perp^2}{t_\perp^2} \end{cases}. \quad (\text{A.38})$$

1677 Requiring $\text{Im}(\xi_1) > 0 > \text{Im}(\xi_2)$ then gives

$$\begin{cases} \xi_1 + \xi_2 = \begin{cases} 2u\sqrt{4\gamma-1}, & \gamma > 1/4 \\ 2ui\sqrt{1-4\gamma}, & \gamma < 1/4 \end{cases} \\ \xi_1 - \xi_2 = 2ui \end{cases}, \quad (\text{A.39})$$

1678

$$\begin{cases} \gamma = m_0(k)t_\perp/\lambda_\perp^2 \\ u = \lambda_\perp/2t_\perp \end{cases}, \quad (\text{A.40})$$

1679 which offers:

1680 • $\gamma > 1/4$:

$$\begin{cases} \xi_1 = u(\sqrt{4\gamma-1} + i) \\ \xi_2 = u(\sqrt{4\gamma-1} - i) \end{cases}; \quad (\text{A.41})$$

1681 • $\gamma < 1/4$:

$$\begin{cases} \xi_1 = iu(\sqrt{1-4\gamma} + 1) \\ \xi_2 = iu(\sqrt{1-4\gamma} - 1) \end{cases}. \quad (\text{A.42})$$

1682 The latter condition stands only when $\gamma > 0$ as for $\text{Im}(\xi_2) < 0$.

1683 **II. ($E = m_0(k)$)** This leads to

$$\begin{cases} \xi_1 \xi_2 = 0 \\ \xi_1^2 + \xi_2^2 = \frac{2m_0(k)t_\perp - \lambda_\perp^2}{t_\perp^2} \end{cases}, \quad (\text{A.43})$$

1684 and one of $\xi_\alpha = 0$ is unavoidable, which fails the precondition and is abandoned, i.e.,
1685 $E = m_0(k)$ is not a solution in the case.

1686 **Case II. ($\text{Im}(\xi_{1,2}) > 0$)**

1687 Now $\tan(\xi_1 L/2) = i = \tan(\xi_2 L/2)$ ($L \rightarrow +\infty$ ignored), and

$$\begin{cases} \xi_1^2 + \xi_2^2 = \frac{2m_0(k)t_\perp - \lambda_\perp^2}{t_\perp^2} \\ \xi_1^2 \xi_2^2 = \frac{m_0(k)^2 - E^2}{t_\perp^2} \\ E = m_0(k) + t_\perp \xi_1 \xi_2 \end{cases}, \quad (\text{A.44})$$

1688 then the second and third equations above leads to

$$m_0(k)^2 - E^2 = (m_0(k) - E)^2, \quad (\text{A.45})$$

1689 which gives us two possible solutions as $E = 0$ or $E = m_0(k)$.

1690 **I. ($E = 0$)** This condition leads to

$$\begin{cases} \xi_1 \xi_2 = -\frac{m_0(k)}{t_\perp} \\ \xi_1^2 + \xi_2^2 = \frac{2m_0(k)t_\perp - \lambda_\perp^2}{t_\perp^2} \end{cases}. \quad (\text{A.46})$$

1691 Requirement $\text{Im}(\xi_{1,2}) > 0$ then gives

$$\begin{cases} \xi_1 + \xi_2 = 2ui \\ \xi_1 - \xi_2 = \begin{cases} 2u\sqrt{4\gamma-1}, & \gamma > 1/4 \\ 2ui\sqrt{1-4\gamma}, & \gamma < 1/4 \end{cases} \end{cases}, \quad (\text{A.47})$$

1692 which offers:

1693 • $\gamma > 1/4$:

$$\begin{cases} \xi_1 = u(\sqrt{4\gamma-1} + i) \\ \xi_2 = u(-\sqrt{4\gamma-1} + i) \end{cases}; \quad (\text{A.48})$$

1694 • $\gamma < 1/4$:

$$\begin{cases} \xi_1 = iu(\sqrt{1-4\gamma} + 1) \\ \xi_2 = iu(-\sqrt{1-4\gamma} + 1) \end{cases}. \quad (\text{A.49})$$

1695 The latter condition stands only when $\gamma > 0$ as for $\text{Im}(\xi_2) > 0$.

1696 **II. ($E = m_0(k)$)** This leads to

$$\begin{cases} \xi_1 \xi_2 = 0 \\ \xi_1^2 + \xi_2^2 = \frac{2m_0(k)t_\perp - \lambda_\perp^2}{t_\perp^2} \end{cases}, \quad (\text{A.50})$$

1697 and again one of $\xi_\alpha = \mathbf{0}$ is unavoidable, and one concludes $E = m_0(\mathbf{k})$ is not a solution in
 1698 the case.

1699 **Case III. ($\text{Im}(\xi_1) = 0, \text{Im}(\xi_2) > 0$)**

1700 By guessing $E = m_0(\mathbf{k})$, we have

$$\begin{cases} \xi_1 \xi_2 = 0 \\ \xi_1^2 + \xi_2^2 = \frac{2m_0(\mathbf{k})t_\perp - \lambda_\perp^2}{t_\perp^2} \end{cases}, \quad (\text{A.51})$$

1701 which gives

$$\begin{cases} (\xi_1 + \xi_2)^2 = 4u^2(2\gamma - 1) \\ (\xi_1 - \xi_2)^2 = 4u^2(2\gamma - 1) \end{cases}, \quad (\text{A.52})$$

1702 and choosing

$$\begin{cases} \xi_1 = 0 \\ \xi_2 = 2ui\sqrt{1-2\gamma} \end{cases}, \quad (\text{A.53})$$

1703 fulfills the requirement. Notice that $\gamma < 1/2$ is assumed, which should not bother the
 1704 self-consistent solution. Meanwhile, since $\xi_1 = \mathbf{0}$ leads to degenerate eigenvalue $\pm\xi_1$, then
 1705 one should generally assume another solution as

$$(A + Bz)e^{i\xi_1 z} \phi \Big|_{\xi_1=0, E=m_0(\mathbf{k})},$$

1706 which, however, only gives result that $B = \mathbf{0}$ while A is arbitrary, which passes no additional
 1707 information.

1708 Retrospecting the definition $\gamma = m_0(\mathbf{k})t_\perp/\lambda_\perp^2$, the discussion above naturally leads to
 1709 the conclusion that the lowest eigenenergy of H_{1d} reads

$$E = \begin{cases} 0, & m_0(\mathbf{k}) > 0 \\ m_0(\mathbf{k}), & m_0(\mathbf{k}) < 0 \end{cases}, \quad (\text{A.54})$$

1710 or by re-defining lowest $E(\mathbf{k})$ as $m_1(\mathbf{k})$, we write

$$m_1(\mathbf{k}) = \Theta(-m_0(\mathbf{k}))m_0(\mathbf{k}),$$

1711 as result mention in Eq. (11)

1712 A.4 Finite-size correction to mass term

1713 We could in fact conserve lowest order correction to see the finite size gap when L is
 1714 not that large. For ξ_1 and ξ_2 , one could approximately get lowest order correction for
 1715 $\tan(\xi L/2)$ by treating $\beta^{\pm L/2}$ as small quantity (depend on sign of $\text{Im}(\xi)$)

$$\tan(\xi L/2) \approx \begin{cases} i(1 - 2\beta^L), & \text{Im}(\xi) > 0 \\ -i(1 - 2\beta^{-L}), & \text{Im}(\xi) < 0 \end{cases}. \quad (\text{A.55})$$

1716 Also notice that from the original $E - \xi$ equation

$$E^2 - (m_0(\mathbf{k}) - t_\perp \xi^2)^2 - \lambda_\perp^2 \xi^2 = 0,$$

1717 which could be further split into (when $E = 0$ as zeroth-order)

$$t_\perp \xi^2 \pm i\lambda_\perp \xi - m_0(\mathbf{k}) = 0, \quad (\text{A.56})$$

1718 one solves

$$\xi = \frac{s_1 i \lambda_{\perp} + s_2 \sqrt{4m_0(k)t_{\perp} - \lambda_{\perp}^2}}{2t_{\perp}} = u(is_1 + s_2 \sqrt{4\gamma - 1}), \quad (\text{A.57})$$

1719 where $s_1, s_2 = \pm$ without restriction. Notice that in real calculation, one needs to specify
1720 which branch $\xi_{1,2}$ lie in, but such choice will not affect the final result as long as chosen
1721 $\xi_{1,2}$ satisfy zeroth-order solution. Now again we have two cases below:

1722 • $\gamma > 1/4$, we choose

$$\begin{cases} \xi_1 = \xi_2^* \\ \text{Im}(\xi_1) > 0 > \text{Im}(\xi_2) \\ \text{Re}(\xi_1) = \text{Re}(\xi_2) > 0 \end{cases}, \quad (\text{A.58})$$

1723 as main branch condition, then

$$\begin{cases} \tan(\xi_1 L/2) \approx i(1 - 2\beta_1^L) \\ \tan(\xi_2 L/2) \approx -i(1 - 2\beta_2^{-L}) \end{cases}, \quad (\text{A.59})$$

1724 and

$$E(k) \approx (m_0(k) - t_{\perp} \xi_1 \xi_2) + 2t_{\perp} \xi_1 \xi_2 \frac{\xi_1 - \xi_2}{\xi_1 + \xi_2} (e^{i\xi_1 L} - e^{-i\xi_2 L}).$$

1725 Notice that first term in bracket is zeroth order as $E \approx 0$. Now, it is time to utilize four
1726 solutions in Eq. (A.57). By main branch condition above, accordingly we choose

$$\begin{cases} \xi_1 = u(\sqrt{4\gamma - 1} + i) \\ \xi_2 = u(\sqrt{4\gamma - 1} - i) \end{cases}, \quad (\text{A.60})$$

1727 considering that $\gamma > 1/4$ in this zone. Afterwards, one obtains

$$E(k) \approx -\frac{4m_0(k)}{\sqrt{4\gamma - 1}} \sin(u\sqrt{4\gamma - 1}L) e^{-uL}. \quad (\text{A.61})$$

1728 Low energy surface state mass shows both exponentially decay and oscillating behavior.

1729 • $0 < \gamma < 1/4$, we choose

$$\begin{cases} \text{Im}(\xi_1) > 0 \\ \text{Im}(\xi_2) > 0 \end{cases}, \quad (\text{A.62})$$

1730 as main branch condition, then

$$\begin{cases} \tan(\xi_1 L/2) \approx i(1 - 2\beta_1^L) \\ \tan(\xi_2 L/2) \approx i(1 - 2\beta_2^L) \end{cases}, \quad (\text{A.63})$$

1731

$$E(k) \approx (m_0(k) + t_{\perp} \xi_1 \xi_2) - 2t_{\perp} \xi_1 \xi_2 \frac{\xi_1 + \xi_2}{\xi_1 - \xi_2} (e^{i\xi_1 L} - e^{i\xi_2 L}),$$

1732 where first term in bracket is again zeroth order energy approaching zero. Again, utilizing
1733 four solutions in Eq. (A.57) with main branch condition above, we choose

$$\begin{cases} \xi_1 = iu(1 + \sqrt{1 - 4\gamma}) \\ \xi_2 = iu(1 - \sqrt{1 - 4\gamma}) \end{cases}, \quad (\text{A.64})$$

1734 considering that $0 < \gamma < 1/4$ in this zone. Again, one obtains

$$E(k) \approx -\frac{4m_0(k)}{\sqrt{1-4\gamma}} \sinh(u\sqrt{1-4\gamma}L) e^{-uL}. \quad (\text{A.65})$$

1735 Since $\sin(ix) = i \sinh(x)$, and by $\gamma = m_0(k)t_\perp/\lambda_\perp^2$, we may set $\gamma(k_c) = 0$ and obtain a
1736 unified expression for lowest order mass correction

$$E(k < k_c) = -\frac{4m_0(k)}{\sqrt{4\gamma-1}} \sin(u\sqrt{4\gamma-1}L) e^{-uL}. \quad (\text{A.66})$$

1737 However, as a comment, in numerical calculation, E in zone $0 < \gamma < 1/4$ is suppressed into
1738 zero in a much slower manner, which is caused by exponential cancellation between **sinh**
1739 and **exp**. Nevertheless, since $\sqrt{1-4\gamma} < 1$ in the region, we conclude that the exponential
1740 increasing is always slower than the decaying, which finally pushes the state to zero energy
1741 for $L \rightarrow +\infty$.

1742 B Derivation of Eq. (1b)

1743 To obtain an effective model, we start from solving \mathcal{H}_{1d} and notice that $[\mathcal{H}_{1d}(\mathbf{k}), \sigma_z] = 0$,
1744 from which we could let

$$\mathcal{H}_{1d}(\mathbf{k})\zeta_s \otimes |\phi^s(\mathbf{k})\rangle = \zeta_s \otimes \mathcal{H}_{1d}^s(\mathbf{k})|\phi^s(\mathbf{k})\rangle, \quad (\text{B.1})$$

1745 where $\mathcal{H}_{1d}^s(\mathbf{k})$ is split Hamiltonian that only acts on one subspace, and by definition

$$\sigma_z \zeta_s = s \zeta_s, \quad s = \pm. \quad (\text{B.2})$$

1746 Under basis of $\{\Psi_{l_z, k}\}_{l_z}$, $\mathcal{H}_{1d}^s(\mathbf{k})$ is in its matrix form denoted as $H_{1d}^s(\mathbf{k})$, with solution
1747 defined from its eigenvalue equation

$$H_{1d}^s(\mathbf{k})\phi^s(\mathbf{k}) = E^s(\mathbf{k})\phi^s(\mathbf{k}), \quad \phi^s(\mathbf{k}) = \oplus_{l_z} \phi_{l_z}^s(\mathbf{k}). \quad (\text{B.3})$$

1748 To make discussion pithy, we shall omit s, \mathbf{k} and let $M \equiv M_0(\mathbf{k})$ below in the section.

1749 Eq. (B.3) can be written in the recurrence form as

$$(t_\perp \tau_z + i \frac{\lambda_\perp}{2} s \tau_x) \phi_{l_z-1} + M \tau_z \phi_{l_z} + (t_\perp \tau_z - i \frac{\lambda_\perp}{2} s \tau_x) \phi_{l_z+1} = E \phi_{l_z}, \quad (\text{B.4})$$

1750 by observing which could we set trial function as $\phi_{l_z} = e^{i\xi l_z} \phi = \beta^{l_z} \phi$ where $\beta = e^{i\xi}$.
1751 Then accordingly the equation is reduced to

$$[(t_\perp \tau_z + i \frac{\lambda_\perp}{2} s \tau_x) \beta^{-1} + (M \tau_z - E) + (t_\perp \tau_z - i \frac{\lambda_\perp}{2} s \tau_x) \beta] \phi = 0, \quad (\text{B.5})$$

1752 which firstly leads to

$$E^2 = (M + 2t_\perp \cos \xi)^2 + \lambda_\perp^2 \sin^2 \xi, \quad (\text{B.6})$$

1753 requiring non-trivial ϕ . From Eq. (B.6) one solves

$$\begin{cases} \cos \xi_\alpha^p = \frac{-Mt_\perp + (-1)^{\alpha-1} \sqrt{M^2 t_\perp^2 - (t_\perp^2 - \lambda_\perp^2/4)(M^2 + \lambda_\perp^2 - E^2)}}{2(t_\perp^2 - \lambda_\perp^2/4)}, \\ \sin \xi_\alpha^p = p \sqrt{1 - \cos^2 \xi_\alpha}, \quad p = \pm, \alpha = 1, 2, \end{cases} \quad (\text{B.7})$$

1754 which tells that

$$\beta_\alpha^p = e^{i\xi_\alpha^p} = \cos \xi_\alpha + ip \sqrt{1 - \cos^2 \xi_\alpha}. \quad (\text{B.8})$$

1755 Here one thing to notice is that the sign change of $\sin \xi_\alpha^p$ is caused by sign change of ξ ,
1756 rather than a phase shift like $\xi \rightarrow \xi + \pi$, since the latter will lead to the sign change of
1757 $\cos \xi$, too, and that is not our solution.

1758 To make maximum utilization of the symmetry, we consider canonical boundary con-
1759 dition in which the centre of 1-d chain sits at $\mathbf{z} = \mathbf{0}$, then by denoting $l = L_z + 1$, we would
1760 have

$$\phi^s(\pm \frac{l}{2}) = 0, \quad (\text{B.9})$$

1761 and it is essential to notice that sites $l_z = \pm \frac{L_z + 1}{2}$ are two fictitious points where the
1762 constraints take place, and true lattice stops at $l_z = \pm \frac{L_z - 1}{2}$ as we only have L_z sites.
1763 What is more, for compensation of unifying expression regardless of oddity of L_z , l_z
1764 would be forced to choose different ways to be taken out as follows

$$\begin{cases} l_z = 0, \pm 1, \pm 2, \dots, \pm \frac{L_z + 1}{2}, & \text{for } L_z \text{ odd,} \\ l_z = \pm \frac{1}{2}, \pm \frac{3}{2}, \dots, \pm \frac{L_z + 1}{2}, & \text{for } L_z \text{ even,} \end{cases} \quad (\text{B.10})$$

1765 which conforms mirror symmetry to $\mathbf{z} = \mathbf{0}$. Afterwards, enlightened by the idea of sym-
1766 metric trial functions, we also build several functions from β_α^p considering the symmetric
1767 case stated above. Denote

$$\begin{cases} E(\beta, l_z) = \frac{\beta^{l_z} + \beta^{-l_z}}{\beta^{(L_z+1)/2} + \beta^{-(L_z+1)/2}} = \frac{\cos(\xi l_z)}{\cos(\xi l/2)} \\ O(\beta, l_z) = \frac{\beta^{l_z} - \beta^{-l_z}}{\beta^{(L_z+1)/2} - \beta^{-(L_z+1)/2}} = \frac{\sin(\xi l_z)}{\sin(\xi l/2)} \end{cases}, \quad (\text{B.11})$$

1768 where ‘ E ’ and ‘ O ’, namely even and odd, represent the parity of two functions about \mathbf{z} ,
1769 and one should not identify E here as the energy function. From which we establish two
1770 sets of factors respecting boundary condition with even or odd parity

$$\begin{cases} f_+(l_z) = \sum_\alpha (-1)^{\alpha-1} E(\beta_\alpha^p, l_z) \\ f_-(l_z) = \sum_\alpha (-1)^{\alpha-1} O(\beta_\alpha^p, l_z) \end{cases}, \quad (\text{B.12})$$

1771 where the summation is over α but without p since it only changes sign of ξ and thus does
1772 not influence the value of E or O . Before proceeding, let us find some special properties
1773 about those functions or factors. Let

$$\begin{cases} a = \beta + \frac{1}{\beta} = 2 \cos \xi \\ b = \beta - \frac{1}{\beta} = 2i \sin \xi \end{cases}, \quad (\text{B.13})$$

1774 who weight as the *lattice differential operators* that lead to relation

$$f_+(l_z \pm 1) = \sum_\alpha (-1)^{\alpha-1} \frac{a_\alpha E(\beta_\alpha, l_z) \pm i b_\alpha \tan(\xi_\alpha l/2) O(\beta_\alpha, l_z)}{2} \equiv g_\pm, \quad (\text{B.14a})$$

$$f_-(l_z \pm 1) = \sum_\alpha (-1)^{\alpha-1} \frac{a_\alpha O(\beta_\alpha, l_z) \mp i b_\alpha \cot(\xi_\alpha l/2) E(\beta_\alpha, l_z)}{2} \equiv h_\pm. \quad (\text{B.14b})$$

1775 One could again see that the iteration relation is also independent of \mathbf{p} within our expecta-
1776 tion.

1777 Now we are able to come back and solve the chain problem. Let

$$\phi_{l_z} = c f_+(l_z) + d f_-(l_z), \quad (\text{B.15})$$

1778 to be guessed general solution confined by boundary condition. Bring this trial solution
1779 into Eq. (B.4) and requiring vanishing coefficients of $E(\beta_\alpha, l_z)$ and $O(\beta_\alpha, l_z)$, one obtains,
1780 after re-organization,

$$\begin{cases} (M - E + t_\perp a_\alpha) c_1 - \frac{\lambda_\perp}{2} s d_2 b_\alpha \cot(\xi_\alpha l/2) = 0 \\ -\frac{\lambda_\perp}{2} s c_1 b_\alpha \tan(\xi_\alpha l/2) + (M + E + t_\perp a_\alpha) d_2 = 0 \end{cases}, \quad (\text{B.16a})$$

$$\begin{cases} (M - E + t_\perp a_\alpha) d_1 + \frac{\lambda_\perp}{2} s c_2 b_\alpha \tan(\xi_\alpha l/2) = 0 \\ \frac{\lambda_\perp}{2} s d_1 b_\alpha \cot(\xi_\alpha l/2) + (M + E + t_\perp a_\alpha) c_2 = 0 \end{cases}, \quad (\text{B.16b})$$

1781 for different α . Requiring simultaneous standing with respect to α leads to four solutions
1782 in pairs

$$\begin{cases} d_2 = \frac{i t_\perp \eta_1}{s \lambda_\perp} c_1, E = E_+ \\ c_1 = \frac{i t_\perp \eta_2}{s \lambda_\perp} d_2, E = -E_- \end{cases}, \quad \begin{cases} c_2 = -\frac{i t_\perp \eta_2}{s \lambda_\perp} d_1, E = E_- \\ d_1 = -\frac{i t_\perp \eta_1}{s \lambda_\perp} c_2, E = -E_+ \end{cases}, \quad (\text{B.17})$$

1783 where the formal expression for energies are

$$E_\pm = M + 2t_\perp \frac{\cos \xi_1 g^\pm(\xi_1) - \cos \xi_2 g^\pm(\xi_2)}{g^\pm(\xi_1) - g^\pm(\xi_2)}, \quad (\text{B.18})$$

1784 with two defined functions

$$g^\pm(\xi) = \frac{\tan^{\pm 1}(\xi(L_z + 1)/2)}{\sin \xi} \quad (\text{B.19})$$

1785 and two dimensionless factors

$$\begin{cases} \eta_1 = \frac{-2(\cos \xi_1 - \cos \xi_2)}{\sin \xi_1 \cot(\xi_1 l/2) - \sin \xi_2 \cot(\xi_2 l/2)}, \\ \eta_2 = \frac{-2(\cos \xi_1 - \cos \xi_2)}{\sin \xi_1 \tan(\xi_1 l/2) - \sin \xi_2 \tan(\xi_2 l/2)}, \end{cases} \quad (\text{B.20})$$

1786 have been introduced. From the above discussion we seemingly have four solutions, math-
1787 ematical restriction, however, tells that equations in Eq. (B.16) in the same brace must
1788 stand simultaneously, which then gives us two relations as

$$\begin{cases} 1 = \left| \frac{i t_\perp \eta_1}{s \lambda_\perp} \cdot \frac{i t_\perp \eta_2}{s \lambda_\perp} \right| \implies |\eta_1 \eta_2| = \frac{\lambda_\perp^2}{t_\perp^2}, \\ m \equiv E_+ = -E_-, \end{cases} \quad (\text{B.21})$$

1789 and the latter one is also a physical result from Dirac equation. This reduces our four so-
1790 lutions to two independent ones for each \mathbf{s} . The above discussion is equivalent to requiring
1791 simultaneous standing of equations in left brace of Eq. (B.16)

$$E^2 = (M + 2t_\perp \cos \xi_\alpha)^2 + \lambda_\perp^2 \sin^2 \xi_\alpha,$$

1792 which is independent of α and matches the result of Eq. (B.6).

1793 Similar arguments can be made here as in the continuum model. Counting on complex-
1794 ity of $\xi_{1,2}$ restricted by Eq. (B.7) and the property of trigonometric/hyperbolic function
1795 leads to the conclusion that quadratic form $f_+^* f_-$ and η (at certain $(\mathbf{k}, \mathbf{z}, E)$) are always
1796 real. Essentially, f_{\pm} are either real or purely imaginary.

1797 In short, what we need solving to get all energy states \mathbf{m} are the simultaneous equations
1798 below

$$\mathbf{m} = M + 2t_{\perp} \frac{\cos \xi_1 g(\xi_1) - \cos \xi_2 g(\xi_2)}{g(\xi_1) - g(\xi_2)}, \quad (\text{B.22a})$$

$$\cos \xi_{\alpha} = \frac{-Mt_{\perp} + (-1)^{\alpha-1} \sqrt{M^2 t_{\perp}^2 - (t_{\perp}^2 - \lambda_{\perp}^2/4)(M^2 + \lambda_{\perp}^2 - m^2)}}{2(t_{\perp}^2 - \lambda_{\perp}^2/4)}, \quad (\text{B.22b})$$

1799 where

$$\begin{cases} M = M_0(\mathbf{k}) = m_0 - 4t_{\parallel} \left(\sin^2 \frac{k_x a}{2} + \sin^2 \frac{k_y b}{2} \right) - 2t_{\perp}, \\ g(\xi) = \frac{\tan(\xi(L_z + 1))/2}{\sin \xi}, \end{cases} \quad (\text{B.23})$$

1800 and sign of ξ is fixed by $\mathbf{p} = +$ so that

$$\sin \xi_{\alpha} = \sqrt{1 - \cos^2 \xi_{\alpha}}, \quad \alpha = 1, 2. \quad (\text{B.24})$$

1801 Basically, there are three variables ξ_1, ξ_2 and \mathbf{m} , together with three equations above, then
1802 it is in a sense some *exact system of equations* but a non-linear transcendental version.
1803 From this set of equations, one may expect L_z solutions $\mathbf{m}_n(\mathbf{k}), n = 1, 2, \dots, L_z$ including
1804 one surface state and $L_z - 1$ purely trivial bulk states, if within suitable choice of parame-
1805 ters. And the other set of L_z solutions are just chiral partners with $-\mathbf{m}_n(\mathbf{k})$. Notice that
1806 these $2L_z$ solutions compose eigenvalues for one H_{1d}^s , then by counting $s = \pm$ there are in
1807 fact $4L_z$ solutions in total, which is expected from the matrix form of H_{1d} .

1808 Here it comes to construct basis for projection, we firstly ignore lower index for \mathbf{m}
1809 since our wavefunction solution form is universal whatever \mathbf{n} takes. Then by counting \mathbf{s} ,
1810 we totally have four independent solutions for each \mathbf{m} as follows

$$\begin{cases} \varphi(\mathbf{s}) = \begin{pmatrix} c_1 f_+ \\ d_2 f_- \end{pmatrix} = C \begin{pmatrix} -is \lambda_{\perp} f_+ \\ t_{\perp} \eta f_- \end{pmatrix}, E = m \\ \chi(\mathbf{s}) = \begin{pmatrix} d_1 f_- \\ c_2 f_+ \end{pmatrix} = C \begin{pmatrix} t_{\perp} \eta f_- \\ is \lambda_{\perp} f_+ \end{pmatrix}, E = -m \end{cases}, \quad (\text{B.25})$$

1811 where we have ignored lower index of η_1 , and the norm C is the same for φ and χ states.
1812 Then restoring \mathbf{n} -indices we have $4L_z$ basis in certain sequence as

$$\begin{aligned} \Phi_1^n &= \zeta_+ \otimes \varphi(+) = \begin{pmatrix} \varphi^n(+) \\ 0 \end{pmatrix}, \quad \Phi_2^n = \begin{pmatrix} 0 \\ \chi^n(-) \end{pmatrix}, \\ \Phi_3^n &= \begin{pmatrix} \chi^n(+) \\ 0 \end{pmatrix}, \quad \Phi_4^n = \begin{pmatrix} 0 \\ \varphi^n(-) \end{pmatrix}, \end{aligned} \quad (\text{B.26})$$

1813 with energies $(\mathbf{m}_n(\mathbf{k}), -\mathbf{m}_n(\mathbf{k}), -\mathbf{m}_n(\mathbf{k}), \mathbf{m}_n(\mathbf{k}))$, respectively. The (\mathbf{k}, l_z) dependence of
1814 these basis states are inherited from functions $f_{\pm}^n(\mathbf{k}, l_z)$ and factor $\eta^n(\mathbf{k})$.

1815 The basis here shares the same symmetry analysis as within the continuum model,
 1816 while here the parity and mirror symmetries can be written down explicitly in the off-
 1817 diagonal matrix form, with $\sigma_0 \tau_z$ and $-i \sigma_z \tau_z$ as the off-diagonal elements, respectively.
 1818 And especially, by combining the mirror and spin- \mathbf{z} index, we assign $\Phi_i^n = \Phi_{\chi,s}^n$ with

$$\begin{aligned} \Phi_{++}^n &= \Phi_1^n, & \Phi_{+-}^n &= \Phi_2^n, \\ \Phi_{-+}^n &= \Phi_3^n, & \Phi_{--}^n &= \Phi_4^n. \end{aligned} \quad (\text{B.27})$$

1819 Now we turn to the projection, which is formally

$$\langle \Phi | H_{\text{Film}} | \Phi \rangle = \langle \Phi | H_{1d} | \Phi \rangle + \langle \Phi | H_{\parallel} | \Phi \rangle, \quad (\text{B.28})$$

1820 where the first part, by the definition of eigenvalue equation, is just $\oplus_n \text{diag}(m_n, -m_n, -m_n, m_n) = \oplus_n m_n(k) \tau_z$
 1821 while in the second part, since $H_{\parallel} = \lambda_{\parallel} (\sin(k_x a) \sigma_x \tau_x + \sin(k_y b) \sigma_y \tau_x)$ is purely off diag-
 1822 onal, it is easy to conclude that

$$\begin{aligned} \langle \Phi_i^n | H_{\parallel} | \Phi_i^{n'} \rangle &= 0, \quad i = 1, 2, 3, 4, \\ \langle \Phi_1^n | H_{\parallel} | \Phi_3^{n'} \rangle &= 0 = \langle \Phi_2^n | H_{\parallel} | \Phi_4^{n'} \rangle. \end{aligned}$$

1823 Then only four terms need consideration by hermicity, among which

$$\begin{aligned} \langle \Phi_1^n | H_{\parallel} | \Phi_4^{n'} \rangle &= \lambda_{\parallel} (\sin(k_x a) - i \sin(k_y b)) \sum_{l_z} |C|^2 i \lambda_{\perp} t_{\perp} [\eta^n (f_+^n)^* f_-^{n'} + \eta^{n'} (f_-^n)^* f_+^{n'}] = 0, \\ \langle \Phi_2^n | H_{\parallel} | \Phi_3^{n'} \rangle &= \lambda_{\parallel} (\sin(k_x a) - i \sin(k_y b)) \sum_{l_z} |C|^2 i \lambda_{\perp} t_{\perp} [\eta^n (f_-^n)^* f_+^{n'} + \eta^{n'} (f_+^n)^* f_-^{n'}] = 0, \end{aligned}$$

1824 as $f_- f_+$ is odd to \mathbf{z} . Then, the only remaining terms are

$$\langle \Phi_1^n | H_{\parallel} | \Phi_2^{n'} \rangle = \lambda_{\parallel} (\sin(k_x a) - i \sin(k_y b)) \delta_{nn'} = \langle \Phi_3^n | H_{\parallel} | \Phi_4^{n'} \rangle,$$

1825 where normalization condition is used. Finally we arrive at the equivalent Hamiltonian

$$H(\mathbf{k}) = \bigoplus_{n=1}^{L_z} [\lambda_{\parallel} (\sin(k_x a) \sigma_x + \sin(k_y b) \sigma_y) + m_n(k) \tau_z \sigma_z] = \bigoplus_{n,\chi} h_{n,\chi}(\mathbf{k}), \quad (\text{B.29})$$

1826 where unspecified degrees of freedom are all identity matrix. And hereto we have suc-
 1827 cessfully arrived at Eq. (1b) in the main text. Also notice that H is exactly equivalent
 1828 to original H_{Film} , since by counting all \mathbf{n} , the projection we did is just a unitary basis
 1829 transformation, where the unitary matrix is composed of solutions of H_{1d} .

1830 The projection here is also a unitary transformation, which shares a simpler form than
 1831 that in the continuum model. Since now the original Hamiltonian reads

$$\mathcal{H}_{\text{Film}}(\mathbf{k}) = \sum_{l_z, l'_z} \Psi_{l_z}^{\dagger} H_{\text{Film}}(\mathbf{k}, l_z, l'_z) \Psi_{l'_z}, \quad (\text{B.30})$$

1832 then by defining $\Psi = \oplus_{l_z} \Psi_{l_z}$, we identify the unitary transformation as

$$\mathcal{H}_{\text{Film}}(\mathbf{k}) = (\Psi^{\dagger} U^L) [(U^L)^{\dagger} H_{\text{Film}}(\mathbf{k}) U^L] ((U^L)^{\dagger} \Psi), \quad (\text{B.31})$$

1833 where

$$U^L = (\Phi^1, \Phi^2, \dots, \Phi^{L_z}), \quad \Phi^n = (\Phi_1^n, \Phi_2^n, \Phi_3^n, \Phi_4^n), \quad (\text{B.32})$$

1834 and we recognize $\Phi_i^n = \oplus_{l_z} \Phi_i^n(l_z)$ here so that U^l is a $4L_z \times 4L_z$ unitary matrix. And here
 1835 again U^l is trivial in \mathbf{k} -space. The core transformation on matrix form of Hamiltonian
 1836 gives rise to

$$H(\mathbf{k}) = (U^l(\mathbf{k}))^\dagger H_{\text{Film}}(\mathbf{k}) U^l(\mathbf{k}), \quad (\text{B.33})$$

1837 while the inverse transformation $(U^l)^\dagger \Psi$ assigns composed Fermionic operators to the new
 1838 basis. Essentially, the transformation to each $h_{n,\chi}$ is done by

$$h_{n,\chi} = (U_{n,\chi}^l)^\dagger H_{\text{Film}} U_{n,\chi}^l, \quad (\text{B.34})$$

1839 where

$$U_{n,\chi}^l = \Phi_\chi^n = (\Phi_{\chi,s=+}^n, \Phi_{\chi,s=-}^n), \quad (\text{B.35})$$

1840 is a $2L_z \times 2$ matrix.

1841 References

- 1842 [1] A. Altland and M. R. Zirnbauer, *Nonstandard symmetry classes in meso-*
 1843 *scopic normal-superconducting hybrid structures*, Phys. Rev. B **55**, 1142 (1997),
 1844 doi:[10.1103/PhysRevB.55.1142](https://doi.org/10.1103/PhysRevB.55.1142).
- 1845 [2] S. Ryu, A. P. Schnyder, A. Furusaki and A. W. W. Ludwig, *Topological insulators*
 1846 *and superconductors: tenfold way and dimensional hierarchy*, New J. Phys. **12**(6),
 1847 065010 (2010), doi:[10.1088/1367-2630/12/6/065010](https://doi.org/10.1088/1367-2630/12/6/065010).
- 1848 [3] C.-K. Chiu, J. C. Y. Teo, A. P. Schnyder and S. Ryu, *Classification of topo-*
 1849 *logical quantum matter with symmetries*, Rev. Mod. Phys. **88**, 035005 (2016),
 1850 doi:[10.1103/RevModPhys.88.035005](https://doi.org/10.1103/RevModPhys.88.035005).
- 1851 [4] B. Fu, J.-Y. Zou, Z.-A. Hu, H.-W. Wang and S.-Q. Shen, *Quantum anomalous*
 1852 *semimetals*, npj Quantum Mater. **7**(1), 94 (2022), doi:[10.1038/s41535-022-00503-0](https://doi.org/10.1038/s41535-022-00503-0).
- 1853 [5] S. D. Sarma, M. Freedman and C. Nayak, *Majorana zero modes and topological quan-*
 1854 *tum computation*, npj Quantum Inf. **1**(1), 15001 (2015), doi:[10.1038/npjqi.2015.1](https://doi.org/10.1038/npjqi.2015.1).
- 1855 [6] A. Soumyanarayanan, N. Reyren, A. Fert and C. Panagopoulos, *Emergent phenom-*
 1856 *ena induced by spin-orbit coupling at surfaces and interfaces*, Nature **539**(7630), 509
 1857 (2016), doi:[10.1038/nature19820](https://doi.org/10.1038/nature19820).
- 1858 [7] J. Junquera, Y. Nahas, S. Prokhorenko, L. Bellaiche, J. Íñiguez, D. G. Schlom,
 1859 L.-Q. Chen, S. Salahuddin, D. A. Muller, L. W. Martin and R. Ramesh, *Topo-*
 1860 *logical phases in polar oxide nanostructures*, Rev. Mod. Phys. **95**, 025001 (2023),
 1861 doi:[10.1103/RevModPhys.95.025001](https://doi.org/10.1103/RevModPhys.95.025001).
- 1862 [8] L. D. Landau and E. M. Lifshitz, *Statistical Physics: Volume 5*, vol. 5, Elsevier
 1863 (2013).
- 1864 [9] P. W. Anderson, *Basic notions of condensed matter physics*, CRC Press (2018).
- 1865 [10] D. J. Thouless, M. Kohmoto, M. P. Nightingale and M. den Nijs, *Quantized hall*
 1866 *conductance in a two-dimensional periodic potential*, Phys. Rev. Lett. **49**, 405 (1982),
 1867 doi:[10.1103/PhysRevLett.49.405](https://doi.org/10.1103/PhysRevLett.49.405).

- 1868 [11] X.-G. Wen, *Topological orders and edge excitations in fractional quantum hall states*,
1869 Adv. Phys. **44**(5), 405 (1995), doi:[10.1080/00018739500101566](https://doi.org/10.1080/00018739500101566), [https://doi.org/10.](https://doi.org/10.1080/00018739500101566)
1870 [1080/00018739500101566](https://doi.org/10.1080/00018739500101566).
- 1871 [12] C. L. Kane and E. J. Mele, *Z_2 topological order and the quantum spin hall effect*,
1872 Phys. Rev. Lett. **95**, 146802 (2005), doi:[10.1103/PhysRevLett.95.146802](https://doi.org/10.1103/PhysRevLett.95.146802).
- 1873 [13] M. Z. Hasan and C. L. Kane, *Colloquium: Topological insulators*, Rev. Mod. Phys.
1874 **82**, 3045 (2010), doi:[10.1103/RevModPhys.82.3045](https://doi.org/10.1103/RevModPhys.82.3045).
- 1875 [14] X.-L. Qi and S.-C. Zhang, *Topological insulators and superconductors*, Rev. Mod.
1876 Phys. **83**, 1057 (2011), doi:[10.1103/RevModPhys.83.1057](https://doi.org/10.1103/RevModPhys.83.1057).
- 1877 [15] A. Bansil, H. Lin and T. Das, *Colloquium: Topological band theory*, Rev. Mod.
1878 Phys. **88**, 021004 (2016), doi:[10.1103/RevModPhys.88.021004](https://doi.org/10.1103/RevModPhys.88.021004).
- 1879 [16] Y. Tokura, K. Yasuda and A. Tsukazaki, *Magnetic topological insulators*, Nat. Rev.
1880 Phys. **1**(2), 126 (2019), doi:[10.1038/s42254-018-0011-5](https://doi.org/10.1038/s42254-018-0011-5).
- 1881 [17] L. Fu, C. L. Kane and E. J. Mele, *Topological insulators in three dimensions*, Phys.
1882 Rev. Lett. **98**, 106803 (2007), doi:[10.1103/PhysRevLett.98.106803](https://doi.org/10.1103/PhysRevLett.98.106803).
- 1883 [18] J. E. Moore and L. Balents, *Topological invariants of time-reversal-invariant band*
1884 *structures*, Phys. Rev. B **75**, 121306 (2007), doi:[10.1103/PhysRevB.75.121306](https://doi.org/10.1103/PhysRevB.75.121306).
- 1885 [19] R. Roy, *Topological phases and the quantum spin hall effect in three dimensions*,
1886 Phys. Rev. B **79**, 195322 (2009), doi:[10.1103/PhysRevB.79.195322](https://doi.org/10.1103/PhysRevB.79.195322).
- 1887 [20] D. Hsieh, D. Qian, L. Wray, Y. Xia, Y. S. Hor, R. J. Cava and M. Z. Hasan, *A*
1888 *topological dirac insulator in a quantum spin hall phase*, Nature **452**(7190), 970
1889 (2008), doi:[10.1038/nature06843](https://doi.org/10.1038/nature06843).
- 1890 [21] Y. Xia, D. Qian, D. Hsieh, L. Wray, A. Pal, H. Lin, A. Bansil, D. Grauer,
1891 Y. S. Hor, R. J. Cava and M. Z. Hasan, *Observation of a large-gap topological-*
1892 *insulator class with a single dirac cone on the surface*, Nat. Phys. **5**(6), 398 (2009),
1893 doi:[10.1038/nphys1274](https://doi.org/10.1038/nphys1274).
- 1894 [22] D. Hsieh, Y. Xia, D. Qian, L. Wray, F. Meier, J. H. Dil, J. Osterwalder, L. Patthey,
1895 A. V. Fedorov, H. Lin, A. Bansil, D. Grauer *et al.*, *Observation of time-reversal-*
1896 *protected single-dirac-cone topological-insulator states in Bi_2Te_3 and Sb_2Te_3* , Phys.
1897 Rev. Lett. **103**, 146401 (2009), doi:[10.1103/PhysRevLett.103.146401](https://doi.org/10.1103/PhysRevLett.103.146401).
- 1898 [23] Y. L. Chen, J. G. Analytis, J.-H. Chu, Z. K. Liu, S.-K. Mo, X. L. Qi, H. J. Zhang,
1899 D. H. Lu, X. Dai, Z. Fang, S. C. Zhang, I. R. Fisher *et al.*, *Experimental realiza-*
1900 *tion of a three-dimensional topological insulator, Bi_2Te_3* , Science **325**(5937), 178
1901 (2009), doi:[10.1126/science.1173034](https://doi.org/10.1126/science.1173034), [https://www.science.org/doi/pdf/10.1126/](https://www.science.org/doi/pdf/10.1126/science.1173034)
1902 [science.1173034](https://www.science.org/doi/pdf/10.1126/science.1173034).
- 1903 [24] B. I. Halperin, *Quantized hall conductance, current-carrying edge states, and the*
1904 *existence of extended states in a two-dimensional disordered potential*, Phys. Rev. B
1905 **25**, 2185 (1982), doi:[10.1103/PhysRevB.25.2185](https://doi.org/10.1103/PhysRevB.25.2185).
- 1906 [25] Y. Hatsugai, *Chern number and edge states in the integer quantum hall effect*, Phys.
1907 Rev. Lett. **71**, 3697 (1993), doi:[10.1103/PhysRevLett.71.3697](https://doi.org/10.1103/PhysRevLett.71.3697).

- 1908 [26] Y. Hatsugai, *Edge states in the integer quantum hall effect and the riemann surface of*
1909 *the bloch function*, Phys. Rev. B **48**, 11851 (1993), doi:[10.1103/PhysRevB.48.11851](https://doi.org/10.1103/PhysRevB.48.11851).
- 1910 [27] S.-Q. Shen, *Starting from the Dirac Equation*, pp. 17–32, Springer Singapore,
1911 Singapore, ISBN 978-981-10-4606-3, doi:[10.1007/978-981-10-4606-3_2](https://doi.org/10.1007/978-981-10-4606-3_2) (2017).
- 1912 [28] L. Šmejkal, Y. Mokrousov, B. Yan and A. H. MacDonald, *Topological antiferromag-*
1913 *netic spintronics*, Nat. Phys. **14**(3), 242 (2018), doi:[10.1038/s41567-018-0064-5](https://doi.org/10.1038/s41567-018-0064-5).
- 1914 [29] H. Nielsen and M. Ninomiya, *Absence of neutrinos on a lattice: (i). proof by*
1915 *homotopy theory*, Nucl. Phys. B **185**(1), 20 (1981), doi:[https://doi.org/10.1016/0550-](https://doi.org/10.1016/0550-3213(81)90361-8)
1916 [3213\(81\)90361-8](https://doi.org/10.1016/0550-3213(81)90361-8).
- 1917 [30] H. Nielsen and M. Ninomiya, *Absence of neutrinos on a lattice: (ii). intuitive topo-*
1918 *logical proof*, Nucl. Phys. B **193**(1), 173 (1981), doi:[https://doi.org/10.1016/0550-](https://doi.org/10.1016/0550-3213(81)90524-1)
1919 [3213\(81\)90524-1](https://doi.org/10.1016/0550-3213(81)90524-1).
- 1920 [31] J.-Y. Zou, R. Chen, B. Fu, H.-W. Wang, Z.-A. Hu and S.-Q. Shen, *Half-quantized*
1921 *hall effect at the parity-invariant fermi surface*, Phys. Rev. B **107**, 125153 (2023),
1922 doi:[10.1103/PhysRevB.107.125153](https://doi.org/10.1103/PhysRevB.107.125153).
- 1923 [32] K.-Z. Bai, B. Fu, Z. Zhang and S.-Q. Shen, *Metallic quantized anomalous*
1924 *hall effect without chiral edge states*, Phys. Rev. B **108**, L241407 (2023),
1925 doi:[10.1103/PhysRevB.108.L241407](https://doi.org/10.1103/PhysRevB.108.L241407).
- 1926 [33] B. Fu, K.-Z. Bai and S.-Q. Shen, *Half quantum mirror hall effect* (2024), [2402.02654](https://arxiv.org/abs/2402.02654).
- 1927 [34] K. G. Wilson, *Confinement of quarks*, Phys. Rev. D **10**, 2445 (1974),
1928 doi:[10.1103/PhysRevD.10.2445](https://doi.org/10.1103/PhysRevD.10.2445).
- 1929 [35] S. D. Drell, M. Weinstein and S. Yankielowicz, *Strong-coupling field theories.*
1930 *ii. fermions and gauge fields on a lattice*, Phys. Rev. D **14**, 1627 (1976),
1931 doi:[10.1103/PhysRevD.14.1627](https://doi.org/10.1103/PhysRevD.14.1627).
- 1932 [36] B. Zhou, H.-Z. Lu, R.-L. Chu, S.-Q. Shen and Q. Niu, *Finite size effects on helical*
1933 *edge states in a quantum spin-hall system*, Phys. Rev. Lett. **101**, 246807 (2008),
1934 doi:[10.1103/PhysRevLett.101.246807](https://doi.org/10.1103/PhysRevLett.101.246807).
- 1935 [37] H.-Z. Lu, W.-Y. Shan, W. Yao, Q. Niu and S.-Q. Shen, *Massive dirac fermions and*
1936 *spin physics in an ultrathin film of topological insulator*, Phys. Rev. B **81**, 115407
1937 (2010), doi:[10.1103/PhysRevB.81.115407](https://doi.org/10.1103/PhysRevB.81.115407).
- 1938 [38] W.-Y. Shan, H.-Z. Lu and S.-Q. Shen, *Effective continuous model for surface states*
1939 *and thin films of three-dimensional topological insulators*, New J. Phys. **12**(4), 043048
1940 (2010), doi:[10.1088/1367-2630/12/4/043048](https://doi.org/10.1088/1367-2630/12/4/043048).
- 1941 [39] Y. Zhang, K. He, C.-Z. Chang, C.-L. Song, L.-L. Wang, X. Chen, J.-F. Jia, Z. Fang,
1942 X. Dai, W.-Y. Shan, S.-Q. Shen, Q. Niu *et al.*, *Crossover of the three-dimensional*
1943 *topological insulator Bi₂Se₃ to the two-dimensional limit*, Nat. Phys. **6**(8), 584 (2010),
1944 doi:[10.1038/nphys1689](https://doi.org/10.1038/nphys1689).
- 1945 [40] C.-X. Liu, H. Zhang, B. Yan, X.-L. Qi, T. Frauenheim, X. Dai, Z. Fang and S.-C.
1946 Zhang, *Oscillatory crossover from two-dimensional to three-dimensional topological*
1947 *insulators*, Phys. Rev. B **81**, 041307 (2010), doi:[10.1103/PhysRevB.81.041307](https://doi.org/10.1103/PhysRevB.81.041307).

- 1948 [41] S. K. Chong, L. Liu, K. Watanabe, T. Taniguchi, T. D. Sparks, F. Liu and V. V.
1949 Deshpande, *Emergent helical edge states in a hybridized three-dimensional topological*
1950 *insulator*, Nat. Commun. **13**(1), 6386 (2022), doi:[10.1038/s41467-022-33643-9](https://doi.org/10.1038/s41467-022-33643-9).
- 1951 [42] A. C. Lygo, B. Guo, A. Rashidi, V. Huang, P. Cuadros-Romero and S. Stemmer,
1952 *Two-dimensional topological insulator state in cadmium arsenide thin films*, Phys.
1953 Rev. Lett. **130**, 046201 (2023), doi:[10.1103/PhysRevLett.130.046201](https://doi.org/10.1103/PhysRevLett.130.046201).
- 1954 [43] D. N. Sheng, Z. Y. Weng, L. Sheng and F. D. M. Haldane, *Quantum spin-hall effect*
1955 *and topologically invariant chern numbers*, Phys. Rev. Lett. **97**, 036808 (2006),
1956 doi:[10.1103/PhysRevLett.97.036808](https://doi.org/10.1103/PhysRevLett.97.036808).
- 1957 [44] B. A. Bernevig, T. L. Hughes and S.-C. Zhang, *Quantum spin hall effect and*
1958 *topological phase transition in HgTe quantum wells*, Science **314**(5806), 1757
1959 (2006), doi:[10.1126/science.1133734](https://doi.org/10.1126/science.1133734), [https://www.science.org/doi/pdf/10.1126/](https://www.science.org/doi/pdf/10.1126/science.1133734)
1960 [science.1133734](https://www.science.org/doi/pdf/10.1126/science.1133734).
- 1961 [45] M. König, S. Wiedmann, C. Brüne, A. Roth, H. Buhmann, L. W. Molenkamp, X.-
1962 L. Qi and S.-C. Zhang, *Quantum spin hall insulator state in HgTe quantum wells*,
1963 Science **318**(5851), 766 (2007), doi:[10.1126/science.1148047](https://doi.org/10.1126/science.1148047), [https://www.science.](https://www.science.org/doi/pdf/10.1126/science.1148047)
1964 [org/doi/pdf/10.1126/science.1148047](https://www.science.org/doi/pdf/10.1126/science.1148047).
- 1965 [46] Y. L. Chen, J.-H. Chu, J. G. Analytis, Z. K. Liu, K. Igarashi, H.-H. Kuo, X. L.
1966 Qi, S. K. Mo, R. G. Moore, D. H. Lu, M. Hashimoto, T. Sasagawa *et al.*, *Massive*
1967 *dirac fermion on the surface of a magnetically doped topological insulator*, Science
1968 **329**(5992), 659 (2010), doi:[10.1126/science.1189924](https://doi.org/10.1126/science.1189924), [https://www.science.org/doi/](https://www.science.org/doi/pdf/10.1126/science.1189924)
1969 [pdf/10.1126/science.1189924](https://www.science.org/doi/pdf/10.1126/science.1189924).
- 1970 [47] F. D. M. Haldane, *Model for a quantum hall effect without landau levels: Condensed-*
1971 *matter realization of the "parity anomaly"*, Phys. Rev. Lett. **61**, 2015 (1988),
1972 doi:[10.1103/PhysRevLett.61.2015](https://doi.org/10.1103/PhysRevLett.61.2015).
- 1973 [48] R. Yu, W. Zhang, H.-J. Zhang, S.-C. Zhang, X. Dai and Z. Fang, *Quantized*
1974 *anomalous hall effect in magnetic topological insulators*, Science **329**(5987), 61
1975 (2010), doi:[10.1126/science.1187485](https://doi.org/10.1126/science.1187485), [https://www.science.org/doi/pdf/10.1126/](https://www.science.org/doi/pdf/10.1126/science.1187485)
1976 [science.1187485](https://www.science.org/doi/pdf/10.1126/science.1187485).
- 1977 [49] C.-Z. Chang, J. Zhang, X. Feng, J. Shen, Z. Zhang, M. Guo, K. Li, Y. Ou, P. Wei,
1978 L.-L. Wang, Z.-Q. Ji, Y. Feng *et al.*, *Experimental observation of the quantum*
1979 *anomalous hall effect in a magnetic topological insulator*, Science **340**(6129), 167
1980 (2013), doi:[10.1126/science.1234414](https://doi.org/10.1126/science.1234414), [https://www.science.org/doi/pdf/10.1126/](https://www.science.org/doi/pdf/10.1126/science.1234414)
1981 [science.1234414](https://www.science.org/doi/pdf/10.1126/science.1234414).
- 1982 [50] X.-L. Qi, T. L. Hughes and S.-C. Zhang, *Topological field theory*
1983 *of time-reversal invariant insulators*, Phys. Rev. B **78**, 195424 (2008),
1984 doi:[10.1103/PhysRevB.78.195424](https://doi.org/10.1103/PhysRevB.78.195424).
- 1985 [51] M. Mogi, M. Kawamura, R. Yoshimi, A. Tsukazaki, Y. Kozuka, N. Shirakawa, K. . S.
1986 Takahashi, M. Kawasaki and Y. Tokura, *A magnetic heterostructure of topological*
1987 *insulators as a candidate for an axion insulator*, Nat. Mater. **16**(5), 516 (2017),
1988 doi:[10.1038/nmat4855](https://doi.org/10.1038/nmat4855).
- 1989 [52] M. Mogi, Y. Okamura, M. Kawamura, R. Yoshimi, K. Yasuda, A. Tsukazaki, K. S.
1990 Takahashi, T. Morimoto, N. Nagaosa, M. Kawasaki, Y. Takahashi and Y. Tokura,

- 1991 *Experimental signature of the parity anomaly in a semi-magnetic topological insula-*
1992 *tor*, Nat. Phys. **18**(4), 390 (2022), doi:[10.1038/s41567-021-01490-y](https://doi.org/10.1038/s41567-021-01490-y).
- 1993 [53] J.-Y. Zou, B. Fu, H.-W. Wang, Z.-A. Hu and S.-Q. Shen, *Half-quantized hall effect*
1994 *and power law decay of edge-current distribution*, Phys. Rev. B **105**, L201106 (2022),
1995 doi:[10.1103/PhysRevB.105.L201106](https://doi.org/10.1103/PhysRevB.105.L201106).
- 1996 [54] H. Zhang, C.-X. Liu, X.-L. Qi, X. Dai, Z. Fang and S.-C. Zhang, *Topological insu-*
1997 *lators in Bi₂Se₃, Bi₂Te₃ and Sb₂Te₃ with a single dirac cone on the surface*, Nat.
1998 Phys. **5**(6), 438 (2009), doi:[10.1038/nphys1270](https://doi.org/10.1038/nphys1270).
- 1999 [55] M. E. Peskin, *An introduction to quantum field theory*, CRC press (2018).
- 2000 [56] H.-W. Wang, B. Fu and S.-Q. Shen, *Helical symmetry breaking and quan-*
2001 *tum anomaly in massive dirac fermions*, Phys. Rev. B **104**, L241111 (2021),
2002 doi:[10.1103/PhysRevB.104.L241111](https://doi.org/10.1103/PhysRevB.104.L241111).
- 2003 [57] H.-W. Wang, B. Fu, J.-Y. Zou, Z.-A. Hu and S.-Q. Shen, *Fractional electromagnetic*
2004 *response in a three-dimensional chiral anomalous semimetal*, Phys. Rev. B **106**,
2005 045111 (2022), doi:[10.1103/PhysRevB.106.045111](https://doi.org/10.1103/PhysRevB.106.045111).
- 2006 [58] K. O. Friedrichs, *The identity of weak and strong extensions of differential operators*,
2007 Trans. Am. Math. Soc. **55**(1), 132 (1944).
- 2008 [59] Z. Wang, H. Weng, Q. Wu, X. Dai and Z. Fang, *Three-dimensional dirac*
2009 *semimetal and quantum transport in Cd₃As₂*, Phys. Rev. B **88**, 125427 (2013),
2010 doi:[10.1103/PhysRevB.88.125427](https://doi.org/10.1103/PhysRevB.88.125427).
- 2011 [60] S.-B. Zhang, H.-Z. Lu and S.-Q. Shen, *Edge states and integer quantum hall effect in*
2012 *topological insulator thin films*, Sci. Rep. **5**(1), 13277 (2015), doi:[10.1038/srep13277](https://doi.org/10.1038/srep13277).
- 2013 [61] W. P. Su, J. R. Schrieffer and A. J. Heeger, *Solitons in polyacetylene*, Phys. Rev.
2014 Lett. **42**, 1698 (1979), doi:[10.1103/PhysRevLett.42.1698](https://doi.org/10.1103/PhysRevLett.42.1698).
- 2015 [62] W. P. Su, J. R. Schrieffer and A. J. Heeger, *Soliton excitations in polyacetylene*,
2016 Phys. Rev. B **22**, 2099 (1980), doi:[10.1103/PhysRevB.22.2099](https://doi.org/10.1103/PhysRevB.22.2099).
- 2017 [63] G. E. Volovik, *Topological Lifshitz transitions*, Low Temp. Phys. **43**(1), 47
2018 (2017), doi:[10.1063/1.4974185](https://doi.org/10.1063/1.4974185), https://pubs.aip.org/aip/ltp/article-pdf/43/1/47/15722194/47_1_online.pdf.
- 2020 [64] L. Fu and C. L. Kane, *Topological insulators with inversion symmetry*, Phys. Rev.
2021 B **76**, 045302 (2007), doi:[10.1103/PhysRevB.76.045302](https://doi.org/10.1103/PhysRevB.76.045302).
- 2022 [65] G. D. Mahan, *Nonzero Temperatures*, pp. 109–185, Springer US, Boston, MA, ISBN
2023 978-1-4757-5714-9, doi:[10.1007/978-1-4757-5714-9_3](https://doi.org/10.1007/978-1-4757-5714-9_3) (2000).
- 2024 [66] S. L. Adler, *Axial-vector vertex in spinor electrodynamics*, Phys. Rev. **177**, 2426
2025 (1969), doi:[10.1103/PhysRev.177.2426](https://doi.org/10.1103/PhysRev.177.2426).
- 2026 [67] E. Witten, *An su(2) anomaly*, Phys. Lett. B **117**(5), 324 (1982),
2027 doi:[https://doi.org/10.1016/0370-2693\(82\)90728-6](https://doi.org/10.1016/0370-2693(82)90728-6).
- 2028 [68] A. N. Redlich, *Parity violation and gauge noninvariance of the effective*
2029 *gauge field action in three dimensions*, Phys. Rev. D **29**, 2366 (1984),
2030 doi:[10.1103/PhysRevD.29.2366](https://doi.org/10.1103/PhysRevD.29.2366).

- 2031 [69] R. Jackiw, *Fractional charge and zero modes for planar systems in a magnetic field*,
2032 Phys. Rev. D **29**, 2375 (1984), doi:[10.1103/PhysRevD.29.2375](https://doi.org/10.1103/PhysRevD.29.2375).
- 2033 [70] G. W. Semenoff, *Condensed-matter simulation of a three-dimensional anomaly*,
2034 Phys. Rev. Lett. **53**, 2449 (1984), doi:[10.1103/PhysRevLett.53.2449](https://doi.org/10.1103/PhysRevLett.53.2449).
- 2035 [71] E. Fradkin, E. Dagotto and D. Boyanovsky, *Physical realization of the par-*
2036 *ity anomaly in condensed matter physics*, Phys. Rev. Lett. **57**, 2967 (1986),
2037 doi:[10.1103/PhysRevLett.57.2967](https://doi.org/10.1103/PhysRevLett.57.2967).
- 2038 [72] M. Nakahara, *Geometry, topology and physics*, CRC press (2018).
- 2039 [73] A. Bohm, A. Mostafazadeh, H. Koizumi, Q. Niu and J. Zwanziger, *Mathematical*
2040 *Structure of the Geometric Phase I: The Abelian Phase*, pp. 107–127, Springer
2041 Berlin Heidelberg, Berlin, Heidelberg, ISBN 978-3-662-10333-3, doi:[10.1007/978-3-](https://doi.org/10.1007/978-3-662-10333-3_6)
2042 [662-10333-3_6](https://doi.org/10.1007/978-3-662-10333-3_6) (2003).
- 2043 [74] T. T. Wu and C. N. Yang, *Concept of nonintegrable phase factors and global formu-*
2044 *lation of gauge fields*, Phys. Rev. D **12**, 3845 (1975), doi:[10.1103/PhysRevD.12.3845](https://doi.org/10.1103/PhysRevD.12.3845).
- 2045 [75] T. T. Wu and C. N. Yang, *Dirac's monopole without strings: Classical lagrangian*
2046 *theory*, Phys. Rev. D **14**, 437 (1976), doi:[10.1103/PhysRevD.14.437](https://doi.org/10.1103/PhysRevD.14.437).
- 2047 [76] M. V. Berry, *Quantal phase factors accompanying adiabatic changes*, Proc. R. Soc.
2048 Lond. A **392**(1802), 45 (1984).
- 2049 [77] F. D. M. Haldane, *Berry curvature on the fermi surface: Anomalous hall ef-*
2050 *fect as a topological fermi-liquid property*, Phys. Rev. Lett. **93**, 206602 (2004),
2051 doi:[10.1103/PhysRevLett.93.206602](https://doi.org/10.1103/PhysRevLett.93.206602).
- 2052 [78] X. Wang, D. Vanderbilt, J. R. Yates and I. Souza, *Fermi-surface calcula-*
2053 *tion of the anomalous hall conductivity*, Phys. Rev. B **76**, 195109 (2007),
2054 doi:[10.1103/PhysRevB.76.195109](https://doi.org/10.1103/PhysRevB.76.195109).
- 2055 [79] D. Xiao, M.-C. Chang and Q. Niu, *Berry phase effects on electronic properties*, Rev.
2056 Mod. Phys. **82**, 1959 (2010), doi:[10.1103/RevModPhys.82.1959](https://doi.org/10.1103/RevModPhys.82.1959).
- 2057 [80] Y. Chen, D. L. Bergman and A. A. Burkov, *Weyl fermions and the anoma-*
2058 *lous hall effect in metallic ferromagnets*, Phys. Rev. B **88**, 125110 (2013),
2059 doi:[10.1103/PhysRevB.88.125110](https://doi.org/10.1103/PhysRevB.88.125110).
- 2060 [81] C.-X. Liu, X.-L. Qi, X. Dai, Z. Fang and S.-C. Zhang, *Quantum anomalous*
2061 *hall effect in $\text{Hg}_{1-y}\text{Mn}_y\text{Te}$ quantum wells*, Phys. Rev. Lett. **101**, 146802 (2008),
2062 doi:[10.1103/PhysRevLett.101.146802](https://doi.org/10.1103/PhysRevLett.101.146802).
- 2063 [82] M. Creutz and I. Horváth, *Surface states and chiral symmetry on the lattice*, Phys.
2064 Rev. D **50**, 2297 (1994), doi:[10.1103/PhysRevD.50.2297](https://doi.org/10.1103/PhysRevD.50.2297).
- 2065 [83] J. Wang, B. Lian, H. Zhang, Y. Xu and S.-C. Zhang, *Quantum anoma-*
2066 *lous hall effect with higher plateaus*, Phys. Rev. Lett. **111**, 136801 (2013),
2067 doi:[10.1103/PhysRevLett.111.136801](https://doi.org/10.1103/PhysRevLett.111.136801).
- 2068 [84] B. A. Bernevig and S.-C. Zhang, *Quantum spin hall effect*, Phys. Rev. Lett. **96**,
2069 106802 (2006), doi:[10.1103/PhysRevLett.96.106802](https://doi.org/10.1103/PhysRevLett.96.106802).

- 2070 [85] I. Knez, R.-R. Du and G. Sullivan, *Evidence for helical edge modes in*
2071 *inverted InAs/GaSb quantum wells*, Phys. Rev. Lett. **107**, 136603 (2011),
2072 doi:[10.1103/PhysRevLett.107.136603](https://doi.org/10.1103/PhysRevLett.107.136603).
- 2073 [86] L. Du, I. Knez, G. Sullivan and R.-R. Du, *Robust helical edge trans-*
2074 *port in gated InAs/GaSb bilayers*, Phys. Rev. Lett. **114**, 096802 (2015),
2075 doi:[10.1103/PhysRevLett.114.096802](https://doi.org/10.1103/PhysRevLett.114.096802).
- 2076 [87] S. Tang, C. Zhang, D. Wong, Z. Pedramrazi, H.-Z. Tsai, C. Jia, B. Moritz,
2077 M. Claassen, H. Ryu, S. Kahn, J. Jiang, H. Yan *et al.*, *Quantum spin hall state in*
2078 *monolayer 1t'-wte2*, Nat. Phys. **13**(7), 683 (2017), doi:[10.1038/nphys4174](https://doi.org/10.1038/nphys4174).
- 2079 [88] S. Wu, V. Fatemi, Q. D. Gibson, K. Watanabe, T. Taniguchi, R. J. Cava and
2080 P. Jarillo-Herrero, *Observation of the quantum spin hall effect up to 100 kelvin in*
2081 *a monolayer crystal*, Science **359**(6371), 76 (2018), doi:[10.1126/science.aan6003](https://doi.org/10.1126/science.aan6003),
2082 <https://www.science.org/doi/pdf/10.1126/science.aan6003>.
- 2083 [89] J. E. Hirsch, *Spin hall effect*, Phys. Rev. Lett. **83**, 1834 (1999),
2084 doi:[10.1103/PhysRevLett.83.1834](https://doi.org/10.1103/PhysRevLett.83.1834).
- 2085 [90] J. Balakrishnan, G. Kok Wai Koon, M. Jaiswal, A. H. Castro Neto and B. Özyilmaz,
2086 *Colossal enhancement of spin-orbit coupling in weakly hydrogenated graphene*, Nat.
2087 Phys. **9**(5), 284 (2013), doi:[10.1038/nphys2576](https://doi.org/10.1038/nphys2576).
- 2088 [91] J. Sinova, S. O. Valenzuela, J. Wunderlich, C. H. Back and T. Jungwirth, *Spin hall*
2089 *effects*, Rev. Mod. Phys. **87**, 1213 (2015), doi:[10.1103/RevModPhys.87.1213](https://doi.org/10.1103/RevModPhys.87.1213).
- 2090 [92] K. v. Klitzing, G. Dorda and M. Pepper, *New method for high-accuracy determi-*
2091 *nation of the fine-structure constant based on quantized hall resistance*, Phys. Rev.
2092 Lett. **45**, 494 (1980), doi:[10.1103/PhysRevLett.45.494](https://doi.org/10.1103/PhysRevLett.45.494).
- 2093 [93] R. B. Laughlin, *Quantized hall conductivity in two dimensions*, Phys. Rev. B **23**,
2094 5632 (1981), doi:[10.1103/PhysRevB.23.5632](https://doi.org/10.1103/PhysRevB.23.5632).
- 2095 [94] N. Nagaosa, J. Sinova, S. Onoda, A. H. MacDonald and N. P. Ong, *Anomalous hall*
2096 *effect*, Rev. Mod. Phys. **82**, 1539 (2010), doi:[10.1103/RevModPhys.82.1539](https://doi.org/10.1103/RevModPhys.82.1539).
- 2097 [95] M. Kohmoto, *Topological invariant and the quantization of the hall conductance*, An-
2098 nals of Physics **160**(2), 343 (1985), doi:[https://doi.org/10.1016/0003-4916\(85\)90148-](https://doi.org/10.1016/0003-4916(85)90148-4)
2099 [4](https://doi.org/10.1016/0003-4916(85)90148-4).
- 2100 [96] Q. Niu, D. J. Thouless and Y.-S. Wu, *Quantized hall conductance as a topological*
2101 *invariant*, Phys. Rev. B **31**, 3372 (1985), doi:[10.1103/PhysRevB.31.3372](https://doi.org/10.1103/PhysRevB.31.3372).
- 2102 [97] D. Xiao, M.-C. Chang and Q. Niu, *Berry phase effects on electronic properties*, Rev.
2103 Mod. Phys. **82**, 1959 (2010), doi:[10.1103/RevModPhys.82.1959](https://doi.org/10.1103/RevModPhys.82.1959).
- 2104 [98] M. Büttiker, *Absence of backscattering in the quantum hall effect in multiprobe*
2105 *conductors*, Phys. Rev. B **38**, 9375 (1988), doi:[10.1103/PhysRevB.38.9375](https://doi.org/10.1103/PhysRevB.38.9375).
- 2106 [99] T. Fukui, K. Shiozaki, T. Fujiwara and S. Fujimoto, *Bulk-edge correspondence for*
2107 *chern topological phases: A viewpoint from a generalized index theorem*, J. Phys.
2108 Soc. Jpn. **81**(11), 114602 (2012), doi:[10.1143/JPSJ.81.114602](https://doi.org/10.1143/JPSJ.81.114602), [https://doi.org/10.](https://doi.org/10.1143/JPSJ.81.114602)
2109 [1143/JPSJ.81.114602](https://doi.org/10.1143/JPSJ.81.114602).

- 2110 [100] X.-L. Qi, Y.-S. Wu and S.-C. Zhang, *Topological quantization of the spin hall effect*
2111 *in two-dimensional paramagnetic semiconductors*, Phys. Rev. B **74**, 085308 (2006),
2112 doi:[10.1103/PhysRevB.74.085308](https://doi.org/10.1103/PhysRevB.74.085308).
- 2113 [101] C.-X. Liu, S.-C. Zhang and X.-L. Qi, *The quantum anomalous hall ef-*
2114 *fect: Theory and experiment*, Annu. Rev. Condens. Matter Phys. **7**(1), 301
2115 (2016), doi:[10.1146/annurev-conmatphys-031115-011417](https://doi.org/10.1146/annurev-conmatphys-031115-011417), <https://doi.org/10.1146/annurev-conmatphys-031115-011417>.
2116
- 2117 [102] J. G. Checkelsky, R. Yoshimi, A. Tsukazaki, K. S. Takahashi, Y. Kozuka, J. Falson,
2118 M. Kawasaki and Y. Tokura, *Trajectory of the anomalous hall effect towards the*
2119 *quantized state in a ferromagnetic topological insulator*, Nat. Phys. **10**(10), 731
2120 (2014), doi:[10.1038/nphys3053](https://doi.org/10.1038/nphys3053).
- 2121 [103] X. Kou, S.-T. Guo, Y. Fan, L. Pan, M. Lang, Y. Jiang, Q. Shao, T. Nie, K. Murata,
2122 J. Tang, Y. Wang, L. He *et al.*, *Scale-invariant quantum anomalous hall effect in*
2123 *magnetic topological insulators beyond the two-dimensional limit*, Phys. Rev. Lett.
2124 **113**, 137201 (2014), doi:[10.1103/PhysRevLett.113.137201](https://doi.org/10.1103/PhysRevLett.113.137201).
- 2125 [104] M. Mogi, R. Yoshimi, A. Tsukazaki, K. Yasuda, Y. Kozuka, K. S. Takahashi,
2126 M. Kawasaki and Y. Tokura, *Magnetic modulation doping in topological insu-*
2127 *lators toward higher-temperature quantum anomalous Hall effect*, Appl. Phys.
2128 Lett. **107**(18), 182401 (2015), doi:[10.1063/1.4935075](https://doi.org/10.1063/1.4935075), https://pubs.aip.org/aip/apl/article-pdf/doi/10.1063/1.4935075/14470575/182401_1_online.pdf.
2129
- 2130 [105] C.-Z. Chang, W. Zhao, D. Y. Kim, H. Zhang, B. A. Assaf, D. Heiman, S.-C. Zhang,
2131 C. Liu, M. H. W. Chan and J. S. Moodera, *High-precision realization of robust*
2132 *quantum anomalous hall state in a hard ferromagnetic topological insulator*, Nat.
2133 Mater. **14**(5), 473 (2015), doi:[10.1038/nmat4204](https://doi.org/10.1038/nmat4204).
- 2134 [106] Y. Ou, C. Liu, G. Jiang, Y. Feng, D. Zhao, W. Wu, X.-X. Wang, W. Li, C. Song,
2135 L.-L. Wang, W. Wang, W. Wu *et al.*, *Enhancing the quantum anomalous hall effect*
2136 *by magnetic codoping in a topological insulator*, Adv. Mater. **30**(1), 1703062 (2018),
2137 doi:<https://doi.org/10.1002/adma.201703062>, <https://onlinelibrary.wiley.com/doi/pdf/10.1002/adma.201703062>.
2138
- 2139 [107] Y. Deng, Y. Yu, M. Z. Shi, Z. Guo, Z. Xu, J. Wang, X. H. Chen and Y. Zhang,
2140 *Quantum anomalous hall effect in intrinsic magnetic topological insulator MnBi₂Te₄*,
2141 Science **367**(6480), 895 (2020), doi:[10.1126/science.aax8156](https://doi.org/10.1126/science.aax8156), <https://www.science.org/doi/pdf/10.1126/science.aax8156>.
2142
- 2143 [108] C. Liu, Y. Wang, H. Li, Y. Wu, Y. Li, J. Li, K. He, Y. Xu, J. Zhang and Y. Wang,
2144 *Robust axion insulator and chern insulator phases in a two-dimensional antiferro-*
2145 *magnetic topological insulator*, Nat. Mater. **19**(5), 522 (2020), doi:[10.1038/s41563-019-0573-3](https://doi.org/10.1038/s41563-019-0573-3).
2146
- 2147 [109] C. Lei, S. Chen and A. H. MacDonald, *Magnetized topological insulator multilayers*,
2148 Proc. Natl. Acad. Sci. U.S.A. **117**(44), 27224 (2020), doi:[10.1073/pnas.2014004117](https://doi.org/10.1073/pnas.2014004117),
2149 <https://www.pnas.org/doi/pdf/10.1073/pnas.2014004117>.
- 2150 [110] R. S. K. Mong, A. M. Essin and J. E. Moore, *Antiferromagnetic topological insula-*
2151 *tors*, Phys. Rev. B **81**, 245209 (2010), doi:[10.1103/PhysRevB.81.245209](https://doi.org/10.1103/PhysRevB.81.245209).

- 2152 [111] A. M. Essin, J. E. Moore and D. Vanderbilt, *Magnetoelectric polarizability and*
2153 *axion electrodynamics in crystalline insulators*, Phys. Rev. Lett. **102**, 146805 (2009),
2154 doi:[10.1103/PhysRevLett.102.146805](https://doi.org/10.1103/PhysRevLett.102.146805).
- 2155 [112] J. Wang, B. Lian, X.-L. Qi and S.-C. Zhang, *Quantized topological magnetoelectric*
2156 *effect of the zero-plateau quantum anomalous hall state*, Phys. Rev. B **92**, 081107
2157 (2015), doi:[10.1103/PhysRevB.92.081107](https://doi.org/10.1103/PhysRevB.92.081107).
- 2158 [113] B. Fu, Z.-A. Hu and S.-Q. Shen, *Bulk-hinge correspondence and three-dimensional*
2159 *quantum anomalous hall effect in second-order topological insulators*, Phys. Rev.
2160 Res. **3**, 033177 (2021), doi:[10.1103/PhysRevResearch.3.033177](https://doi.org/10.1103/PhysRevResearch.3.033177).
- 2161 [114] R. Chen and S.-Q. Shen, *On the half-quantized hall conductance of massive surface*
2162 *electrons in magnetic topological insulator films* (2023), [2304.04229](https://arxiv.org/abs/2304.04229).
- 2163 [115] F. Wilczek, *Two applications of axion electrodynamics*, Phys. Rev. Lett. **58**, 1799
2164 (1987), doi:[10.1103/PhysRevLett.58.1799](https://doi.org/10.1103/PhysRevLett.58.1799).
- 2165 [116] D. M. Neno, C. A. C. Garcia, J. Gooth, C. Felser and P. Narang, *Axion physics in*
2166 *condensed-matter systems*, Nat. Rev. Phys. **2**(12), 682 (2020), doi:[10.1038/s42254-](https://doi.org/10.1038/s42254-020-0240-2)
2167 [020-0240-2](https://doi.org/10.1038/s42254-020-0240-2).
- 2168 [117] R.-L. Chu, J. Shi and S.-Q. Shen, *Surface edge state and half-quantized*
2169 *hall conductance in topological insulators*, Phys. Rev. B **84**, 085312 (2011),
2170 doi:[10.1103/PhysRevB.84.085312](https://doi.org/10.1103/PhysRevB.84.085312).
- 2171 [118] R. Li, J. Wang, X.-L. Qi and S.-C. Zhang, *Dynamical axion field in topological*
2172 *magnetic insulators*, Nat. Phys. **6**(4), 284 (2010), doi:[10.1038/nphys1534](https://doi.org/10.1038/nphys1534).
- 2173 [119] X.-L. Qi, R. Li, J. Zang and S.-C. Zhang, *Inducing a magnetic monopole with topo-*
2174 *logical surface states*, Science **323**(5918), 1184 (2009), doi:[10.1126/science.1167747](https://doi.org/10.1126/science.1167747),
2175 <https://www.science.org/doi/pdf/10.1126/science.1167747>.
- 2176 [120] W.-K. Tse and A. H. MacDonald, *Giant magneto-optical kerr effect and universal*
2177 *faraday effect in thin-film topological insulators*, Phys. Rev. Lett. **105**, 057401 (2010),
2178 doi:[10.1103/PhysRevLett.105.057401](https://doi.org/10.1103/PhysRevLett.105.057401).
- 2179 [121] K. Nomura and N. Nagaosa, *Surface-quantized anomalous hall current and the*
2180 *magnetoelectric effect in magnetically disordered topological insulators*, Phys. Rev.
2181 Lett. **106**, 166802 (2011), doi:[10.1103/PhysRevLett.106.166802](https://doi.org/10.1103/PhysRevLett.106.166802).
- 2182 [122] T. Morimoto, A. Furusaki and N. Nagaosa, *Topological magnetoelectric ef-*
2183 *fects in thin films of topological insulators*, Phys. Rev. B **92**, 085113 (2015),
2184 doi:[10.1103/PhysRevB.92.085113](https://doi.org/10.1103/PhysRevB.92.085113).
- 2185 [123] N. Varnava and D. Vanderbilt, *Surfaces of axion insulators*, Phys. Rev. B **98**, 245117
2186 (2018), doi:[10.1103/PhysRevB.98.245117](https://doi.org/10.1103/PhysRevB.98.245117).
- 2187 [124] M. M. Vazifeh and M. Franz, *Quantization and 2π periodicity of the*
2188 *axion action in topological insulators*, Phys. Rev. B **82**, 233103 (2010),
2189 doi:[10.1103/PhysRevB.82.233103](https://doi.org/10.1103/PhysRevB.82.233103).
- 2190 [125] A. Sekine and K. Nomura, *Axion electrodynamics in topological materials*, J. Appl.
2191 Phys. **129**(14), 141101 (2021), doi:[10.1063/5.0038804](https://doi.org/10.1063/5.0038804), [https://pubs.aip.org/aip/](https://pubs.aip.org/aip/jap/article-pdf/doi/10.1063/5.0038804/15259555/141101_1_online.pdf)
2192 [jap/article-pdf/doi/10.1063/5.0038804/15259555/141101_1_online.pdf](https://pubs.aip.org/aip/jap/article-pdf/doi/10.1063/5.0038804/15259555/141101_1_online.pdf).

- 2193 [126] C. Fang, M. J. Gilbert and B. A. Bernevig, *Topological insulators*
2194 *with commensurate antiferromagnetism*, Phys. Rev. B **88**, 085406 (2013),
2195 doi:[10.1103/PhysRevB.88.085406](https://doi.org/10.1103/PhysRevB.88.085406).
- 2196 [127] D. Xiao, J. Jiang, J.-H. Shin, W. Wang, F. Wang, Y.-F. Zhao, C. Liu, W. Wu,
2197 M. H. W. Chan, N. Samarth and C.-Z. Chang, *Realization of the axion insulator*
2198 *state in quantum anomalous hall sandwich heterostructures*, Phys. Rev. Lett. **120**,
2199 056801 (2018), doi:[10.1103/PhysRevLett.120.056801](https://doi.org/10.1103/PhysRevLett.120.056801).
- 2200 [128] D. S. Lee, T.-H. Kim, C.-H. Park, C.-Y. Chung, Y. S. Lim, W.-S. Seo and H.-H. Park,
2201 *Crystal structure, properties and nanostructuring of a new layered chalcogenide semi-*
2202 *conductor*, **Bi₂MnTe₄**, CrystEngComm **15**, 5532 (2013), doi:[10.1039/C3CE40643A](https://doi.org/10.1039/C3CE40643A).
- 2203 [129] Y. Gong, J. Guo, J. Li, K. Zhu, M. Liao, X. Liu, Q. Zhang, L. Gu, L. Tang,
2204 X. Feng, D. Zhang, W. Li *et al.*, *Experimental realization of an intrinsic magnetic*
2205 *topological insulator**, Chin. Phys. Lett. **36**(7), 076801 (2019), doi:[10.1088/0256-](https://doi.org/10.1088/0256-307X/36/7/076801)
2206 [307X/36/7/076801](https://doi.org/10.1088/0256-307X/36/7/076801).
- 2207 [130] P. Wang, J. Ge, J. Li, Y. Liu, Y. Xu and J. Wang, *Intrinsic*
2208 *magnetic topological insulators*, The Innovation **2**(2), 100098 (2021),
2209 doi:<https://doi.org/10.1016/j.xinn.2021.100098>.
- 2210 [131] M. M. Otrokov, T. V. Menshchikova, M. G. Vergniory, I. P. Rusinov, A. Y. Vya-
2211 zovskaya, Y. M. Koroteev, G. Bihlmayer, A. Ernst, P. M. Echenique, A. Arnau
2212 and E. V. Chulkov, *Highly-ordered wide bandgap materials for quantized anomalous*
2213 *hall and magnetoelectric effects*, 2D Mater. **4**(2), 025082 (2017), doi:[10.1088/2053-](https://doi.org/10.1088/2053-1583/aa6bec)
2214 [1583/aa6bec](https://doi.org/10.1088/2053-1583/aa6bec).
- 2215 [132] J. Li, Y. Li, S. Du, Z. Wang, B.-L. Gu, S.-C. Zhang, K. He, W. Duan and Y. Xu,
2216 *Intrinsic magnetic topological insulators in van der waals layered MnBi₂Te₄-family*
2217 *materials*, Sci. Adv. **5**(6), eaaw5685 (2019), doi:[10.1126/sciadv.aaw5685](https://doi.org/10.1126/sciadv.aaw5685), [https:](https://www.science.org/doi/pdf/10.1126/sciadv.aaw5685)
2218 [://www.science.org/doi/pdf/10.1126/sciadv.aaw5685](https://www.science.org/doi/pdf/10.1126/sciadv.aaw5685).
- 2219 [133] J. Ge, Y. Liu, J. Li, H. Li, T. Luo, Y. Wu, Y. Xu and J. Wang, *High-Chern-number*
2220 *and high-temperature quantum Hall effect without Landau levels*, Nat. Sci. Rev. **7**(8),
2221 1280 (2020), doi:[10.1093/nsr/nwaa089](https://doi.org/10.1093/nsr/nwaa089), [https://academic.oup.com/nsr/article-pdf/](https://academic.oup.com/nsr/article-pdf/7/8/1280/38881797/nwaa089.pdf)
2222 [7/8/1280/38881797/nwaa089.pdf](https://academic.oup.com/nsr/article-pdf/7/8/1280/38881797/nwaa089.pdf).
- 2223 [134] D. Zhang, M. Shi, T. Zhu, D. Xing, H. Zhang and J. Wang, *Topological axion states*
2224 *in the magnetic insulator mnbi₂te₄ with the quantized magnetoelectric effect*, Phys.
2225 Rev. Lett. **122**, 206401 (2019), doi:[10.1103/PhysRevLett.122.206401](https://doi.org/10.1103/PhysRevLett.122.206401).
- 2226 [135] J. B. Kogut, *The lattice gauge theory approach to quantum chromodynamics*, Rev.
2227 Mod. Phys. **55**, 775 (1983), doi:[10.1103/RevModPhys.55.775](https://doi.org/10.1103/RevModPhys.55.775).
- 2228 [136] T. Hatsuda and T. Kunihiro, *Qcd phenomenology based on a chiral effective*
2229 *lagrangian*, Phys. Rep. **247**(5), 221 (1994), doi:[https://doi.org/10.1016/0370-](https://doi.org/10.1016/0370-1573(94)90022-1)
2230 [1573\(94\)90022-1](https://doi.org/10.1016/0370-1573(94)90022-1).
- 2231 [137] P. Nason, *The lattice schwinger model with slac fermions*, Nucl. Phys. B **260**(2),
2232 269 (1985), doi:[https://doi.org/10.1016/0550-3213\(85\)90072-0](https://doi.org/10.1016/0550-3213(85)90072-0).
- 2233 [138] Z.-X. Li, A. Vaezi, C. B. Mendl and H. Yao, *Numerical observation of emer-*
2234 *gent spacetime supersymmetry at quantum criticality*, Sci. Adv. **4**(11), eaau1463
2235 (2018), doi:[10.1126/sciadv.aau1463](https://doi.org/10.1126/sciadv.aau1463), [https://www.science.org/doi/pdf/10.1126/](https://www.science.org/doi/pdf/10.1126/sciadv.aau1463)
2236 [sciadv.aau1463](https://www.science.org/doi/pdf/10.1126/sciadv.aau1463).

- 2237 [139] R. Stacey, *Eliminating lattice fermion doubling*, Phys. Rev. D **26**, 468 (1982),
2238 doi:[10.1103/PhysRevD.26.468](https://doi.org/10.1103/PhysRevD.26.468).
- 2239 [140] C. W. J. Beenakker, A. Donís Vela, G. Lemut, M. J. Pacholski and J. Tworzydło,
2240 *Tangent fermions: Dirac or majorana fermions on a lattice without fermion doubling*,
2241 Ann. Phys. **535**(7), 2300081 (2023), doi:<https://doi.org/10.1002/andp.202300081>,
2242 <https://onlinelibrary.wiley.com/doi/pdf/10.1002/andp.202300081>.
- 2243 [141] H.-W. Wang, B. Fu and S.-Q. Shen, *Signature of parity anomaly: Crossover from*
2244 *one half to integer quantized hall conductance in a finite magnetic field*, Phys. Rev.
2245 B **109**, 075113 (2024), doi:[10.1103/PhysRevB.109.075113](https://doi.org/10.1103/PhysRevB.109.075113).
- 2246 [142] A. M. M. Pruisken, *Universal singularities in the integral quantum hall effect*, Phys.
2247 Rev. Lett. **61**, 1297 (1988), doi:[10.1103/PhysRevLett.61.1297](https://doi.org/10.1103/PhysRevLett.61.1297).
- 2248 [143] Y.-F. Zhao, R. Zhang, R. Mei, L.-J. Zhou, H. Yi, Y.-Q. Zhang, J. Yu, R. Xiao,
2249 K. Wang, N. Samarth, M. H. W. Chan, C.-X. Liu *et al.*, *Tuning the chern*
2250 *number in quantum anomalous hall insulators*, Nature **588**(7838), 419 (2020),
2251 doi:[10.1038/s41586-020-3020-3](https://doi.org/10.1038/s41586-020-3020-3).
- 2252 [144] T. Fukui, Y. Hatsugai and H. Suzuki, *Chern numbers in discretized brillouin zone:*
2253 *Efficient method of computing (spin) hall conductances*, J. Phys. Soc. Jpn. **74**(6),
2254 1674 (2005), doi:[10.1143/JPSJ.74.1674](https://doi.org/10.1143/JPSJ.74.1674), <https://doi.org/10.1143/JPSJ.74.1674>.
- 2255 [145] D. Levine and P. J. Steinhardt, *Quasicrystals: A new class of ordered structures*,
2256 Phys. Rev. Lett. **53**, 2477 (1984), doi:[10.1103/PhysRevLett.53.2477](https://doi.org/10.1103/PhysRevLett.53.2477).
- 2257 [146] L. Fu and C. L. Kane, *Superconducting proximity effect and majorana fermions*
2258 *at the surface of a topological insulator*, Phys. Rev. Lett. **100**, 096407 (2008),
2259 doi:[10.1103/PhysRevLett.100.096407](https://doi.org/10.1103/PhysRevLett.100.096407).
- 2260 [147] X.-L. Qi, T. L. Hughes and S.-C. Zhang, *Chiral topological supercon-*
2261 *ductor from the quantum hall state*, Phys. Rev. B **82**, 184516 (2010),
2262 doi:[10.1103/PhysRevB.82.184516](https://doi.org/10.1103/PhysRevB.82.184516).
- 2263 [148] J. Wang, Q. Zhou, B. Lian and S.-C. Zhang, *Chiral topological superconductor and*
2264 *half-integer conductance plateau from quantum anomalous hall plateau transition*,
2265 Phys. Rev. B **92**, 064520 (2015), doi:[10.1103/PhysRevB.92.064520](https://doi.org/10.1103/PhysRevB.92.064520).
- 2266 [149] B. Fu and S.-Q. Shen, *Anomalous coherence length of majorana zero modes at*
2267 *vortices in superconducting topological insulators*, Phys. Rev. B **107**, 184517 (2023),
2268 doi:[10.1103/PhysRevB.107.184517](https://doi.org/10.1103/PhysRevB.107.184517).
- 2269 [150] J. Li, R.-L. Chu, J. K. Jain and S.-Q. Shen, *Topological anderson insulator*, Phys.
2270 Rev. Lett. **102**, 136806 (2009), doi:[10.1103/PhysRevLett.102.136806](https://doi.org/10.1103/PhysRevLett.102.136806).
- 2271 [151] C. W. Groth, M. Wimmer, A. R. Akhmerov, J. Tworzydło and C. W. J. Beenakker,
2272 *Theory of the topological anderson insulator*, Phys. Rev. Lett. **103**, 196805 (2009),
2273 doi:[10.1103/PhysRevLett.103.196805](https://doi.org/10.1103/PhysRevLett.103.196805).
- 2274 [152] H.-M. Guo, G. Rosenberg, G. Refael and M. Franz, *Topological anderson*
2275 *insulator in three dimensions*, Phys. Rev. Lett. **105**, 216601 (2010),
2276 doi:[10.1103/PhysRevLett.105.216601](https://doi.org/10.1103/PhysRevLett.105.216601).